ARIANA MARIA DA CONCEIÇÃO LACORTE CANIATO SERRANO

# SYNTHESIS AND DESIGN OF TUNABLE MICROWAVE BANDPASS FILTERS USING PLANAR PATCH RESONATORS

São Paulo & Grenoble

2011

ARIANA MARIA DA CONCEIÇÃO LACORTE CANIATO SERRANO

# SYNTHESIS AND DESIGN OF TUNABLE MICROWAVE BANDPASS FILTERS USING PLANAR PATCH RESONATORS

A thesis in cotutelle submitted to
Escola Politécnica da Universidade de São Paulo
and to Université de Grenoble
in partial fulfillment of
Doctor's Degree of Electrical Engineering
Sub-area: Microelectronics

Advisors: Prof. Dr. Fatima Salete Correra
Prof. Dr. Philippe Ferrari
Prof. Dr. Tân-Phu Vuong

São Paulo & Grenoble

2011

*De onde ela vem?! De que matéria bruta*
*Vem essa luz que sobre as nebulosas*
*Cai de incógnitas criptas misteriosas*
*Como as estalactites duma gruta?!*

*Vem da psicogenética e alta luta*
*Do feixe de moléculas nervosas,*
*Que, em desintegrações maravilhosas,*
*Delibera, e depois, quer e executa!*

*Vem do encéfalo absconso que a constringe,*
*Chega em seguida às cordas do laringe,*
*Tísica, tênue, mínima, raquítica...*

*Quebra a força centrípeta que a amarra,*
*Mas, de repente, e quase morta, esbarra*
*No mulambo da língua paralítica*

***Augusto dos Anjos (A idéia)***

# ACKNOWLEDGEMENTS

Antes de tudo, agradeço a Gustavo Rehder por ter sido mais que um marido perfeito, um grande amigo e colega, me ouvindo e me ajudando, e por todas as discussões sobre o tema durante meu trabalho.

I deeply thank my advisors, Prof. Fatima Salete Correra, Prof. Philippe Ferrari, and Prof. Tân-Phu Vuong, whose help, advice and supervision were invaluable, transcending the barrier of languages with a healthy mix of Portuguese, French and English.

Especialmente agradeço à Fatima por toda a dedicação e paciência com todos os processos administrativos pela qual eu a fiz passar, e pela brilhante orientação desta tese, assim como o foi para com todos os outros trabalhos nos últimos (mais de) dez anos.

Et je tiens à remercier tout particulièrement Philippe pour le plaisir que j'ai eu à côtoyer un si précieux collègue, pour son accueil chaleureux au laboratoire, pour l’excellente expérience professionnelle et pour toutes les opportunités qu’il m’a apportées.

Que Prof. Tân-Phu Vuong reçoive toute l'expression de ma reconnaissance pour m'avoir proposé la cotutelle et pour son dynamisme qui m'ont permis de mener à bien mes études en France.

I sincerely thank my thesis committee: Prof. Eduardo Pouzada, Prof. Octávio de Andrade and Prof. Bernard Jarry, in special the last two who agreed to be *rapporteurs* of this thesis.

I would like to also thank all my dear colleagues that directly or indirectly helped to improve my work, especially Sandro Verri, Emmanuel Pistono and Nicolas Corrao.

Finally, I would like to thank Capes for the financial support in Brazil, and to Erasmus Mundus Consortium for the financial support during the period of hard, but amusing studies in France and for the opportunity to live in the second city of my heart (after São Paulo), Grenoble.

# RESUMO

O objetivo desta tese é o projeto e a síntese de filtros passa-faixa sintonizáveis em frequências de micro-ondas utilizando ressoadores planares tipo *patch*. As características dos filtros projetados, tais como frequência central, largura de banda e/ou seletividade, são eletronicamente ajustadas por uma tensão de controle DC. Uma metodologia para a concepção e síntese de filtros sintonizáveis *patch* é desenvolvida e aplicada a dois filtros com topologias triangular e circular. A metodologia fornece técnicas para extrair o esquema de acoplamento que modela o comportamento do filtro e as equações necessárias para calcular a matriz de acoplamento. Então, a resposta teórica do filtro resultante da análise dos coeficientes da matriz de acoplamento é comparada com os resultados das simulações completas. As simulações completas combinam os resultados da simulação eletromagnética 3D do layout do filtro com os resultados da simulação elétrica dos dispositivos de ajuste, representados por seu modelo elétrico equivalente de elementos discretos. Isso permite o correto modelamento das características do ajuste e a definição de seus limites. A fim de validar a metodologia, os filtros *patch* sintonizáveis são fabricados usando tecnologia de micro-ondas de circuito Integrado (MIC) sobre substratos flexíveis. As dimensões mínimas são maiores do que 0,5 mm, garantindo um processo de fabricação de baixo custo. O primeiro filtro é um filtro *patch dual-mode* sintonizável que utiliza um ressonador triangular com duas fendas perpendiculares. A frequência central e a largura de banda do filtro podem ser ajustadas individualmente por um controle independente de cada modo fundamental degenerado. O controle dos modos é feito através de diodos varactor montados nas fendas do ressoador *patch*. O filtro apresenta variação de 20 % de frequência central de 2,9 GHz a 3,5 GHz. A banda relativa de 3 dB varia de 4 % a 12 %. Duas tensões de polarização DC diferentes variando de 2,5 V a 22 V são usadas para ajustar este filtro. O segundo filtro é um filtro *patch triple-mode* sintonizável que utiliza um ressoador circular com quatro fendas radiais, nas quais são conectados os diodos varactor. A frequência central e a largura de banda deste filtro variam simultaneamente. O filtro apresenta 27 % de variação da frequência central de 1,8 GHz a 2,35 GHz com variação concomitante da largura de banda relativa de 8,5 % para 26 %. Apenas uma única tensão de polarização DC variando de 0,5 V a 20 V é usada para sintonizar este filtro. Ambos os filtros são capazes de lidar com níveis de potência de no mínimo +14,5 dBm (filtro com ressoador triangular) e +12,9 dBm (filtro com ressoador circular).

Palavras-chave: Filtros reconfiguráveis. Ressoadores *patch*. Diodo varactor. Ressoador multimodo.

# RESUME

L’objectif de la thèse était la conception et la synthèse de filtres RF passe-bande reconfigurables, basés sur des résonateurs de type “Patch”. Les caractéristiques des filtres reconfigurables conçus, à savoir leur fréquence de fonctionnement, leur bande passante et leur sélectivité, peuvent être ajustées dynamiquement à l’aide d’une tension de commande DC. Une méthode de conception dédiée à la synthèse des filtres reconfigurables a été développée et appliquée à deux filtres reconfigurables basés sur des « patchs » triangulaire et circulaire. La technique de synthèse repose sur l’analyse de la matrice de couplage, facilitée par une analyse électromagnétique des modes propres des résonateurs « Patch ». Les filtres reconfigurables ont été conçus et optimisés à l’aide de simulations électromagnétiques 3D en incluant le modèle électrique des composants localisés utilisés, diodes varactors et capacités fixes. Les deux filtres reconfigurables ont été réalisés en technologie circuit imprimé. Les dimensions minimum du « layout » ont été choisies afin d’être compatibles avec une technologie bas coût, la dimension la plus faible n’étant pas inférieure à 0,5 mm. Le premier filtre est un filtre double mode utilisant un résonateur de type triangulaire avec deux fentes perpendiculaires. La fréquence centrale du filtre ainsi que sa bande passante peuvent être ajustées de manière indépendante en contrôlant de manière séparée les deux modes dégénérés du « Patch » triangulaire. Ceci est obtenu à l’aide de varactors placés sur les deux fentes perpendiculaires du « Patch ». Chaque varactor permet de contrôler indépendamment l’un des deux modes dégénérés. L’analyse de la matrice de couplage a permis de déduire les conditions optimales de commande des varactors. Le filtre réalisé présente un accord de la fréquence centrale de 20 %, entre 2,9 GHz et 3,5 GHz. La bande passante relative peut être ajustée de 4 % à 12 %. Les tensions de commande des varactors varient de 2,5 V à 22 V. Le second filtre est un filtre triple mode utilisant un résonateur de type circulaire avec quatre fentes radiales, chacune munie d’un varactor. La fréquence centrale et la bande passante du filtre varient de manière simultanée lorsque les varactors sont commandés avec la même tension. Le filtre réalisé présente un accord de la fréquence centrale de 27 %, entre 1,8 GHz et 2,35 GHz. La bande passante relative peut être ajustée de 8,5 % à 26 %. La tension de commande des varactors varie de 0,5 V à 22 V. Une analyse non linéaire a été menée pour les deux filtres réalisés. Les deux filtres présentent un point de compression de respectivement +14.5 dBm pour le « Patch » triangulaire et +12.9 dBm pour le « Patch » circulaire. Les points d’interception d’ordre 3 ont également été mesurés.

Mots clés: Filtres reconfigurables. Résonateurs “Patch”. Diodes varactors. Résonateurs multi-modes.

# ABSTRACT

The objective of this thesis is the design and synthesis of tunable bandpass filters at microwave frequencies using planar patch resonators. The characteristics of the designed filters, such as center frequency, bandwidth, and/or selectivity, are electronically adjusted by a DC voltage control. A methodology for the design and synthesis of tunable patch filters is developed and applied to two filters with triangular and circular topologies. The methodology provides techniques to extract the coupling scheme that models the filter behavior and the necessary equations for calculating the corresponding coupling matrix. Then, the theoretical filter response resulting from the analysis of the coupling matrix coefficients is compared to the results of complete simulations. The complete simulations combine the results of the 3D electromagnetic (EM) simulation of the filter layout with the results of the electrical simulation of the tuning devices, represented by their lumped elements equivalent model. This allows the correct model of the tuning effect and the definition of the tuning possibilities and limits. In order to validate the methodology, the tunable patch filters are fabricated using Microwave Integrated Circuit (MIC) technology on flexible substrates. The minimum dimensions are greater than 0.5 mm, ensuring a low cost fabrication process. The first filter is a tunable dual-mode patch filter using a triangular resonator with two perpendicular slots. The central frequency and the bandwidth of the filter are individually tuned by independently controlling each degenerate fundamental mode. The topology with uncoupled modes allows the control of each resonant mode frequency by varactor diodes mounted across the slots of the patch resonator. This filter presents a center frequency tuning range of 20 %, varying from 2.9 GHz to 3.5 GHz. The $FBW_{3dB}$ can be varied from 4 % to 12 %. Two different DC bias voltages ranging from 2.5 V to 22 V are used to tune this filter. The second filter is a tunable triple-mode patch filter using a circular resonator with four slots, across which the varactor diodes are connected. The center frequency and bandwidth of this filter vary simultaneously. This filter presents a center frequency tuning range of 27 %, varying from 1.8 GHz to 2.35 GHz, changing concomitantly with the bandwidth from 8.5 % to 26 %. Only a single DC bias voltage ranging from 0.5 V to 20 V is used to tune the filter. Both filters are able to handle power levels as high as +14.5 dBm (triangular patch filter) and +12.9 dBm (circular patch filter).

Keywords: Tunable filters. Patch resonators. Varactor diode. Multimode resonator.

# TABLE OF CONTENTS

# 1 INTRODUCTION

Today's modern telecommunication systems have become multi-standard, having multiband coverage and multifunctionality. Hence, they require a wide variety of analog circuits containing several amplifiers, filters, oscillators, antennas etc., for each specific application frequency. This trend demands the development of tunable and reconfigurable filters that constitute a key component in the radio frequency (RF) chain. Electronically tunable and reconfigurable filters have an control circuit to adjust their characteristics such as center frequency, bandwidth, and/or selectivity in a predetermined and controlled manner, replacing the need for multiple channels, improving overall system reliability, reducing size, weight, complexity, and cost.

The applications of these filters can be classified according to their behavior. For example, a filter capable of selecting different frequency bands may replace a conventional filter bench, reducing size and cost. Radar systems may employ a tunable bandwidth filter to eliminate out-of-band jamming spectral components. Communication systems with multiband transceivers may also adapt a filter capable of synchronizing different information channels.

Several types of tunable filters have been presented in the literature using different technologies, topologies, and tuning mechanisms. Despite the great development of planar filters using microstrip resonators tuned by varactor diodes, PIN diodes, or microelectromechanical systems (MEMS), planar patch resonators have been rarely investigated until this thesis.

The design methodology of any kind of filter involves a theoretical analysis, based on techniques that provide the necessary couplings to achieve a desired filter response. These techniques are widely utilized in all filter technologies, however, until now, there are very scarce publications about synthesis techniques applied to patch filters. Moreover, tunable filters derived directly from these techniques have not been demonstrated yet and there has been a major effort worldwide devoted to it.

## 1.1 OBJECTIVES

The objective of this thesis was the design and synthesis of tunable bandpass filters at microwave frequencies using planar patch resonators.

The main goal was to obtain filters that can have their characteristics such as center frequency, bandwidth, and selectivity electronically adjusted by a DC voltage control. For that, it was investigated the integration of commercially available components such as varactor diodes or RF MEMS for applications in microwave frequencies with patch filters.

A synthesis technique using coupling matrix applied to patch filters was developed to establish the theoretical approach and to aid in the design and optimization process, identifying which couplings should be changed in order to obtain the desired filter specifications.

The tunable patch filters were to be designed and optimized through complete simulations including 3D electromagnetic (EM) responses of the filters' layout and the electrical influence of the discrete components on these responses. Then, in order to validate the synthesis and the design, tunable patch filters were intended to be fabricated using Microwave Integrated Circuit (MIC) technology on flexible substrates and the tunable elements were to be mounted on the filter with regular soldering. The minimum dimensions on the layouts were to be chosen to be compatible with traditional photolithographic techniques in printed circuit boards (PCB) or automated mechanical PCB prototyping processes, facilitating manufacture and reducing costs.

A final analysis was envisaged to compare the measured and simulated results, evaluating the tuning ranges in terms of center frequency, bandwidth, and selectivity. In addition, linearity was to be assessed through power and intermodulation measurements.

The present work was developed at the Microwave and Optoelectronics Group (GMO) of Laboratory of Microelectronics (LME) of Polytechnic School of the University of São Paulo (EPUSP), Brazil, in conjunction with the *Institut de Microélectronique, Electromagnétisme et Photonique et LAboratoire d'Hyperfréquences et de Caractérisation* (IMEP-LAHC), in Grenoble, France.

## 1.2 THESIS OVERVIEW

A bibliographical study of tunable filters is shown in chapter 2 describing the evolution of microwave tunable filters in different technologies and with different tuning mechanisms, showing the most performing microwave planar tunable filters presented in the international literature. Microstrip and patch tunable filters are compared in terms of area, operating frequency, tuning elements, DC bias voltage of the tuning element, and electrical performance. A figure of merit is proposed in order to compare tunable planar filters with different characteristics in fair manner. This chapter also presents a basic theory of patch filters, providing concepts and formulation of three patch resonators with different geometries: square, circular and triangular.

Chapter 3 concerns the methodology proposed for the design and synthesis of tunable patch filters. Initially, the basic concepts of coupling matrices are described, followed by the necessary formulation to calculate a coupling matrix relative to the designed patch filter. Then, the methodology is detailed. 3D EM simulations are used to design the initial filter and to determine the nature of the couplings presented in the structure. The methodology is based on the theoretical analysis of the coupling matrix and on complete simulations that can correctly predetermine the tunable patch filter response. Complete simulations embed 3D EM simulations of the filter layout into electrical simulations that account for the equivalent circuit model of the tuning element. The fabrication and assembly processes are discussed, followed by a description of the characterization methods of the tunable patch filters at small signal and higher power levels.

In chapter 4, the methodology is applied to the design of a tunable dual-mode filter using a triangular patch resonator. The type of tuning that can be achieved by the filter is discussed, as well as the electrical modeling of the tuning elements. The filter is analyzed, fabricated, and characterized. Then, the theoretical, simulated and measured frequency responses of the filter are compared. Finally, a discussion on the filter performance is presented indicating the limits of the tuning range, the filter losses, miniaturization achieved, the calculated unloaded quality factor. A comparison is given between the tunable triangular patch filter and the tunable filters presented in the literature through the proposed figure of merit defined in chapter 2.

In chapter 5, the methodology is applied to the design of a tunable triple-mode filter using a circular patch resonator. A different behavior from the previous design is shown, making the theoretical analysis more complex. The filter is fabricated and characterized and then, the theoretical, simulated and measured frequency responses of the filter are compared. The DC biasing is discussed in order to allow different types of tuning with a higher degree of freedom. Finally, a discussion of the filter performance is presented indicating the limits of the tuning range, the filter losses, miniaturization achieved, the calculated unloaded quality factor. The tunable filter with circular patch resonator is compared to the tunable triangular filter presented in chapter 4 and to the tunable filters presented in the literature through the proposed figure of merit.

Lastly, chapter 6 presents the conclusions of the developed work and the perspectives of envisaged future works as a natural continuation of the results presented in this thesis.

# 2 BACKGROUND AND STATE-OF-THE-ART

## 2.1 TUNABLE FILTERS

Since the appearance of the first tunable filters at microwave frequencies during the 1950s, the study of tunable filters has been strongly attached to the fixed filters technology. Based on waveguide cavity, mainly three different approaches of frequency tuning were developed, which are still used today:

- Mechanical tuning - alters the cavity dimensions;
- Magnetic tuning - alters the magnetic field applied to a ferromagnetic material;
- Electronic tuning - alters the electric field applied to a component or to an electric/ferroelectric material.

Throughout the next two decades, a fast spread of the tuning concept was experienced and several designs were developed with either mechanical tuning by using movable metallic or dielectric walls[1], or tuning screws[2], or magnetic tuning, using pieces of ferrites[3, 4] inside the cavities. The Yttrium-Iron-Garnet (YIG) ferrite became widely utilized for its excellent performance, especially for very narrow bandpass filters. These approaches result in filters with great performance, very low insertion loss, and high power handling, but they are bulky and their response time is long. Moreover, these cavity tunable filters are expensive because they require custom machining, delicate assembly, adjustments, and calibration, making it difficult for mass-production and integration with other devices. In order to increase the response speed of reconfigurable filters, electronic tuning designs were investigated by using fast response components, such as varactor diodes[5], and plasma discharge[6]. Despite the fast response, the low quality factor (Q) of the varactor diodes reduces the overall filter's Q and the plasma discharge mechanism can lead to a complex solution.

At the same time, different solutions to reduce cost, size, and weight and to improve manufacturability were investigated. Planar technology has become an important alternative for being able to meet those characteristics and because the planar circuits were easy to test and to integrate to other circuits and systems. Therefore, in the following decades, several tunable filters topologies in planar technology using transmission lines[7], rings[8], striplines[9], comblines[10], and others[11, 12] began to be exploited.

Continuously efforts were dedicated to reduce size and weight of the tuning filters and hence, dual-mode filters became more interesting. The dual-mode concept has been a significant improvement first introduced by Lin[13], in 1951. This concept allowed the increase of the filter's order without increasing the number of resonators. It is based on the coupling of the so-called degenerate modes, which are modes that have the same resonant frequency but different EM field distribution, in the same resonator. Almost two decades later, when the planar technology became popular, Wolff[14] applied this concept to planar filters, using a circular ring resonator. Nonetheless, only after 1975 the concept was widely implemented in microwave filters. At first, dual-mode filters were based on waveguide[15, 16] and on dielectric resonator[17] technologies, either using iris or screws strategically placed in the resonant cavities in order to couple the modes, resulting in dual-, triple-, quad-, and more generally, multi-mode filters. In planar technology, dual-mode filters were implemented only decades later, using a very simpler coupling method, by changing small parts of the layout geometry in microstrip[18] and patch[19] resonators.

In the late 1990s, in addition to the already popular varactor diodes, other components, such as field effect transistor (FET) switches, PIN diodes, and RF MEMS[20] switches began to be more commonly used for discrete tuning of microwave filters. For continuous tuning, the novelty was the use of RF MEMS capacitors[21]. The response time of the RF MEMS is longer compared to the semiconductor-based components, but they can operate at higher frequencies with lower insertion loss and higher power handling.

Planar microstrip filters are present nowadays in most commercial systems that operate in the lower range of the microwave frequencies spectrum, approximately from 1 GHz to 10 GHz. The quest for the best performance of tuning filters is directed to achieve low insertion loss, wide tuning range, reduced area, and low DC voltage control. The fabrication process is taken into account considering the traditional photolithographic process on commercial substrate, which constitutes the simpler and less-expensive process.

In order to facilitate a fair comparison between tunable filters, since they have different characteristics and the designer takes into account different boundaries, a figure of merit (FoM) was defined. It is not a complete criterion for all the filter characteristics, but is generic, considering the basic important characteristics in order to compare any type of tunable filter. The FoM defined here considers a filter surface factor, tunability, and losses.

The surface factor ($SF$)[22] indicates the compromise between the maximum operating frequency and the size of the filter, given by eq. (1). This factor should be as high as possible to achieve a compact device. In the equation, $c$ is the speed of light, $f_{min}$ is the minimum operating frequency of the tunable filter, and $A$ is the area of the manufactured filter.

$$SF = \frac{c^2}{f_{min}^2 \cdot A} \tag{1}$$

The tuning range of the filter is defined by the capability of the filter to tune a desired characteristic ($R$), which may be center frequency or bandwidth. This value should be as high as possible, and can be calculated by eq. (2), where $R_{max}$ is the maximum value of the characteristic and $R_{min}$ is the minimum value of the characteristic.

$$\text{Tuning range } = \frac{R_{max} - R_{min}}{(R_{max} + R_{min})/2} \tag{2}$$

Because the tuning range depends on the limits of the losses within the passband fixed by the designer, the comparison of a tuning range without comparing the filter loss is not reasonable. Therefore, the FoM also considers the loss as the worst value within the tuning range, where the worst return loss (RL) is the minimum absolute value of $|S_{11}|$, and the worst insertion loss (IL), is the maximum absolute value of $|S_{12}|$. Finally, the FoM is defined by eq. (3), where a higher value means a better filter performance.

$$\text{FoM} = \frac{SF \cdot Tuning\ Range \cdot RL}{IL} \tag{3}$$

In view of the many different applications existing nowadays, a narrower or wider bandwidth does not necessarily means a best characteristic. Therefore, the bandwidth of the filter is not considered in this FoM. Nevertheless, the bandwidth is discussed along the work and is defined as the absolute 3-dB bandwidth ($ABW_{3dB}$ or just bandwidth) and 3-dB fractional bandwidth ($FBW_{3dB}$) defined in eq. (4), where ($f_{3dB\ up}$ - $f_{3dB\ low}$) is the difference between the upper and lower frequencies at the passband when the insertion loss drops 3 dB relative to the center frequency $f_c$.

$$\text{FBW}_{3dB} = \frac{\text{ABW}_{3dB}}{f_c} = \frac{f_{3dB\ up} - f_{3dB\ low}}{f_c} \tag{4}$$

Some interesting discrete tunable microstrip filters have been recently presented using commercial PIN and varactor diodes, or using custom switches and varactors:

Chen *et al*[23] showed that it is possible to change a loaded ring filter's characteristic from bandpass to bandstop by changing the commercial varactor diodes DC bias voltage from 0 V to 5.5 V at 2.45 GHz. The filter was fabricated using traditional photolithographic process on a commercial microwave substrate.

A custom-switch bandstop open loop filter[24] working at approximately 10 GHz was demonstrated using eight vanadium dioxide switches, which change from a semiconductor state to a metallic state when a DC bias voltage is applied to them. The filter was fabricated using two levels of photolithographic mask on a sapphire substrate and wire bonding was used to connect the switches. Each switch adds a pole to the bandstop filter changing among the preselected configurations of bandwidth and central frequency ($f_c$).

Wideband bandpass filters with reconfigurable bandwidths using stubs connected to PIN diodes were presented, with two preselected bandwidths when the PIN diodes are ON or OFF[25]. In the ON-mode, the 35 % $FBW_{3dB}$ of the OFF-mode is reduced to 16 %, whereas the IL increased 4 dB at a center frequency of 1.9 GHz.

Ultra wideband bandpass filters with reconfigurable bandwidths were presented with three preselected bandwidths using a set of PIN diodes[26]. The IL was constant around 1.3 dB and the $FBW_{3dB}$ changed from 70 % to 85 % centered at approximately 2.4 GHz. The bandpass filters with reconfigurable bandwidths were fabricated using traditional photolithographic process on commercial microwave substrate.

In continuously tuned filters, commercial silicon (Si) and gallium arsenide (GaAs) varactors, and Barium-Strontium-Titanate (BST) capacitors are largely used:

A tunable combline filter with high selectivity and constant-bandwidth in low frequencies (800 MHz) was presented[27]. Commercial varactor diodes were biased by a DC voltage ranging from 0 V to 20 V for a tuning range of 12 % with high $IL_{max}$ of 5 dB. The filter was fabricated using traditional photolithographic process on commercial microwave substrate, achieving a good scale factor *SF* of 4.3.

On the other hand, a very high frequency tuning range of 41 % was demonstrated with a meander loop filter at $f_{min}$ of 1.68 GHz, but still, the insertion loss was very high, reaching 7.6 dB[28]. The filter was also fabricated using traditional photolithographic process on a commercial microwave substrate, achieving a scale factor *SF* of 3.2.

Another tunable folded-microstrip filter fabricated using traditional photolithographic process on commercial microwave substrate was presented with an outstanding *SF* of 18.6[29]. Its minimum center frequency is 1.39 GHz. It was tuned with commercial GaAs varactors biased by DC voltage ranging from 0 V to 20 V. The filter has a moderate $f_c$ tuning range of 26 %, a reasonable $IL_{max}$ of 2.5 dB, and bandwidth tuning range of 30 %. However, both its $f_c$ and bandwidth vary simultaneously, without any possibility of independent control.

A combline filter centered at higher frequencies ($f_{min}$ of 11.7 GHz) and fabricated on alumina with laser drilling was presented with a medium *SF* of 2.9[30]. The filter exhibits a moderate $f_c$ tuning range of 20 %. However, the IL is high, reaching 10 dB, and its $f_c$ and bandwidth also vary simultaneously. Moreover, this combline filter is tuned with BST varactors, which need a high DC bias voltage of 100 V.

A tunable bandpass filter with $f_{min}$ at 1.02 GHz with selectivity control was presented[31]. It uses commercial Si varactor diodes to change the $f_c$ and the transmission zero location from the upper-side band to the lower-side band, keeping the bandwidth fixed. Despite the medium *SF* of 3.0, it showed an $IL_{max}$ of 3 dB and a very poor tuning range of 5.5 %.

Finally, a tunable coplanar waveguide (CPW) ring filter with bandwidth control was presented[32]. The filter showed a moderate tuning range of 14 % with moderate $IL_{max}$ of 2.5 dB at the working frequency $f_c$ of 1.8 GHz, and a poor *SF* of 1.1. Although using BST varactors, the applied DC bias voltage was reasonable, varying from a 0 V to 35 V.

A summary of the different tunable filters presented in the international literature and described above is shown in Table 2.1. As a conclusion of this short description of tunable filters, from an electrical point of view, one can divide these devices into 4 groups (A), (B), (C) and (D), used in Table 2.1.

(A) $f_c$ tuning and constant bandwidth;

(B) Constant $f_c$ and bandwidth tuning;

(C) Simultaneously $f_c$ and bandwidth tuning, without independent control;

(D) Selectivity tuning.

Table 2.1 – Summary of tunable microstrip filters from the international literature

| Ref | Topology | Tuning type | Tuning Element | DC bias | $f_{min}$ (GHz) | $IL_{max}$ (dB) | Tuning range | Area ($mm^2$) | FoM |
|---|---|---|---|---|---|---|---|---|---|
| [23] | square Ring | D - discrete | varactor diode | 5.5 V | 2.45 | 1.6 | - | 900 | - |
| [24] | open Loop | C - discrete | $VO_2$ switch | - | 9.0 | - | 5.4 % | 84 | - |
| [25] | stub | B - discrete | PIN diode | - | 1.9 | 4.1 | 50 % | 1200 | 2.2 |
| [26] | ring & stub | C - discrete | PIN diode | - | 2.4 | 1.35 | 20 % | 900 | 1.01 |
| [27] | combline | A - continuous | varactor diode | 20 V | 0.75 | 5.0 | 18 % | 1250 | 1.86 |
| [28] | meander loop | C - continuous | varactor diode | 20 V | 1.68 | 7.6 | 41 % | 400 | 1.20 |
| [29] | folded | C - continuous | GaAs varactor diode | 20 V | 1.39 | 2.5 | 26 % | 200 | 15.6 |
| [30] | combline | C - continuous | BST varactor | 100 V | 11.7 | 10.0 | 20 % | 8.8 | 0.54 |
| [31] | folded | D - continuous | varactor diode | 20 V | 1.06 | 3.5 | 5.5 % | 1260 | 0.54 |
| [32] | CPW ring | B - continuous | BST varactor | 35 V | 1.8 | 2.5 | 10 % | 1015 | 0.56 |

Right after the advent of microstrip filters, patch filters began to be investigated. Patch filters are fabricated in the same planar technology as the microstrip filters, but employ, instead of strips, resonators with two-dimensional geometries, such as circle, square, or triangle, as shown in Figure 1. Although they occupy larger area, they show lower IL than microstrip filters. In order to reduce the area, dual-mode patch filters were proposed, and the first ones were presented in the literature in 1991, using circular and square geometries[19], followed by the triangular geometry[33], in 2003.

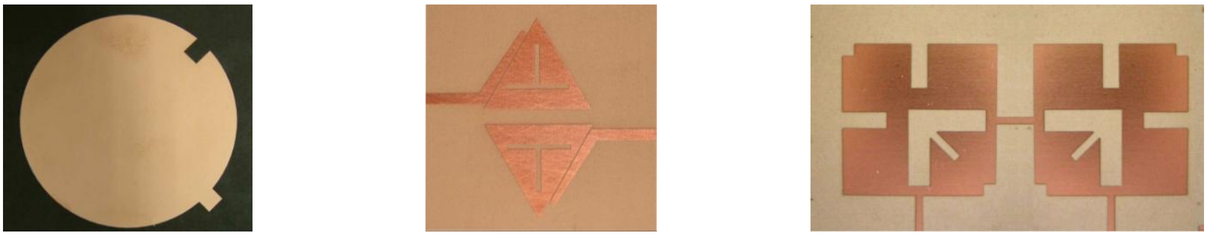

(a) (b) (c)

Figure 1 – Examples of patch resonators (a) circular, (b) triangular, and (c) square.

Dual-mode patch filters were also the subject of my master's dissertation, entitled "Design of microwave planar bandpass filters using dual-mode patch resonators"[34], which provided the basis for this work. Although several variations of dual-mode patch filters have been presented in the last two decades, there are very few works reported in the literature showing tunable patch filters. The only two tunable patch filters that have been reported until this work were fabricated using traditional photolithography process on commercial microwave substrates. They both used PIN diodes for a discrete tuning. The first one showed a reconfigurable triangular patch filter with constant $f_c$ and a $FBW_{3dB}$ variation of 60 % from 4.5 % to 8.6 % at 10 GHz, and IL increasing from 2.2 dB to 3.3 dB[35]. The filter presented a poor *SF* of 0.9. The second reconfigurable patch filter used a slotted-square resonator to realize a selectivity reconfigurable filter, keeping the $FBW_{3dB}$ constant[36]. The filter presented the same SF than the previous one and its working frequency changed from 9 GHz to 10 GHz, keeping a narrow bandwidth of 3.8 % with a high IL of about 3.5 dB. These publications, summarized in Table 2.2, do not present any methodology for designing tunable patch filters.

Table 2.2 - Summary of tunable patch filters from the international literature

| Ref | Topology | Tuning type | Tuning Element | DC bias | $f_{min}$ (GHz) | $IL_{max}$ (dB) | Tuning range | Area (mm$^2$) | FoM |
|---|---|---|---|---|---|---|---|---|---|
| [35] | triangular | B - discrete | PIN diode | 10 V | 10 | 3.3 | 60 % | 180 | 0.42 |
| [36] | square | A - discrete | PIN diode | 10 V | 8.9 | 3.7 | 10 % | 225 | 0.06 |

The methodology for designing tunable patch filters proposed in this thesis involves the design of the fixed patch filters, a mode-coupling analysis, and the tuning element analysis. These points are described in details in the next chapter.

## 2.2 PATCH RESONATORS - FUNDAMENTALS

Planar filters are basically realized on two metal layers with a dielectric substrate in between, as shown in Figure 2a. The main substrate characteristics that determine the dimensions of the filter are the thickness *h* of the dielectric layer, its dielectric constant or relative permittivity $\varepsilon_r$, and the thickness *t* of the metal layers. Other parameters such as the dielectric loss tangent tan ($\delta$) and the metal conductivity $\sigma$ affect the filter performance, in terms of insertion loss.

Planar filters are typically fabricated on the top metal layer, as illustrated in Figure 2b, and sometimes, metal vias are used to make a connection to the ground plane (the bottom metal layer). Some topologies have also electromagnetic band-gap structures (EBG) etched in the ground plane to add a rejection characteristic to the filter response.

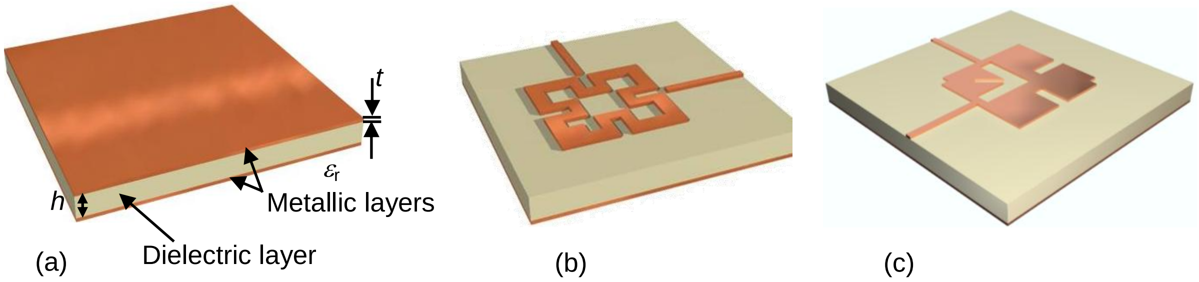

Figure 2 – (a) Planar filters substrate; (b) Example of a fabricated microstrip filter; (c) Example of a fabricated patch filter[37].

Fundamentally, there are the one-dimensional and the two-dimensional planar filters. The first type are the traditional microstrip filters, formed by resonators such as step impedance resonators (SIR), edge- and parallel-coupled lines, hairpin, interdigital, combline etc. This work is focused on the second type of planar filters, the patch filters, which are not based on transmission lines, as the microstrip filters, but on two-dimensional geometries. The design approach for patch filters is different then that used for microstrip filters. In particular, the analysis of the EM field patterns is fundamental to understand the behavior of patch filters.

Resonators support different resonant modes, in which the applied energy is split. Each mode resonates at a particular frequency, where the lowest frequency is from the first mode, named fundamental or dominant, and is defined by the characteristics of the resonator. For frequencies higher than the fundamental mode one, there are other resonant modes, which generate spurious bands in the filter response.

When the resonator has a regular geometry, two modes may have the same resonance frequency, despite their different EM field patterns. These modes are called degenerate modes and can occur at several frequencies in the same resonator. In patch resonators, the fundamental modes are degenerate, one presenting an even and the other an odd EM field pattern.

Patch resonators can be ideally treated as waveguide cavities, of which the top and bottom layers are perfect electric walls, laterally surrounded by perfect magnetic walls. Consequently, the EM fields are transverse magnetic ($TM^z$) relative to the direction perpendicular to the ground plane, which was named *z* axis in this work. This means that there is no magnetic field component in the z axis, only an electric component $E_z$. The $TM^z$ mode has a well-known formulation and it is used for the analysis of patch filter fields. The formulation presented below accounts for the effective values of resonator dimensions and substrate dielectric constant, in order to consider real boundaries instead of perfect walls.

A complete text about patch filters theory, a detailed design methodology, patch filters characteristics and considerations, as well as Matlab-based programs, which calculate the patch resonances and the electrical field patterns for the square, circular and triangular geometries are given in my master's dissertation[34].

### 2.2.1 SQUARE PATCH RESONATOR

Figure 3 presents a square patch resonator.

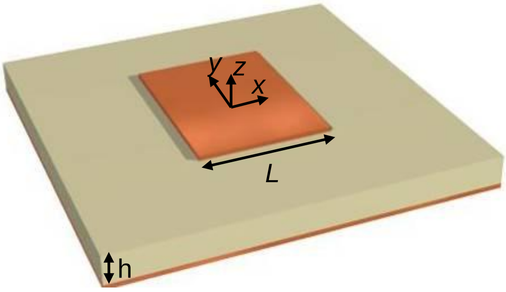

Figure 3 – Square patch resonator with length *L*.

The electric field distribution along the square resonator can be calculated by eq. (5)[38] and its corresponding resonant frequency by eq. (6)[39], deduced from patch antenna equations. It can be seen that the field patterns depend only on the square side and on the desired resonant mode indices *m* and *n*, although the frequency also depends on the substrate characteristics.

$$E_z\ \mathrm{square}(x,y) = A\cos\left(\frac{m\,\pi\,x}{L}\right)\cos\frac{1}{2}\left(\frac{n\,\pi\,y}{L}\right) \tag{5}$$

$$\mathrm{freq\ square}(m,n) = \frac{c}{2L_{\mathrm{ef}}\sqrt{\varepsilon_{\mathrm{ef}}\,\mu_{\mathrm{r}}}}\sqrt{m^2+n^2} \tag{6}$$

Where:

*A* is the electric field magnitude;

*m* and *n* are the non-negative integer $\mathrm{TM}^z_{m,n,0}$ mode indices in *x* and *y* axis directions, respectively, with the condition that *m* and *n* cannot be simultaneously null;

*x*, *y* are the coordinate axes with origin at the resonator’s geometric center;

*c* is the light speed in vacuum;

$\mu_r$ is the relative magnetic permeability ($\mu_r$ =1);

$L_{ef}$ is the effective length of the square resonator:

$$L_{ef} = L + 2|\Delta L| \tag{7}$$

with:

$$\Delta L = 0.412\,h\left(\frac{\varepsilon_{ef} + 0.3\ L/h + 0.264}{\varepsilon_{ef} - 0.258\ L/h + 0.8}\right) \tag{8}$$

If *m* = 0 or *n* = 0: $\varepsilon_{ef} = \varepsilon_{ef\ auxiliar}$ (9)

Otherwise: $\varepsilon_{ef} = \varepsilon^2_{ef\ auxiliar}/\varepsilon_r$ (10)

with: $$\varepsilon_{ef\ auxiliar} = \frac{1}{2}\left[\varepsilon_r + 1 + \frac{\varepsilon_r - 1}{\sqrt{1 + 10\left({}^{h}/_{L}\right)}}\right] \tag{11}$$

$\varepsilon_{ef}$ is the effective relative dielectric constant of the patch resonator;

$\varepsilon_r$ is the substrate relative dielectric constant;

*h* is the substrate thickness;

*L* is the length of the square resonator.

From these equations, it is simple to verify the presence of the degenerate modes as the resonant frequency remains unchanged with the exchange of *m* and *n*, whereas $E_z$ changes. This is the case of the dominant modes $TM^z_{1,0,0}$ and $TM^z_{0,1,0}$.

### 2.2.2 CIRCULAR PATCH RESONATOR

A circular patch resonator is illustrated in Figure 4, in polar coordinates.

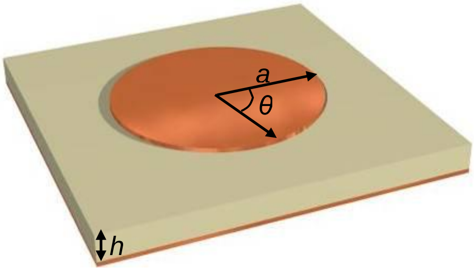

Figure 4 – Circular patch resonator with radius *a*.

The electric field distribution along this type of resonator is given by eq. (12)[40]. Similarly to the square resonator, the field distribution is only related to the resonator physical dimensions and the resonant mode indices *p* and *q*. The modal frequencies depend on those indices and also on the substrate characteristics, calculated from eq. (13)[38].

$$E_z\ \mathrm{circle}(a,\theta) = A\ \mathrm{J}\left(p, \frac{\alpha_{p,q}\, r}{a}\right) \cos(p\theta) \tag{12}$$

$$\mathrm{freq\ circle}(p,q) = \frac{\alpha_{p,q}\, c}{2\,\pi\, r_{ef}\sqrt{\varepsilon_r\, \mu_r}} \tag{13}$$

Where:

J (*p*, *r*) is the Bessel function of first kind and order *p*;

*r* is the radial variation of the radius from 0 to *a*;

*a* is the radius of the circular resonator;

*θ* is the angular variation of the radius from 0 to 2π.

*p* and *q* are the non-negative integer $TM^z_{p,q,0}$ mode indices in *θ* and *r* directions, respectively, with $q \neq 0$;

$\alpha_{p,q}$ is the $q^{th}$ zero of the derivative of the Bessel function of first kind and order *p*;

$r_{ef}$ is the effective radius of the resonator:

for $p = 0$[41]:

$$r_{ef} = a\sqrt{1 + \left({}^{2h}\!/_{\pi a \varepsilon_r}\right)\left[\ln\left({}^{a}\!/_{2h}\right) + \varepsilon_r\sqrt{2} + 1.7726 + \left({}^{h}\!/_{a}\right)(0.268\,\varepsilon_r + 1.65)\right]} \quad (14)$$

for $p \neq 0$[38]:

$$r_{ef} = a\sqrt{1 + \left({}^{2h}\!/_{\pi a \varepsilon_r}\right)\left[\ln\left({}^{\pi a}\!/_{2h}\right) + 1.7726\right]} \quad (15)$$

The frequency equation shows that the modal frequencies are directly related to the values of $\alpha_{p,q}$. The lowest values are $\alpha_{0,1} = 3.832$, $\alpha_{1,1} = 1.841$, and $\alpha_{2,1} = 3.054$, therefore the fundamental mode is $TM^z_{1,1,0}$, given by the lowest value $\alpha_{1,1}$. The degenerate modes are orthogonal to each other and can be calculated from (12) by simply rotating $\theta$ by 90º.

### 2.2.3 TRIANGULAR PATCH RESONATOR

In a triangular resonator, illustrated in Figure 5, the electric field patterns are given by eq. (16)[42] and, similarly to the other structures, depend on the resonator physical dimensions. However, in this case, the $TM^z_{s,u,v}$ mode indices $s$, $u$, and $v$ do not have any physical connotation or individual meaning, and must satisfy the condition $s + u + v = 0$. The resonant frequencies are calculated by eq. (17).

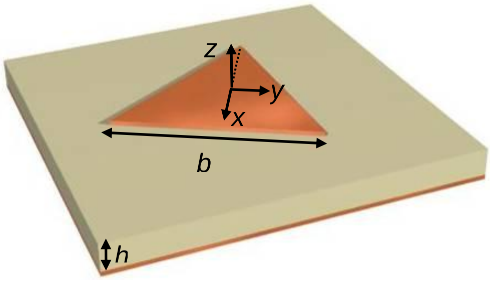

Figure 5 – Equilateral triangular patch resonator with base *b*.

$$E_z\,\text{triangle}(x,y) =$$

$$= A\left\{\cos\left[\left(\frac{2\pi x}{b\sqrt{3}} + \frac{2\pi}{3}\right)v\right]\cos\left[\left(\frac{2\pi y(s-u)}{3b}\right)\right] + \cos\left[\left(\frac{2\pi x}{b\sqrt{3}} + \frac{2\pi}{3}\right)s\right]\cos\left(\frac{2\pi y(u-v)}{3b}\right) + \cos\left[\left(\frac{2\pi x}{b\sqrt{3}} + \frac{2\pi}{3}\right)u\right]\cos\left(\frac{2\pi y(v-s)}{3b}\right)\right\} \quad (16)$$

$$freq\,\text{triangle}(s,u) = \frac{2c}{3b_{ef}\sqrt{\varepsilon_r\,\mu_r}}\sqrt{s^2 + su + u^2} \quad (17)$$

Where:

*s*, *u*, and *v* are the integer $TM^z_{s,u,v}$ mode indices;

*b* is the base of the equilateral triangular resonator;

*x* and *y* are the coordinate axes with origin at the resonator's geometric center, parallel to the height and to the base, respectively;

$b_{ef}$ is the effective base of the triangular resonator: $b_{ef} = b + h/\sqrt{\varepsilon_r}$ (18)

The exchange of the index values *s* and *u* in eq. (17) keeps the resonant frequency unchanged for any set of {*s*, *u*}. The same occurs with the field patterns in eq. (16), where every set of {*s*, *u* and *v*} that satisfy the condition $s + u + v = 0$, do not change the field pattern. Therefore, it is not possible to verify the presence of the degenerate modes through these equations.

The fundamental degenerate mode patterns are given by the set of minimum values that satisfy the condition $s + u + v = 0$, which is {0, 1 and -1}, as in the resonant modes $TM^z_{0,1,-1}$ or $TM^z_{1,0,-1}$ etc. Nevertheless, all those resonant modes show exactly the same electric field pattern according to eq. (16) and thus, another equation is required to describe the electric field pattern of the degenerate modes of the triangular patch resonator. The solution is not obvious as in the case of the circular resonator, however one approach consists in the use of the superposition principle applied to the EM fields[43]. First, by rotating the *x* and *y* axes of $\beta = 2\pi/3$ and $\varphi = -2\pi/3$, new equations for $E_z$ are formulated: $E_{z\beta}$ $(x',y')$, where $x' = x\cos\beta + y\sin\beta$ and $y' = y\cos\beta - x\sin\beta$, and $E_{z\varphi}$ $(x'',y'')$, where $x'' = x\cos\varphi + y\sin\varphi$ and $y'' = y\cos\varphi - x\sin\varphi$. The difference $E_{z\beta} - E_{z\varphi}$, generates the adequate extra electrical field patterns for the degenerate modes.

### 2.2.4 PATCH FILTERS CHARACTERISTICS

Single-mode filters are the ones in which each resonator determines a single pole in the filter passband. Single-mode patch filters have lower conductor loss and higher power handling when compared to microstrip filters. However, they occupy a larger area, and hardly achieve $FBW_{3dB}$ narrower than 5%.

In order to reduce the area of a single-mode patch filter, a useful technique is to insert a perturbation in the resonator geometry. The term perturbation is used in the context of filters to define any change in the resonator geometry. The perturbation is inserted into the resonator to increase the electrical current path of a resonant mode and thus, the corresponding modal frequency decreases. If the dominant frequency of a patch resonator is reduced without changing its dimensions, one can consider the filter miniaturized, because in order to reduce the frequency, the filter dimensions should increase. The position where the perturbation must be inserted for an effective perturbation of a specific mode is defined by the examination of the field patterns and the associated current distribution along the resonator.

A major advantage of the perturbation technique is that, when reducing the dominant frequency without (or barely) changing other modes, one can obtain higher level of second harmonic rejection in the filter frequency response. For this, one should reduce the dominant frequency $f_d$ in a manner that the frequency $2\cdot f_d$ is located on an area with good rejection of the frequency response of the resonator. Using as an example a circular patch resonator without perturbation, where the dominant frequency is 3.0 GHz, the second resonant mode frequency is 5.1 GHz, and the third resonant mode frequency is 6.0 GHz. Perturbing this resonator, its dominant frequency can be reduced to approximately 2.2 GHz maintaining the higher modes unchanged. In this way, at 4.4 GHz there will be a good attenuation as there is no resonant mode at this frequency.

As described in the beginning of this chapter, another way to miniaturize filters is the use of the dual-mode concept, which increases the order of the filter without increasing the number of resonators. Dual-mode filters are formed by dual-mode resonators, where each resonator determines two poles in the filter passband. A dual-mode patch resonator is a single-mode resonator with perturbations in its geometry, which bring the frequency of a particular mode closer to the frequency of another mode, forming the filter passband. Each of these modes works as a resonant circuit, determining a pole in the passband. From an electrical point of view, a dual-mode patch resonator is equivalent to a doubly-tuned resonant circuit and thus, a second order filter is constructed with a single resonator. Hence, the number of resonators needed to build a filter with a given order is halved thus decreasing the filter size. Another great advantage of dual-mode patch filters is the possibility to design narrow-band patch filters with $FBW_{3dB}$ of less than 5%, which is not possible with a single-mode patch filter.

Therefore, it is possible to design patch filters with two important characteristics: miniaturization and selectivity. Miniaturization occurs at two levels: by increasing the electrical current path, which reduces the modal frequency without changing the patch resonator area, and by increasing the order of the filter without increasing the number of resonators. Selectivity is also improved when changing specific resonant frequencies or when increasing the order of the filter.

# 3 DESIGN METHODOLOGY OF TUNABLE PATCH FILTERS

The synthesis technique helps the designer to produce a prototype filter network that outputs, or approximates to, a desired filter response. Based on the transfer function of the filter, after successive mathematical transformations, the synthesis technique results in the required values of couplings between resonators, between resonators and the feed lines, and between the input/output feed lines necessary to form a filter based on arbitrary topology and technology. Thus, the synthesis problem consists in determining the couplings such that a prescribed response is reproduced. These couplings, organized in a matrix, can then be translated to the dimensions of a well-known topology. The synthesis can produce different classes of filter responses as Butterworth, Chebyshev, elliptic etc. These are ideal results and do not consider losses in the network.

Since the 1960’s, several polynomial synthesis techniques have been formulated in order to theoretically analyze a filter function. Initially, the technique involved so many couplings[44] that the fabrication and adjustments could become extremely complex, and thus, unpractical. Through the years, the synthesis techniques were improved, reducing the number of coupling elements[45, 46]. In 1974, for the first time, couplings between non-adjacent resonators, besides the couplings between the adjacent resonators, were considered by Atia, Williams, and Newcomb[46], in order to accomplish a more general theory. The couplings between non-adjacent resonators were named cross-couplings. Successive similarity transformations were then applied to the coupling matrix to cancel some unwanted couplings to achieve a desired network topology. Unfortunately, sometimes the method could not converge, although for the next two decades, this technique was widely used and enhanced. Later, Cameron presented an even more comprehensive technique to synthesize even- or odd-networks with arbitrarily placed transmission zeros, asymmetric or symmetric characteristics, and singly or doubly terminated[47]. Subsequently, Amari proposed a gradient optimization technique, with a simple recursion formula to determine the low-pass prototype with arbitrarily placed transmission zeros, in which the topology constrains are included in the optimization process, forcing the final coupling matrix to take the form of a predetermined topology[48].

These techniques focused on topologies where the source and the load are coupled to only one resonator and not coupled to each other. Such topologies can produce at most $N - 2$ finite transmission zeros, considering a topology with $N$ resonators. This means that for a low order filter, such as $N < 3$, the rejection of the filter would be quite limited, because the filter would not be able to produce any finite transmission zero. In a context where the systems increasingly demand sharper filter responses and reduced filter area, this can constitute a serious drawback.

The addition of a direct signal path between the source and the load yields $N$ finite transmission zeros for a topology with $N$ resonators instead of $N - 2$. Some synthesis techniques of non-general filters with source/load coupling were then presented[49], however Amari evolved his previous gradient optimization technique to allow the realization of filters of any order with source/load couplings, in 2001[50]. In 2002, he presented a universal and comprehensive synthesis technique of coupled resonator filters with source/load-multiresonator coupling, with no need of any similarity transformation[51]. Hence, all the other techniques began to consider the source/load-multiresonator coupling. Although the coupling matrix techniques are applied to all kinds of filter technologies, only one article in the literature briefly showed a short analysis of a coupling matrix applied to the realization of a patch filter, but the synthesis methodology was not described[36].

## 3.1 COUPLING MATRIX AND COUPLING SCHEME

The most common practice in filter design is to use one resonant mode from each resonator (single-mode resonator). This is due to the topologies of the most typical cavities or microstrip filters. Although this assumption is widely used, it is not accurate for the general case of designing filters. Especially when analyzing filters using multimode resonators, as in this work, this becomes highly inadequate. As explained in chapter 2, each multimode resonator contributes with more than one resonant mode to produce specific poles in the filter passband. Under the assumption that the behavior of each mode can be approximated by a lumped LC resonator at the resonant frequency $f_0$, the usual term “resonator” used in the analysis of coupling matrix will be treated here by “resonant mode” or simply “mode”.

The synthesis optimization that considers the source/load-multimode couplings results in a coupling matrix with $N + 2$ rows and $N + 2$ columns, where $N$ is the order of the filter. The first row denotes the source, the second row denotes the first resonant mode, the third row denotes the second resonant mode…, up to the penultimate row ($N + 1$), which denotes the last resonant mode, and the last row ($N + 2$), which denotes the load. The columns are related to each filter part: source, resonant modes, and load in an analogous manner. For a general formulation, $M_{AB}$ is the matrix element in the row relative to the filter part $A$ and column relative to filter part $B$. For example, for a third order filter ($N = 3$), its general coupling matrix $M$ is shown in eq. (19), where $S$ designates source, the numbers 1 to $N$ designate each lossless resonant mode, and $L$ designates load.

$$M_{3^{rd}order} = \begin{bmatrix} M_{SS} & M_{S1} & M_{S2} & M_{S3} & M_{SL} \\ M_{1S} & M_{11} & M_{12} & M_{13} & M_{1L} \\ M_{2S} & M_{21} & M_{22} & M_{23} & M_{2L} \\ M_{3S} & M_{31} & M_{32} & M_{33} & M_{3L} \\ M_{LS} & M_{L1} & M_{L2} & M_{L3} & M_{LL} \end{bmatrix} \tag{19}$$

The matrix element placed across a row and a column represents the coupling between the filter parts corresponding to the row and column. It means that the matrix element $M_{S2}$, for example, is the coupling coefficient between source and resonant mode 2, or $M_{31}$ is the coupling coefficient between resonant modes 3 and 1. All the coupling coefficients of the matrix are normalized, and thus, frequency-independent.

From the coupling matrix, one can obtain the theoretical curves of the reflection coefficient $S_{11}$, known as return loss (RL) and the transmission coefficient $S_{21}$, known as insertion loss (IL) as a function of the frequency. For that, the filter network is considered to be excited by a voltage source with internal impedance $R_i$ and magnitude equal to unity, whereas the load terminal impedance is $R_o$. Using the Kirchhoff's voltage law, which states that the algebraic sum of the voltage drops around any closed path in a network is zero, one can obtain the loop current equations expressed in a matrix form and grouped in a vector [$I$] in eq. (20)[51].

$$[-jR + \omega' W + M][I] = [A][I] = -j[e] \tag{20}$$

Where:

$j^2 = -1$;

[$R$] is a $(N + 2) \times (N + 2)$ matrix, in which only nonzero entries are $R_{11} = R_i$ and $R_{N+2, N+2} = R_o$, both normalized to 1 (the reference is 50 Ω);

[$W$] is a $(N + 2) \times (N + 2)$ identity matrix, with $W_{11} = W_{N+2, N+2} = 0$;

$\omega'$ is the lowpass prototype normalized angular frequency given by eq. (21):

$$\omega' = \frac{\omega_c}{\Delta\omega}\left(\frac{\omega}{\omega_c} - \frac{\omega_c}{\omega}\right) \tag{21}$$

Where:

$\omega_c$ is the center angular frequency of the filter;

$\Delta\omega$ is the bandwidth of the filter;

[M] is the coupling matrix;

[$e$] is a (1 x $N$) vector that represents the filter stimulus, in which only nonzero entry is $e_{11} = 1$.

Finally, the scattering parameters curves are given by eq. (22) and (23)[51].

$$S_{21} = -2j[A^{-1}]_{N+2,1} \tag{22}$$

$$S_{11} = 1 + 2j[A^{-1}]_{11} \tag{23}$$

Some clarifications about the coupling matrix are highly important in order to better understand its relation to the characteristics of the filter centered at $f_c$:

- $M_{SS}$ and $M_{LL}$ have no meaning and are always null-terms.
- The main diagonal elements, except for $M_{SS}$ and $M_{LL}$, exist in asynchronous tuned networks, where each resonant mode has a different resonant frequency. The main diagonal elements represent the offsets from filter's center frequency of each resonant mode frequency, also called susceptances;
- If the self-resonant frequency of mode $A$, $f_{0A}$, is higher than the filter center frequency $f_c$, $M_{AA}$ is negative, and if it is lower, $M_{AA}$ is positive.
- The farther the resonant mode frequency $f_{0A}$ from the filter's center frequency, the higher the magnitude of $M_{AA}$.
- The self-resonant frequency of each mode can be calculated directly from the diagonal elements as given by eq (24).

$$f_{0A} = -f_c\left(M_{AA} \cdot BW_{3dB} - \sqrt{{M_{AA}}^2 \cdot BW_{3dB}^2 + 4}\right)/2 \tag{24}$$

- The normalized coupling coefficient $M_{AB}$ between two resonant modes $A$ and $B$ can be determined from eq. (25)[52], where $f_A$ and $f_B$ are the resonant frequency of each mode when they are coupled to each other.

$$M_{AB} = \pm\frac{1}{2}\left(\frac{f_{0A}}{f_{0B}} + \frac{f_{0B}}{f_{0A}}\right)\sqrt{\left(\frac{f_A^2 - f_B^2}{f_A^2 + f_B^2}\right)^2 - \left(\frac{f_{0A}^2 - f_{0B}^2}{f_{0A}^2 + f_{0B}^2}\right)^2} \tag{25}$$

- If two resonant modes $A$ and $B$ are not coupled to each other, $f_A = f_{0A}$, and $f_B = f_{0B}$, leading to $M_{AB} = 0$.

- The center frequency of the filter is the geometric mean of all the resonant frequencies calculated by (24), given by (26).

$$f_c = \left(\prod_{i=1}^{N} f_i\right)^{1/N} \tag{26}$$

- The coupling coefficient +/- sign of the matrix elements $M_{SA}$ and $M_{AL}$ indicates the coupling of an even- ($M_{SA} = M_{AL}$) or odd-mode ($M_{SA} = -M_{AL}$). These elements symbolize the external quality factor $q_{SA}$ and $q_{AL}$ of the input and output, calculated from eq. (27).

$$q_{SA} = \frac{1}{M_{SA}^2} \tag{27}$$

- A symmetrical frequency response indicates the equality of the coupling between source (or load) and each resonant mode, i.e. $|M_{SA}| = |M_{SB}|$ and $|M_{LA}| = |M_{LB}|$.
- The condition $|M_{AB}|= |M_{BA}|$, indicates that symmetrical couplings have been assumed for obtaining a symmetrical layout, and their signs indicates a capacitive or inductive coupling.

In some filter layouts, it is very easy to identify the couplings between source, load, and resonators, as in the case of single-mode microstrip filters. Inversely, it can be extremely hard to identify the couplings by just looking at the layout of multi-mode resonators. For this case, which is the case of multi-mode patch resonators, an interpretation of the couplings is necessary to model the filter behavior and find the coupling matrix coefficients.

The couplings in a filter can also be expressed in a diagram form, called coupling scheme. The coupling scheme is a diagram where all the filter parts are represented as black nodes (resonant modes) and white nodes (source/load), and the coupling between them, as full- or dotted-lines symbolizing a direct coupling or an admittance inverter. One possible coupling scheme considering all couplings for the example of a 3rd-order filter is shown in Figure 6.

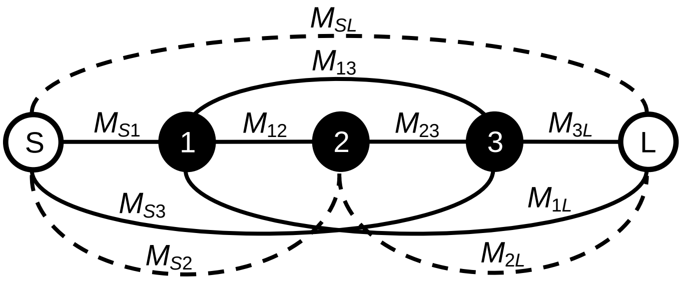

Figure 6 – Coupling scheme of a 3rd-order filter considering all possible couplings. Source and load are represented by white circles and resonators represented by black circles.

The maximum number of possible transmission zeros (*TZ*) of a filter with source/load-multimode couplings is given by the existent path from the source to load. It can be determined by the order of the filter (*N*) minus the number of resonant modes of the shortest path between source and load. TZ = *N* means that there is a coupling between source and load and thus, $M_{SL} \neq 0$.

The coupling scheme and the coupling matrix have a reciprocal correlation, however the relation between the filter response and the coupling matrix or between the filter response and the coupling scheme is not unique, as the coupling matrix is derived from mathematical techniques, which can assume different configurations and still present the same response. Thus, it is a matter of interpretation of the couplings to achieve the desired filter response. The same coupling scheme or matrix can represent the couplings of different filter topologies fabricated in any technology. On the other hand, different coupling schemes or matrices can represent the same filter. Hence, the analysis and determination of the coupling matrix is of great importance to understand and predict the behavior of a filter. From one side, it is useful to know which couplings should be changed to improve a filter response, and transfer this information to the filter layout, and on the other hand, the constraints of the layout can be considered to carry out the matrix and ensure a feasible filter.

In multimode patch filters, an interpretation of the coupling scheme is necessary as the resonant modes are distributed along the same patch resonator and their equivalent electrical circuits are not obvious. Then, it is important to use powerful tools, such as 3D EM simulators in order to identify the field patterns of interest and better understand their couplings.

Concerning reconfigurable filters, a specific synthesis technique has not been carried out yet, especially a technique that includes the impedance of the tuning element. This work proposes initial studies in this sense.

## 3.2 METHODOLOGY

The design of tunable patch filters is not simple because their equivalent circuits are not obvious to extract due to the geometry of the resonator. The formulation of patch resonators is applied to unperturbed geometries and the usual practice of modifying the patch resonator geometry with cuts and slots turns out to be excessively complex. Thus, the approach used for the design of tunable microstrip filters cannot be used to design a patch filter, much less to design tunable patch filters. It is difficult to analyze all the couplings in a patch filter independently, due to the simultaneous presence of the modes in the same resonator. There is not an effective method that isolates the equivalent electrical circuit of each mode and relates it to a specific part of the filter layout. Even harder is to assess the effect of a tuning element on one or more modes of the patch resonator. In view of this, a methodology is proposed and presented here to help on the analysis and design of tunable patch filters. A general view of the proposed methodology is presented in Figure 7.

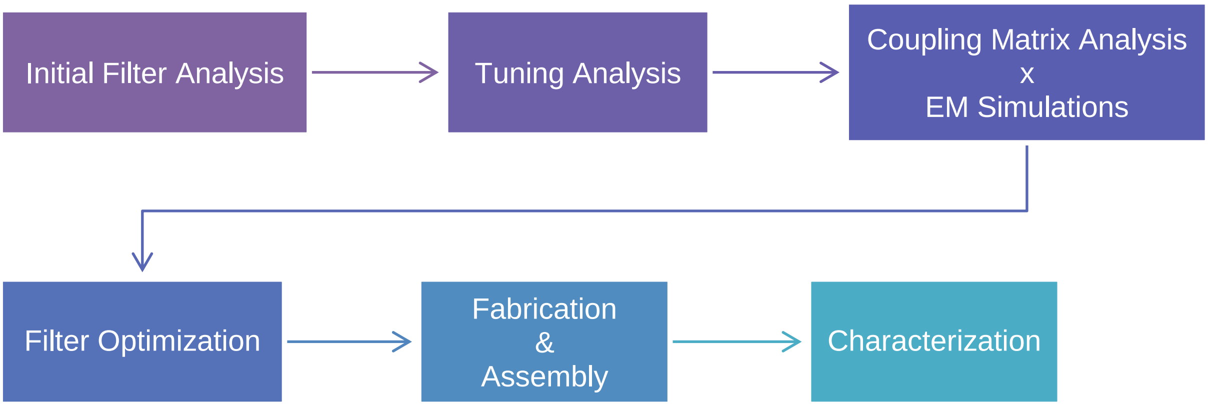

Figure 7 - Methodology for designing tunable patch filters.

### 3.2.1 INITIAL FILTER ANALYSIS

Initially, the tuning characteristics should be defined in order to determine the filter topology and the necessary coupling between the resonant modes. As showed before in chapter 2, there are four general categories of tunable bandpass filters:

- $f_c$ tuning and constant bandwidth;
- Constant $f_c$ and bandwidth tuning;
- Simultaneously $f_c$ and bandwidth tuning, without independent control;
- Selectivity tuning.

For each type of tuning goal, there is a different design technique. The technique for designing filters with center frequency tunability involves the change of the electrical length of the resonators. The technique for tuning the filter bandwidth is more complex because it involves the change of inter-resonator couplings, which cannot always be done individually, affecting the overall response of the filter. In practice, sometimes, the design does not allow the change of the filter center frequency without changing its bandwidth, and vice-versa. If this behavior is not acceptable, another topology should be selected.

The initial resonator and its physical dimensions are determined according to the desired operating frequency for the filter. The dimensions can be calculated from the equations given in section 2.2, with initial perturbations chosen by considering the electric field patterns along the resonator. The design process involves iterative steps in order to achieve the desired characteristics. The coupling between the resonant modes is determined by inserting perturbations to the patch geometry, such as slots, cuts, or adding small patches. This should be carefully analyzed in order to understand how the perturbations change the modes coupling.

3D-EM simulators provide a full electromagnetic response of any kind of structure and all the couplings involved in the layout. Among the commercial available 3D-EM simulators, the *Advanced Design System* (ADS) software, from Agilent Technologies, was chosen to be used in this work. In ADS, there are two types of 3D-EM simulators. A 3D full-wave EM simulator based on the Finite Element Method, called FEM, and a 3D-planar frequency-domain simulator based on the Method of Moments, called Momentum. Only Momentum was used due to the excellent trade-off between results accuracy and simulation time for the type of structures simulated in this work. Besides the accurate filter frequency response, it also allows different analyses required for the design of tunable patch filters by setting the right layout and parameters, as it will be further explained in this chapter.

The traditional EM analysis consists in simulating the filter layout and changing its geometry in a way to obtain the desired couplings. For the design of tunable patch filters, the focus is to find one or more perturbations, which variations on its dimensions will result in the behavior for the desired tunable patch filter. The tuning element will be later integrated to the perturbations in order to electronically change them and control the selected characteristics. These initial simulations are lossless, which means that they do not consider any substrate loss. The losses will be considered at the last step of the methodology, so the loss origin in the filter response can be correctly assessed.

An interpretation of the EM simulations is necessary to determine the nature of the coupling existing between the resonant modes and the feed lines in the patch resonator and then define the corresponding coupling topology for the filter. The interpretation also allows the extraction of some parameters, such as the resonant frequency $f$ of each mode when coupled to other modes, the external quality factors evaluated at the individual resonant frequencies, the self-resonant frequency $f_0$ of each mode, etc. This is of great importance because the parameters extracted from the simulations are used to calculate the initial coupling matrix coefficients.

Simulations of the filter using the feed lines weakly coupled to the resonator give the resonant frequencies $f$ of each mode when coupled to other modes. On the other hand, the self-resonant frequencies $f_0$ of each mode can be excited by using the method of placing a magnetic wall or an electric wall in the filter symmetry axis[52]. This will excite only the even modes or the odd modes, respectively. Unfortunately, ADS does not have a tool to simulate symmetric electric and magnetic boundaries. Then, HFSS$^{TM}$, from Ansoft, another 3D full-wave EM simulator was used for this specific simulation. The simulations carried out with HFSS were used as a confirmation of the theory and particularly in this work, were not essentially necessary.

A more careful inspection of eq. (25) leads to some interesting inferences regarding the coupling between two resonant modes $A$ and $B$. If the filter is synchronously tuned, where all resonant modes have the same frequency ($f_{0A} = f_{0B}$), then the equation is reduced to the well-known formula given in eq. (28).

$$M_{AB} = \pm \frac{f_A^2 - f_B^2}{f_A^2 + f_B^2} \tag{28}$$

On the other hand, if the filter is asynchronously tuned, where each resonant mode has a different frequency ($f_{0A} \neq f_{0B}$), the equation is more complex, and is calculated as given in eq. (25). This is the case of the filters studied in this work. Moreover, if the modes are uncoupled, their coupling coefficient is null ($M_{AB} = 0$), and thus, $f_{0A} = f_A$ and $f_{0B} = f_B$. This is an important observation, which leads to the choice of the coupling scheme of the filter.

Finally, by exciting the structure with only one of the feed lines, it is possible to determine the external quality factor $Q_e$ by extracting the coupling between the feed line and the excited modes. A well-known method for calculating $Q_e$ from the $S_{11}$ curve of the filter is by measuring the bandwidth $\Delta f_{\pm 90^0}$ where the mode phase changes $\pm 90^0$ with respect to the phase of the resonant frequency $f_A$ [53]:

$$q_{SA} = \frac{f_A}{\Delta f_{\pm 90^\circ}} \tag{29}$$

With the equations given in this section, in addition to those given in section 3.1, an initial coupling matrix can be built and its coefficients adjusted so that its frequency response matches the simulated curve from the 3D EM simulator. All the curves presented in this work were simulated in Momentum – ADS, except where indicated.

Because the coupling matrix coefficients are frequency-independent, the center frequency and bandwidth of the filter are considered only when calculating the de-normalized theoretical frequency response of the filter using equations (20) to (23). A Matlab routine for a general filter of order *N* was developed for this purpose. It can be found in the appendix of the thesis.

### 3.2.2 TUNING ANALYSIS

The tuning analysis consists in determining the tuning element, which can be varactor diodes, MEMS switches or capacitances, PIN diodes, or any type of commercial or custom device that changes the filter response as the desired tuning behavior.

There are mainly two ways to simulate the tuning elements: by either drawing the structure integrated to the filter layout or using its equivalent electrical model. The simulation results indicate the appropriated position of the tuning element in the filter layout, its range of values for the desired filter operation, the dimensions of the tuning element, the influence of packaging or wire bonding, depending on the tuning element used.

When using the equivalent electrical circuit model, first, the tuning element should be characterized in order to extract its equivalent electrical model. Then, another simulation procedure must be used because the EM simulator does not allow the connection of lumped elements, such as resistors, inductors, or capacitors, directly in the layout. In order to verify the influence of the tuning element in the filter response, electrical simulations are made based on the EM simulations. For that, in Momentum, the ADS layout environment, internal ports are placed in the filter layout where the lumped elements should be connected, as shown in Figure 8.

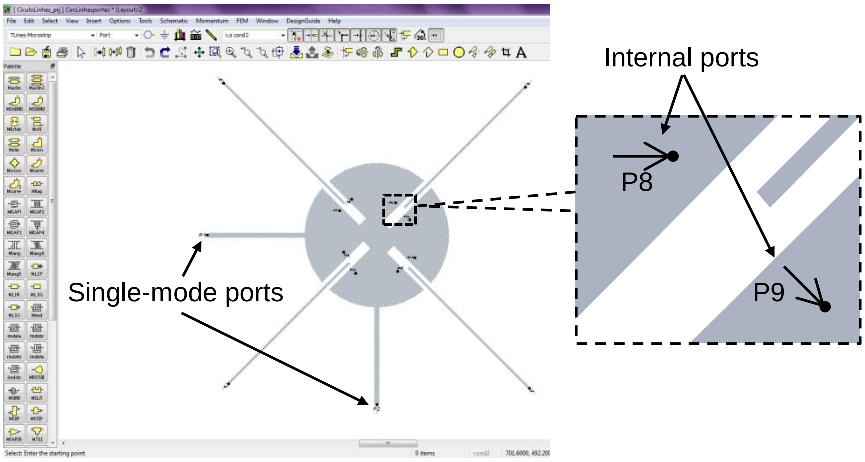

Figure 8 – Filter layout in Momentum environment with two single-mode ports (input and output) and several internal ports where the lumped elements of the tuning element model can be connected in the schematic environment.

After the regular EM simulation, a model of this layout is generated encompassing the S-parameters matrix over the entire frequency range simulated in Momentum. The model becomes available to be imported into the schematic environment. Then, lumped tuning elements can be connected to the model's ports, and the electrical simulations can be performed considering the previous EM results, as shown in Figure 9.

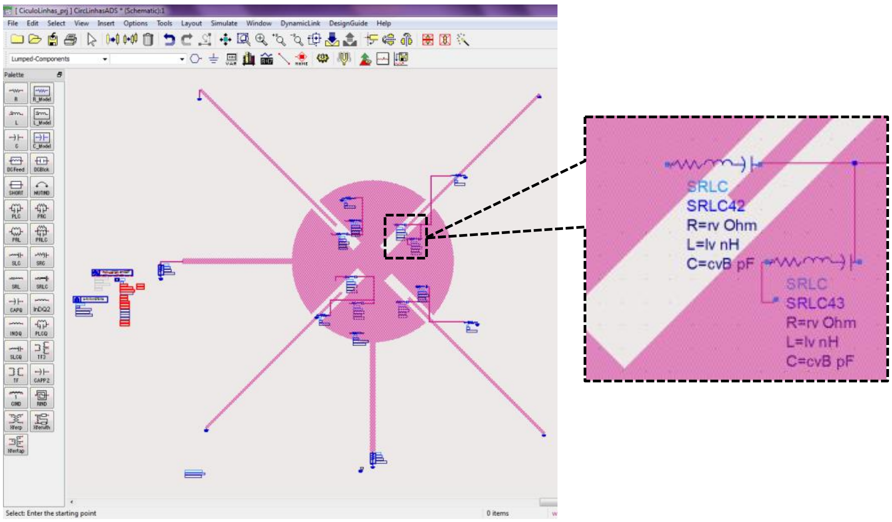

Figure 9 – Filter model with the S-parameters matrix imported to the schematic environment, ADS, with lumped tuning elements connected to the internal ports.

### 3.2.3 COUPLING MATRIX ANALYSIS VERSUS EM SIMULATIONS

Through the coupling matrix, it is possible to change the coupling coefficients in order to verify their effect on the filter response and compare to the effect of each tuning element on the simulation. This theoretical analysis allows us to verify what kind of frequency responses the filter under analysis is able to produce.

The principle followed in the design is to force the element under consideration in the layout to give the same response as the corresponding coefficients in the coupling matrix, or vice-versa, at least over a small range of frequencies around the passband. The proposed design methodology is based on the determination of a specific coupling by matching the scattering parameters of the corresponding elements in the coupling matrix with those obtained from the complete simulations of the structure until the desired frequency response is achieved.

The simulations at this point are the most complete ones, including the equivalent electrical model of the tuning elements, extracted in a step before, and the substrate losses.

A trial version of commercial software, called CoupleFil[54], was used to synthesize the coupling matrix and verify the method presented here. Basically, the software asks for the filter order and frequency response characteristics to generate a coupling matrix corresponding to a given coupling scheme. It also provides a tool to calculate the scattering parameters curves from a coupling matrix with the choice of using resonators with infinite or finite $Q$.

### 3.2.4 FILTER OPTIMIZATION

The filter optimization procedure corresponds to a recursive process carried out in each step of the design methodology. During the simulations and coupling matrix analysis, the filter design should be changed in order to meet the desired parameters for the final tunable filter. The modifications should concern the type of perturbation if the nature of the coupling is not the expected one, or concern only dimensions of the perturbations or of the resonator if the tuning range is out of range. The tunability of the tuning element should be also considered in the optimization process in order to match the tuning requirements.

Lastly, the layout is modified to allow the connection of the tuning elements and the application of the bias voltage. Sometimes these modifications can affect the filter response, thus the filter should be simulated considering them. Only after, the filter is ready to be fabricated.

### 3.2.5 FABRICATION AND ASSEMBLY

The patch filters designed were manufactured using two different processes: chemical or mechanical.

In the chemical process, a flexible mask is generated from the designed layout and recorded on the substrate using traditional photolithographic process. The copper layer of the substrate is selectively protected with a photoresist and then etched in a chemical solution of ferric chloride. This process has low precision, highly operator dependent, and therefore not reproducible. However, it can be used with satisfactory results in topologies with dimensions larger than 300 µm, and with layouts where small variations in the dimensions are not critical for the device performance.

The mechanical process uses a computer controlled micro-milling machine that cuts out the required regions of the substrate to form the filter topology informed by dedicated software. This process is highly accurate, with a precision of the order of 1 µm, highly reliable and reproducible. Gaps smaller than 100 µm are feasible with this machine.

In order to facilitate the filters fabrication, reduce costs and make them commercially attractive, commercial microwave flexible substrates were also used, providing flexibility to the filters design.

After the fabrication process, the tuning elements and the bias circuit components were directly soldered on the device.

### 3.2.6 CHARACTERIZATION

The fabricated filters were characterized by measuring their scattering parameters as a function of frequency. The measurements were performed using Vector Network Analyzers from Agilent Technologies, HP8722D and HP8510C, available at the laboratories at the Polytechnic School of USP and at IMEP-LAHC.

Another important characterization performed in this work was the filter performance with increasing power levels. The filter performance is affected by the nonlinear behavior of tuning elements added to the patch resonators, as varactor diodes. In order to investigate the power capability of the designed tunable patch filters, the 1-dB compression point ($P_{1dB}$) and the 3rd order intermodulation component levels were experimentally determined.

The tunable patch filter's $P_{1dB}$ was measured with the setup presented in Figure 10.

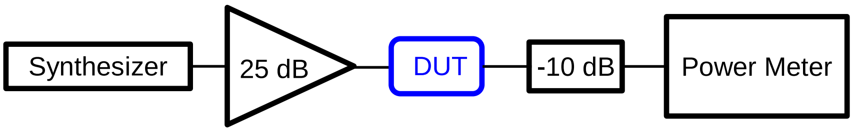

Figure 10 – Setup for the measurement of the 1-dB compression point.

The signal distortion of the tunable patch filters was investigated using the measurement setup shown in Figure 11.

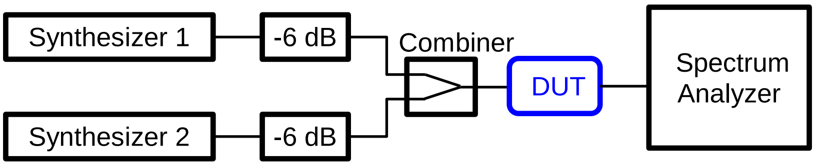

Figure 11 – Setup configuration for the measurement of the third-order intercept point.

### 3.2.7 CHAPTER SUMMARY

In this chapter, the proposed methodology for designing tunable patch filters was detailed. The methodology consists on the analysis of the resonant modes that form the filter passband. It provides the techniques to extract the coupling scheme that models the filter behavior and the necessary equations for calculating the corresponding coupling matrix. For that, EM simulations are of major importance. In this methodology, the lossless simulations should be compared to simulations considering the substrate dielectric and conductor losses and the equivalent electrical model of the tuning element in order to assess their effects. Then, a theoretical study analyzing the coupling matrix coefficients should be used for comparison with the simulation results considering the tuning elements. This allows the correct model of the tuning effect and the definition of the tuning possibilities and limits.

The fabrication and assembly of the filters proposed in this work do not demand any particular process, using traditional photolithography on commercial microwave substrate. The characterization is made at small signals, measuring the S-parameters versus frequency. Nonlinear measurements at higher power levels are also performed in order to determine the 1-dB compression point and the third-order intercept point.

This methodology is applied to the design, fabrication and characterization of a tunable dual-mode triangular patch filter, detailed in chapter 4, and a tunable triple-mode circular patch filter detailed in chapter 5.

# 4 TUNABLE TRIANGULAR PATCH FILTER WITH INDEPENDENT CENTER FREQUENCY AND BANDWIDTH CONTROLS

This section describes the design of a tunable dual-mode bandpass miniaturized patch filter, with independent tunability of center frequency and bandwidth, both with continuous control. The tunable patch filter, initially centered at 3.8 GHz, uses a modified equilateral triangular resonator with capacitances placed along the slots etched in the patch. All the simulations were made using the Rogers Duroid substrate RO3210 with a thickness of 25 mils, and a dielectric constant $\varepsilon_r = 10.2$.

The chosen topology was proposed in my master dissertation using a triangular patch resonator with an inverted "T" shape slot[34]. Some other designs of triangular patch filters with slots were also presented in the literature[55, 56]. However, the use of the inverted T shape slot provides two transmission zeros around the passband, improving the filter rejection, and allows a greater miniaturization compared to both previous works.

## 4.1 INITIAL FILTER ANALYSIS

The degenerate fundamental modes in a triangular patch resonator without perturbations, presented in Figure 12, clearly distinguishing the odd (a) and the even (b) modes. The corresponding current distributions simulated with a weak coupling between the input/output and the resonator are also shown in this figure.

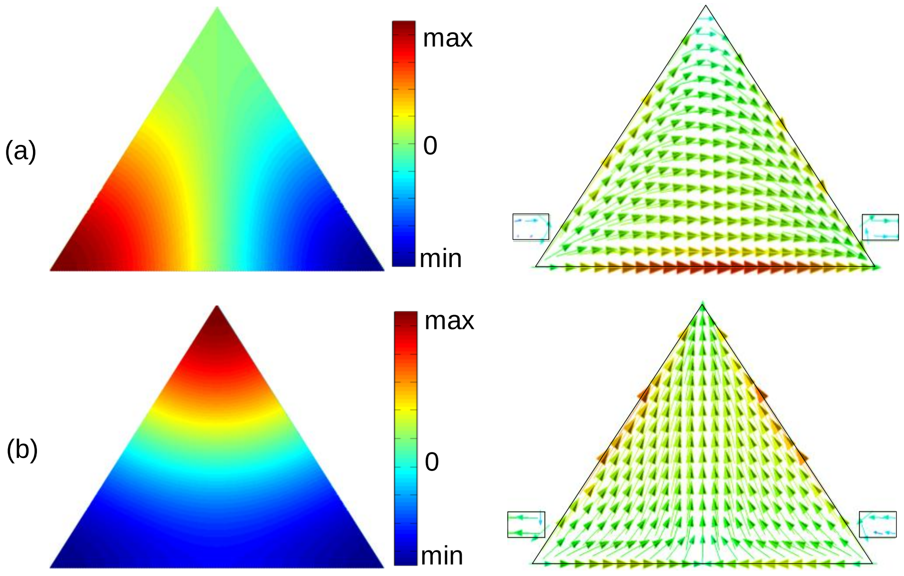

Figure 12 – Unperturbed electrical field pattern (left) and the corresponding current distribution (right) (a) Odd-mode and (b) Even-mode.

Initially, the effect on the fundamental degenerated modes behavior of the perturbations' position and dimensions of the triangular patch resonator, shown in Figure 13, was investigated. A detailed analysis was made through lossless EM simulations and showed how each slot affects and splits the two degenerate dominant modes[57]. It is easy to verify from Figure 12 and Figure 13 that the vertical slot will perturb mainly the odd-mode whereas the horizontal slot will perturb mainly the even-mode.

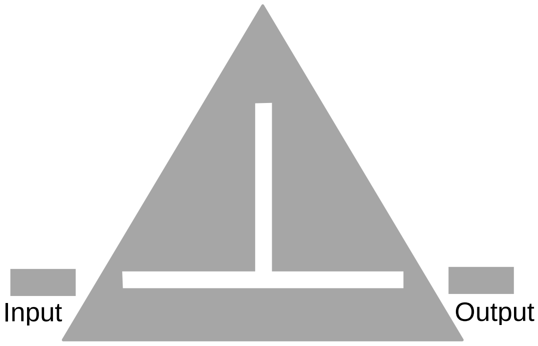

Figure 13 – Layout of the triangular patch resonator weakly coupled to the input and output, with a vertical and a horizontal slot.

Indeed, the simulations showed that a variation in the length of the vertical slot can change the odd-mode frequency $f_1$, without changing the even-mode frequency $f_2$. The horizontal slot works analogously, affecting only the even-mode frequency. This denotes that the degenerate split modes are not coupled, because $f_1$ and $f_2$ when using a vertical or a horizontal slot, respectively, are equal to the split frequencies using both slots. If the degenerate modes are not coupled to each other, each modal frequency can be tuned independently. Threfore it becomes possible to independently control the center frequency and the bandwidth of the filter.

Further, simulations with only one feed line at a time have demonstrated that both modes are excited, indicating that both are coupled to both ports. In this initial analysis, there are no evidences of the existence of coupling between source and load ($M_{SL}$), thus, this filter can be modeled in a first approach by the coupling scheme shown in Figure 14, where the node "1" represents the odd-mode, and the node "2" represents the even-mode.

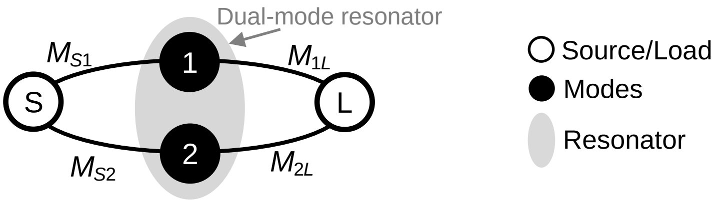

Figure 14 – Initial coupling scheme of the triangular patch filter with one single (dual-mode) resonator supporting the two degenerate modes.

The maximum center frequency of the filter was specified to be 3.8 GHz. The filter was initially optimized to reach this frequency by adjusting the slots dimensions and the position of the feed lines, as illustrated in Figure 15. The substrate considered was the Rogers™ substrate RO3210 with thickness of 25 mils, and dielectric constant $\varepsilon_r = 10.2$, initially without losses. The filter frequency response is shown in Figure 16. The filter is centered at 3.8 GHz, with a very narrow bandwidth of 1.4 %. Two transmission zeros (*TZs*) at real frequencies are located at each side of the passband at 3.2 GHz and 4.0 GHz, respectively. The current distribution of each mode showed that the even-mode exhibits a lower frequency than the odd-mode.

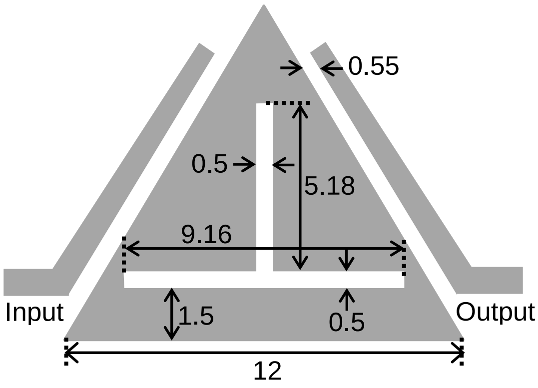

Figure 15 – Layout of the triangular patch filter with dimensions in mm.

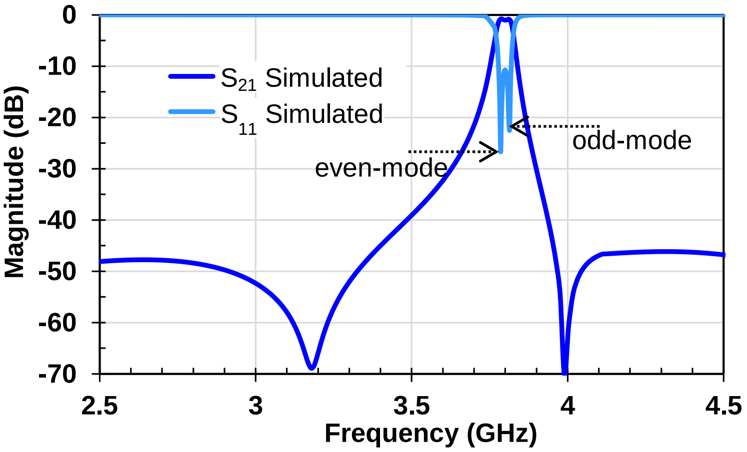

Figure 16 – Frequency response of the triangular patch filter from the EM simulations without considering any substrate loss.

The two *TZ*s in the frequency response of this second order filter ($TZ = N = 2$) show that the source is coupled to the load ($M_{SL} \neq 0$). This is a parasitic coupling that is due to the presence of higher modes in the structure, which provide additional paths between the input and output. The parasitic coupling is much weaker than the other coupling coefficients in the structure, as the positions of the two *TZ* demonstrate. The stronger this coupling, the closer the *TZ* are to the center frequency.

Finally, the complete scheme of the triangular patch filter is presented in Figure 17.

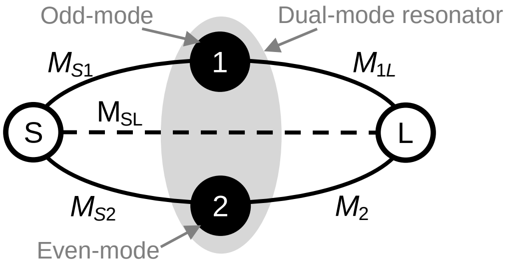

Figure 17 – Complete coupling scheme of the triangular patch filter with one single (dual-mode) resonator supporting the two fundamental degenerate modes.

The coupling matrix format corresponding to this coupling scheme is given in (30). From the initial analysis of the degenerate mode patterns, it should be expected that for the odd-mode $M_{S1} = -M_{1L}$ and for the even-mode $M_{S2} = M_{2L}$. Using specialized software[54], the coupling values were calculated considering a RL of 10 dB to match the simulated frequency response. The resulting coupling matrix is given in (31), denoted by $M_\Delta$, where the index Δ was used to refer to the triangular resonator. These values are consistent with the equations and techniques presented in chapter 3, confirming the interest of the EM analysis simulations to calculate the matrix coefficients.

The theoretical frequency response of the filter calculated from (22) and (23) are presented in Figure 18 considering the filter centered at 3.8 GHz and with $\mathrm{FBW_{3dB}}$ of 1.4 %, and the frequency response obtained from EM simulations neglecting any dielectric and conductor losses of the substrate. Both curves are in very good agreement, hence corroborating this analysis.

$$M_\Delta = \begin{bmatrix} 0 & M_{S1} & M_{S2} & M_{SL} \\ M_{S1} & M_{11} & 0 & M_{1L} \\ M_{S2} & 0 & M_{22} & M_{2L} \\ M_{SL} & M_{1L} & M_{2L} & 0 \end{bmatrix} \tag{30}$$

$$M_\Delta = \begin{bmatrix} 0 & -0.5759 & 0.6341 & -0.0036 \\ -0.5759 & -1.0427 & 0 & 0.5759 \\ 0.6341 & 0 & 0.8564 & 0.6341 \\ -0.0036 & 0.5759 & 0.6341 & 0 \end{bmatrix} \tag{31}$$

It can be seen in the inset in Figure 18 that there is a difference of approximately 1 dB in the passband IL between the lossless simulated curve and the theoretical curve. As neither conductor nor dielectric losses were considered in the EM simulations, and because the feed lines are capacitively coupled to the resonator, this difference represents the radiation loss. This can be compensated by increasing the coupling between feed lines and resonator, as discussed further in section 4.4.

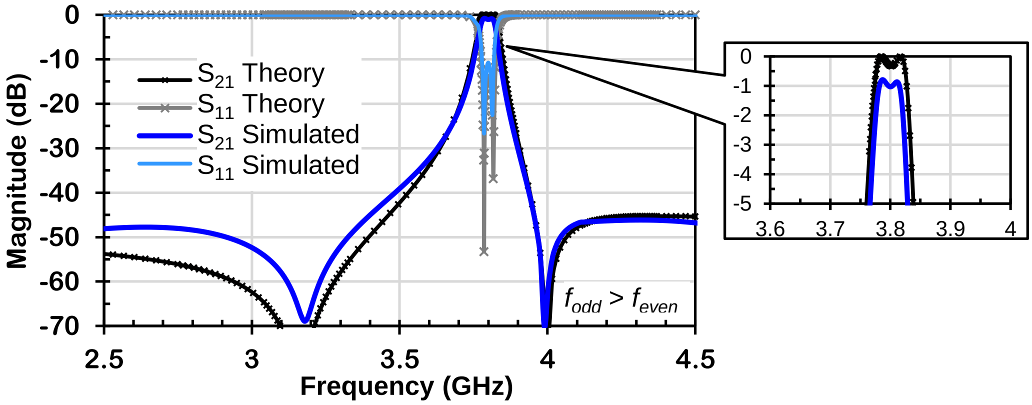

Figure 18 – Simulated (lossless substrate) and theoretical (from matrix $M_\Delta$ in (31)) responses of the triangular patch filter. An inset of the passband is shown on the upper right corner.

From the calculated coupling matrix in (31), it is possible to verify the very weak coupling between source and load through the very low $M_{SL}$ value of -0.0036. Besides, the asymmetrical frequency response is verified by $M_{S1} \neq M_{S2}$. The elements $M_{11} < 0$ and $M_{22} > 0$ implies that $f_{odd} > f_{even}$, confirming the EM simulation results presented in Figure 16, where the odd-mode frequency is higher than the even-mode frequency.

Moreover, the filter exhibited two transmission zeros at real frequencies located at each side of the passband. If the mode frequencies are changed in a manner that $f_{odd} < f_{even}$, the transmission zeros are moved to imaginary frequencies, as seen in the frequency response in Figure 19(a), as a result of the coupling matrix (31) where only the signs of $M_{11}$ *and* $M_{22}$ were changed. When $f_{odd} = f_{even}$, $M_{11} = M_{22} = 0$, there is a destructive superposition of both modes at the central frequency, leading to a significant rejection at the center frequency, as seen in Figure 19(b).

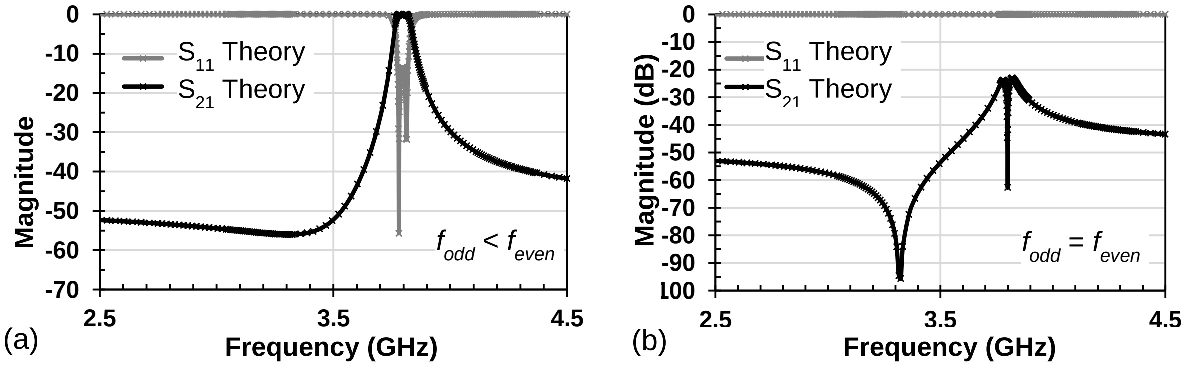

Figure 19 – Theoretical responses of the triangular patch filter when (a) $f_{odd} < f_{even}$ and (b) $f_{odd} = f_{even}$.

## 4.2 TUNING ANALYSIS

In order to realize a tunable filter, the capacitances $C_1$, and $C_2$ were positioned across the slots of the triangular resonator. Their influence on the filter response was investigated. As shown in Figure 20, only one capacitance was placed across the vertical slot, and two capacitances were placed across the horizontal slot to keep the filter symmetry in respect the S-S' plane.

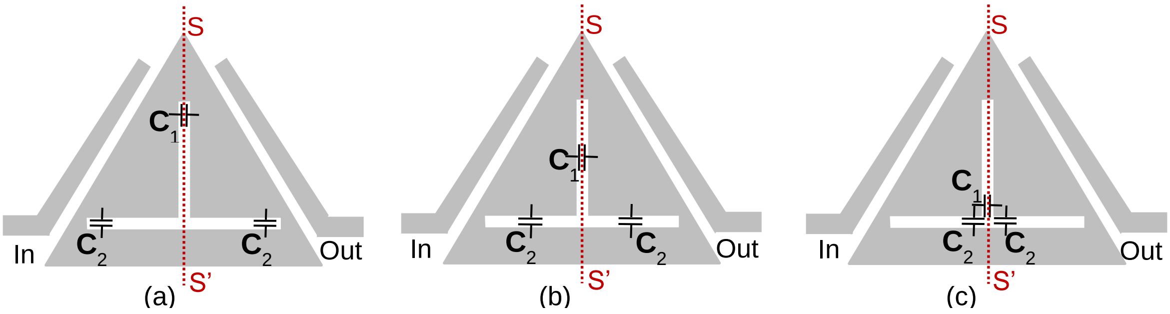

Figure 20 – Triangular patch filter with tuning capacitances at the (a) edge of each slot, (b) middle of the slots, and (c) junction of the slots.

The simulation results showed that $C_1$ controls the odd-mode's frequency without changing the even-mode's frequency. On the contrary, $C_2$ controls the even-mode's frequency without changing the odd-mode's frequency. This very important behavior means that it is possible to control the filter center frequency and bandwidth independently by choosing the correct set of capacitances. This high degree of freedom is only possible since the fundamental modes are uncoupled.

The change in modal frequencies is affected by the capacitances, as well as their position across the slots. Table 4.1 shows the influence of the capacitances' position on the tuning range, considering the filter frequency response with RL better than 10 dB. In the simulations, the IL slightly barely changed. For higher capacitances than the ones shown in Table 4.1, the RL becomes worse than 10 dB due to the mismatch of the resonator impedance. The simulated results in this table show that a maximum center frequency tuning range of 29 % is obtained when the capacitances are positioned in the middle of the slots.

In order to compare the influence of the capacitances in the center frequency response, the capacitances were also assessed within the same tuning range of 4 % from 3.81 GHz to 3.66 GHz at the three positions considered in Figure 20. Table 4.1 shows that for this range, a broader capacitance variation is needed when the capacitances are placed at the edge of the slots than when they are positioned closer to the slots junction. This is quite obvious, but very important. When the capacitors are placed at the edge of the slots, they are short-circuited by the end of the slots, and hence their influence on the resonant modes is weak. Inversely, the maximum sensitivity is obtained for capacitances placed at the slots junction. This important observation explains the effect of the series resistance when using a real model of the tuning element, for example a capacitor. The filter loss due to a capacitor's series resistance increases when the capacitor is moved towards the slots' junction, where their influence is stronger.

Table 4.1 – Simulated center frequency and capacitance ranges for different positions of the capacitances $C_1$, and $C_2$ along the slots of the triangular patch filter.

| Capacitance position | Capacitance range (pF) | Center frequency range (GHz) | Tuning range (%) |
|---|---|---|---|
| Edges of slots | 0 – 0.92 | 3.81 – 3.66 | 4 (max. range) |
| Middle of slots | 0 – 1.45 | 3.81 – 2.85 | 29 (max. range) |
| | 0 – 0.27 | 3.81 – 3.66 | 4 |
| Junction of slots | 0 – 0.20 | 3.81 – 3.52 | 8 (max. range) |
| | 0 – 0.08 | 3.81 – 3.66 | 4 |

In practice, it could be interesting to use several capacitances used for a coarse- or fine-tuning, although for simplicity, the filter was designed with capacitances in the middle of the slots, providing a large tuning range with a well-matched response.

## 4.3 VARACTOR DIODE MODEL

The tuning element used in this filter was a varactor diode. Varactor diode is a semiconductor diode that, when reversed biased below its breakdown voltage, acts as a voltage-controlled variable capacitance. The reverse voltage changes the width of its depletion layer, changing the diode junction capacitance.

There is a characteristic curve of the junction capacitance $C_j$ versus the reverse bias voltage $V$ specific to each type of diode, following eq. (32).

$$C_{\mathrm{j}} = \frac{C_{\mathrm{j}0}}{\left(1 + V/V_j\right)^{\gamma}} \tag{32}$$

Where:

$C_j$ is the reverse biased variable junction capacitance;

$C_{j0}$ is the junction capacitance without an external bias;

$V$ is the applied reverse bias voltage;

$V_j$ is the built-in junction potential;

$\gamma$ "gamma" is a coefficient relating $C_j$ and $V$. It depends on the junction doping profile.

When modeling an encapsulated varactor diode, one should take into account the parasitic elements that are mostly due to the package, in order to obtain an accurate equivalent electrical circuit model at the frequency band at which the diode will operate. For the filters developed in this work, the classical model used is shown in Figure 21, where $R_s$ represents the parasitic series resistance of the diode die, $L_s$ and $C_p$ are the parasitic inductance and capacitance due to the package. In this model, $R_s$ and $L_s$ vary with the applied voltage. In general, the capacitance $C_p$ is absorbed by $C_j$ due to its very low value, and the model becomes a simple series *RLC*. At higher microwave frequencies, say above 10 GHz, a more complete model should be extracted, taking into account $C_p$, the package material, the wires bonding, etc.

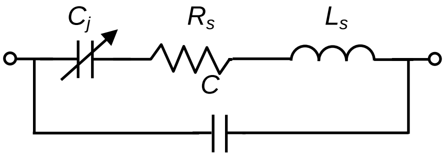

Figure 21 – Equivalent electrical model of a reversed biased varactor diode.

Normally, a typical curve $C_j$ (*V*) is given by the manufacturer for each varactor diode, as shown in Figure 22. With these curves, the more suitable diode capacitance values can be chosen for the design of the reconfigurable filters.

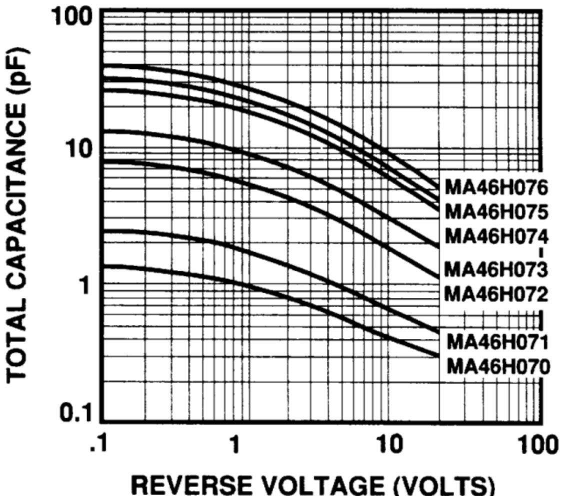

Figure 22 - Example of curves $C_j$ (*V*) for varactor diodes modelled at 1 MHz given by the manufacturer (MA46H071, from M/A-COM, used in this work).

Figure 22 shows the curve of the MA46H071 GaAs diode, from M/A-COM, which was available to be used in this work. The available data given by the manufacturer is the capacitance range vs. the reverse voltage from 0.45 pF (20 V) to 2.3 pF (0.1 V) at 1 MHz, $\gamma = 0.75$, $L_s = 0.45$ nH, and Q = 4500 (at 50 MHz). The Q-factor is defined in eq. (33).

$$Q_{u\,varactor} = \frac{1}{2\pi f\, R_s\, C} \tag{33}$$

The capacitance range of this varactor diode is slightly above the values defined by the simulations. In order to use it, a configuration with two series varactor diodes is used as illustrated in Figure 23, halving the total capacitance. The varactor diodes were connected to ground by a 10 kΩ resistor in order to provide the DC path while blocking the RF signal to ground. A back-to-back configuration was necessary as both sides of the slots are at the same potential, which would prevent biasing the diodes if directly placed across the slots. Furthermore, the back-to-back configuration has been proven to improve the nonlinearity performance, increasing the power handling of the device and improving the 1-dB compression point and the third-order interception point ($IIP_3$)[58, 29].

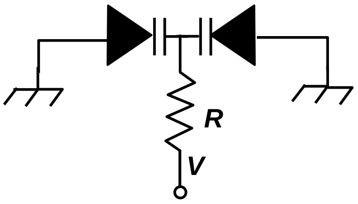

Figure 23 – Back-to-back configuration of the varactor diodes to allow biasing and improve nonlinearity.

This diode was characterized to extract its $R_sL_sC_j$ model by measuring its S-parameters for different reverse bias voltages. Then, the $R_sL_sC_j$ model was simulated in ADS and the values of $R_s$, $L_s$ and $C_j$ were adjusted so that the simulated S-parameters fit the measured data. The capacitances found at 2.45 GHz, presented in Figure 24, are slightly different from those of the manufacturer. The measurements showed that $R_s$ varies from 1.7 Ω (at 1 V) to 3 Ω (at 20 V), $L_s$ varies from 1.2 nH (at 1 V) to 1.7 nH (at 20 V), and hence, Q varies from 24 (at 1 V) to 54 (at 20 V). Despite the changes in $R_s$ and $L_s$, the values used to simulate the real varactor diode were constant, with $R_s = 2$ Ω, and $L_s = 1.3$ nH. This resulted in very good predicted responses and it was not necessary to complicate the model.

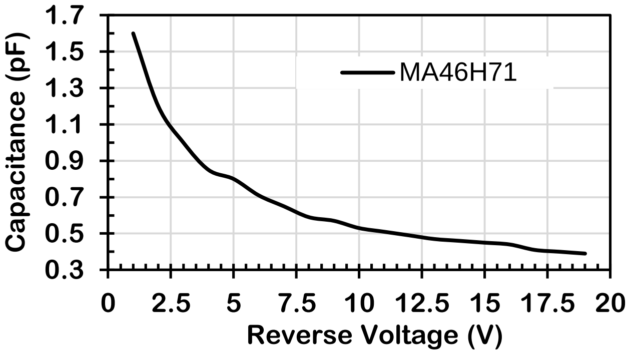

Figure 24 – Measured Capacitance x Reverse Voltage for the varactor diode MA46H71 at 2.45 GHz.

Some simulations were made in order to verify the effect of the parasitic resistance and inductance of the varactor diode's equivalent electrical model. As expected, when the series resistance was varied from 0 Ω to 3 Ω, it increased the filter's insertion loss. The variation in insertion loss changed with the increase of the capacitance and with its position across the slots, as previously explained. For the same capacitance, if $R_s$ is varied from 0 Ω to 3 Ω, the insertion loss varies 0.17 dB when the varactor diodes are located at the edge of the slots, 0.6 dB when the varactor diodes are located in the middle of the slots, and 2 dB when the varactor diodes are located at the slots junction.

## 4.4 THEORETICAL ANALYSIS & EM SIMULATIONS

The filter was simulated considering the real losses of the Rogers$^{TM}$ RO3210 substrate. The dielectric loss provided by the manufacturer is tan $\delta = 0.0021$ and the conductor loss is given by the thickness of the metal layer, 17 µm, and the copper conductivity, $5.8\text{x}10^{-7}$ S/m. The filter is very sensitive to the conductor and dielectric losses, as shown in Figure 25.

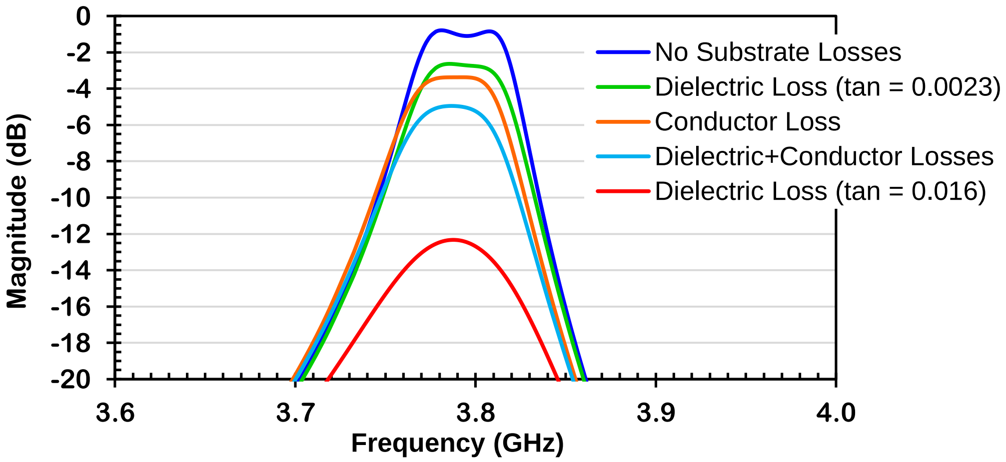

Figure 25 – Effect of the dielectric and conductor losses in the passband of the triangular patch filter.

Figure 25 shows that due to the substrate losses, the IL increased to 5 dB. In order to minimize this loss, two capacitors $C_{in}$ were placed between the feed lines and the resonator strengthening this coupling and the coupling between the source and the load. This allows a stronger coupling without positioning the feed lines extremely close to the resonator, thus facilitating the fabrication process. On the other hand, $C_{in}$ enlarges the filter bandwidth and also decreases the out-of-band rejection. The tunable dual-mode filter was then optimized with the configuration illustrated in Figure 26.

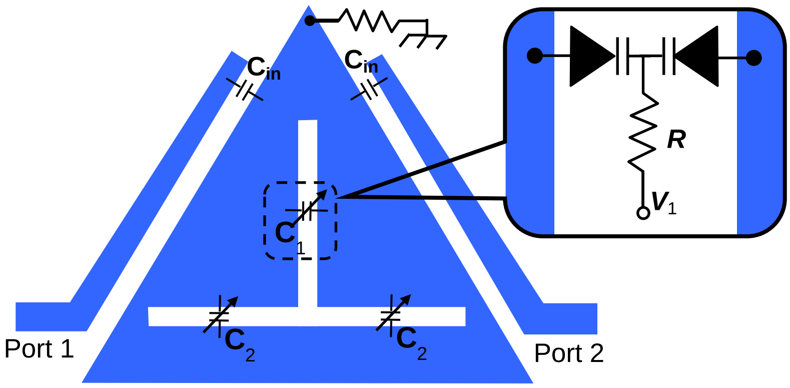

Figure 26 - Tunable dual-mode filter using a single triangular patch resonator with varactors across the slots. In detail, the assembling scheme of the varactors.

Different tuning ranges can be achieved when different values of $C_{in}$ are considered. This capacitor was also modeled and characterized as a series *RLC* circuit, where $R = 0.2\ \Omega$, $L = 0.3$ nH. $C_{in}$ was chosen to be 1.8 pF. Figure 27 shows the simulated filter response considering the *RLC* model of $C_{in}$. The center frequency was reduced to 3.7 GHz and the $\text{FBW}_{3\text{dB}}$ enlarged to 10 %.

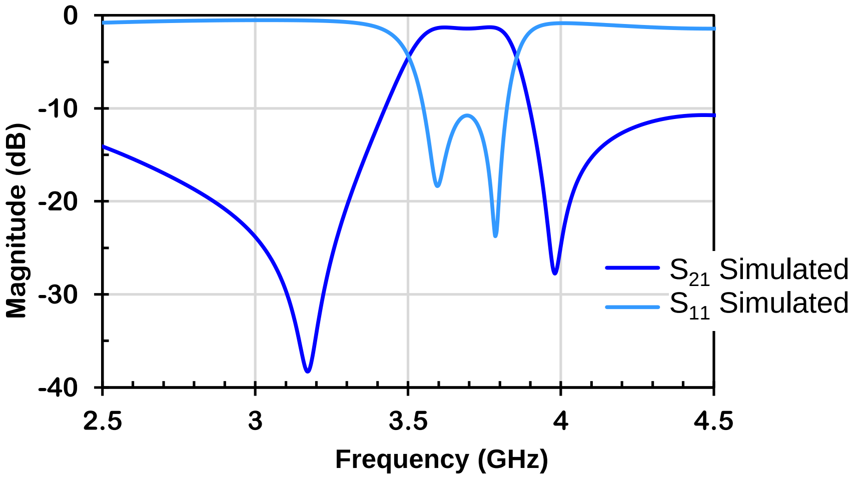

Figure 27 – Simulated filter response considering the substrate losses and the *RLC* series model of $C_{in}$, where $R = 0.2\ \Omega$, $L = 0.3$ nH, and $C_{in} = 1.8$ pF.

Figure 28 shows two theoretical curves considering $C_{in}$. One curve considers an infinite $Q$ resonator, and the other, a finite $Q = 90$ resonator, resulted from matrix (34). Note that the theoretical curves considering a real resonator with finite Q are very close to the simulated one. Hence, it can be estimated that the varactor loaded resonator's Q is near 90. This value is quite good compared to that of microstrip tunable resonators.

$$M_\Delta = \begin{bmatrix} 0 & -0.4926 & 0.6401 & -0.1097 \\ -0.4926 & -1.0777 & 0 & 0.4926 \\ 0.6401 & 0 & 1.0857 & 0.6401 \\ -0.1097 & 0.4926 & 0.6401 & 0 \end{bmatrix} \tag{34}$$

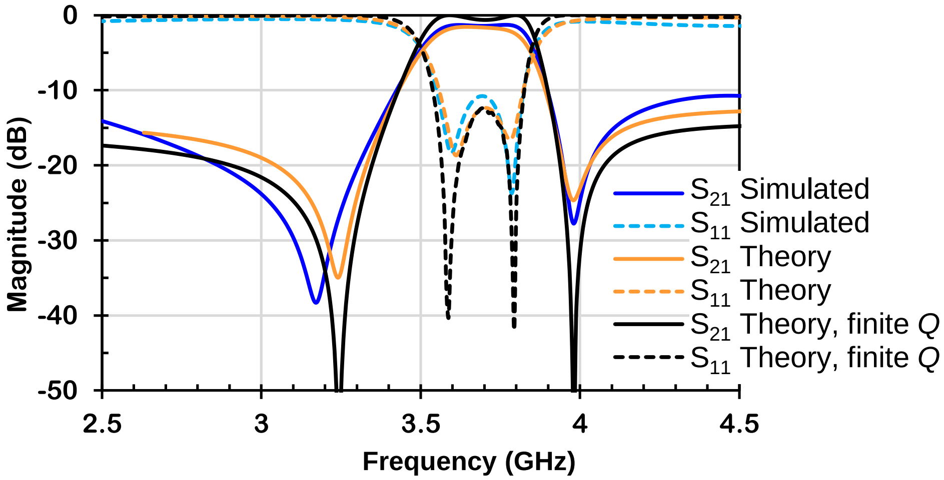

Figure 28 – Theoretical curves from (34), considering a resonator with infinite $Q$ and finite $Q = 90$.

As expected, due to $C_{in}$, the magnitude of $M_{SL}$ in the new matrix (34) highly increased when compared to the initial matrix (31). $M_{22}$ increased as well, making the $f_{even\text{-}mode}$ decrease, explaining the decrease in the center frequency. $M_{11}$ barely changed, explaining the increase in the filter bandwidth. The values of $M_{S1}$ and $M_{S2}$ increased as well.

A coupling matrix analysis was made in in order to verify the effect of the coupling coefficients in the filter frequency response. This analysis leads to three important observations:

- $M_{11}$ only changes the even-mode, and $M_{22}$ only changes the odd-mode, as expected according to (24), allowing their independent control. This is feasible because $C_1$ controls the odd-mode, represented by $M_{22}$, and $C_2$ controls the even-mode, represented by $M_{11}$. This control will be shown later in this section.
- The $FBW_{3dB}$ is a linear function of ($M_{22}$ - $M_{11}$). This observation implies that by increasing $M_{11}$ and $M_{22}$ by the same amount $u$, filters with the same $FBW_{3dB}$ and

decreasing center frequencies can be designed (and vice-versa). This can be seen in the theoretical curves obtained from matrix (35), in Figure 29.

$$M_\Delta = \begin{bmatrix} 0 & -0.4926 & 0.6401 & -0.1097 \\ -0.4926 & -1.0777 + u & 0 & 0.4926 \\ 0.6401 & 0 & 1.0857 + u & 0.6401 \\ -0.1097 & 0.4926 & 0.6401 & 0 \end{bmatrix} \tag{35}$$

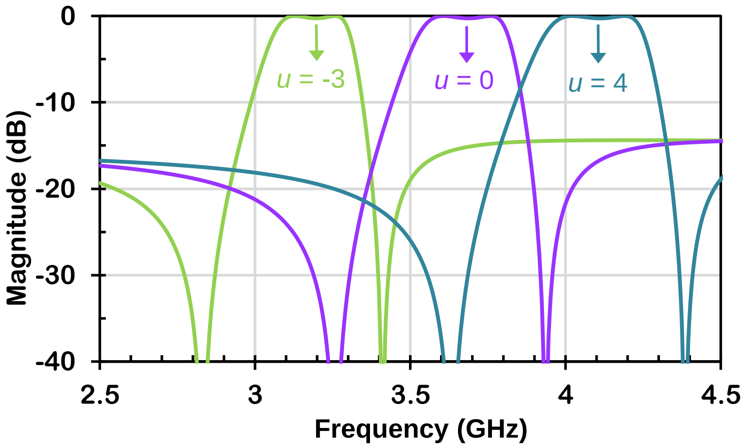

Figure 29 – Theoretical curves for filters with the same $FBW_{3dB}$ and different center frequencies for *u* = 4, *u* = 0 and *u* = -3 from matrix (35).

- The center frequency is a linear function of $(M_{22} + M_{11})/2$. This observation implies that filters with same center frequency and increasing bandwidths are achievable by decreasing $M_{11}$ and increasing $M_{22}$ by the same amount *z* (and vice-versa). This can be seen in the theoretical curves obtained from matrix (36), shown in Figure 30.

$$M_\Delta = \begin{bmatrix} 0 & -0.4926 & 0.6401 & -0.1097 \\ -0.4926 & -1.0777 - z & 0 & 0.4926 \\ 0.6401 & 0 & 1.0857 + z & 0.6401 \\ -0.1097 & 0.4926 & 0.6401 & 0 \end{bmatrix} \tag{36}$$

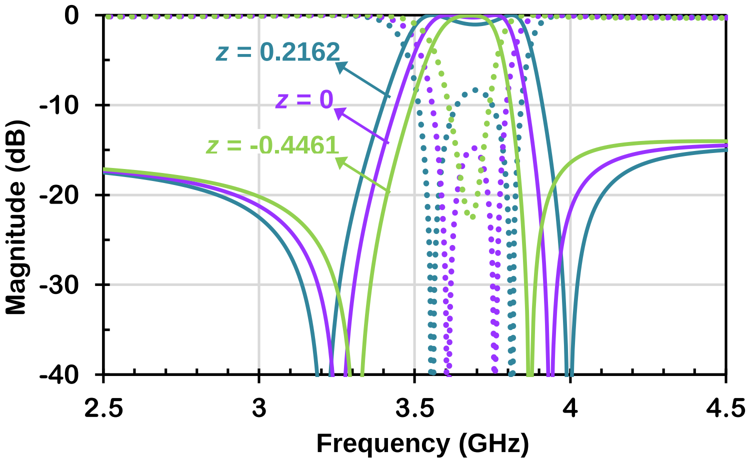

Figure 30 – Theoretical curves for filters with the same center frequency and different $FBW_{3dB}$ for *z* = 0.216, *z* = 0 and *z* = -0.446 from matrix (36).

Complete EM simulations using the capacitor model for $C_{in}$ and the varactor diodes modeled in back-to-back configuration confirmed that the tuning mechanism of changing the mode frequencies remains the same with the filter configuration using $C_{in}$. As expected, the simulated results presented in Figure 31(a) shows that $C_1$ controls the odd-mode's frequency and consequently, the transmission zero next to it, without changing the even-mode's frequency. Similarly, Figure 31(b) shows that $C_2$ controls the even-mode's frequency and its respective transmission zero without changing the odd-mode's frequency. These simulations are important to define the capacitance range needed to tune the filter, which was found to range from 0.22 pF to 1.13 pF, considering the total capacitance of the two varactor diodes connected in series.

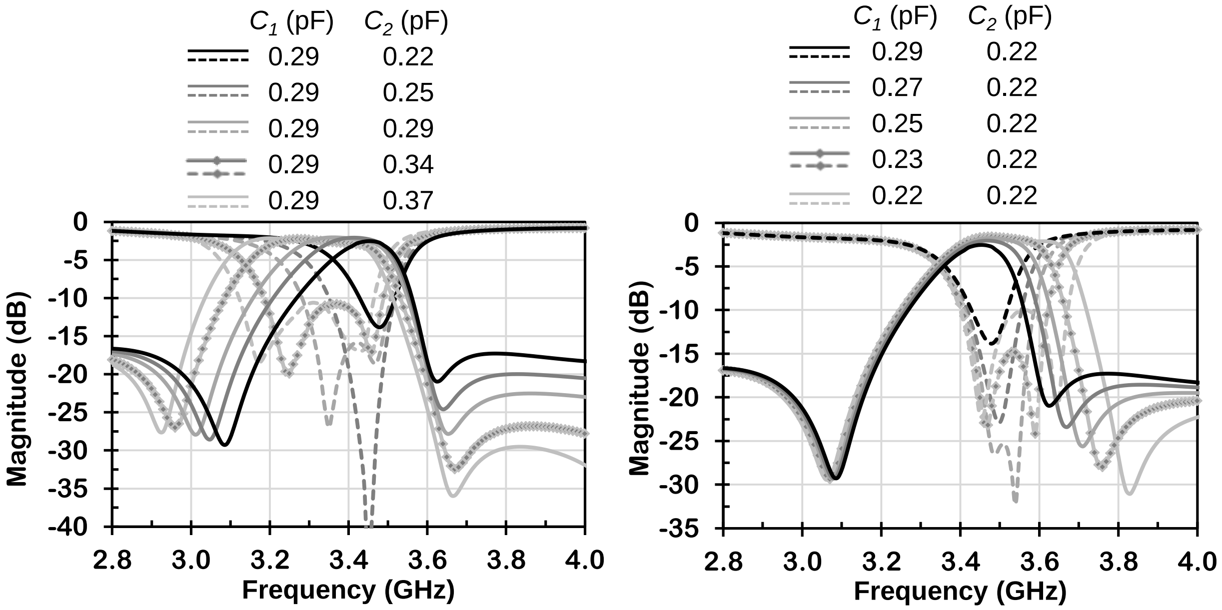

Figure 31 – Simulated results for $S_{21}$ (full line) and $S_{11}$ (dotted line) of the filter with (a) different values of $C_1$, keeping $C_2$ constant and (b) different values of $C_2$, keeping $C_1$ constant.

## 4.5 TUNABLE FILTER FABRICATION AND MEASUREMENTS

The concept was validated in a real implementation as proof-of-concept. The GaAs varactor diodes were biased with only two DC voltages, $V_1$ to control $C_1$ and $V_2$ to control both capacitances $C_2$. Resistances $R$ of 10 KΩ were used to isolate de RF signal from the DC voltage source and ground, as illustrated in Figure 26. A standard photolithographic technique was used to fabricate the filter on the *Rogers Duroid* RO3210 substrate with a thickness of 25 mils, $\varepsilon_r = 10.2$, and tan $\delta = 0.0021$. The size of the circuit shown in Figure 32 is roughly 30 mm x 20 mm, with the equilateral triangular base of 12 mm, slots' width of 0.5 mm, vertical slot's length of 5.7 mm and horizontal slot's length of 9.2 mm positioned at 1.45 mm from the base.

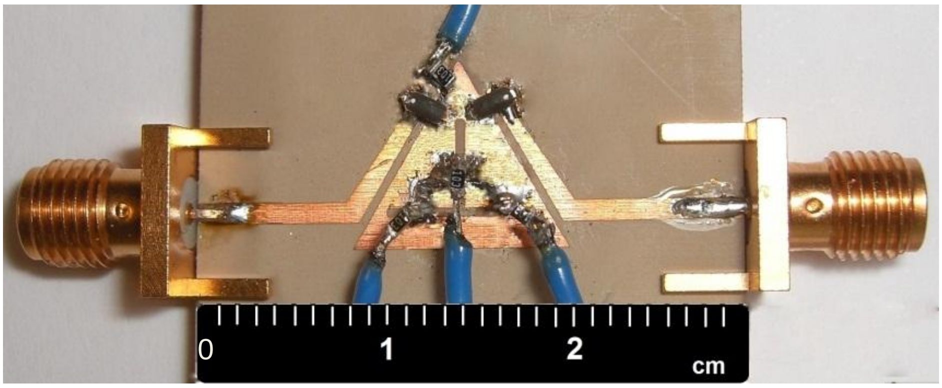

Figure 32 - Fabricated tunable dual-mode triangular patch filter.

### 4.5.1 SMALL-SIGNAL MEASUREMENTS

Measurements of the filter were carried out with the Agilent 8510C vector network analyser at small signal levels in which the varactor diodes work as linear devices. Results are shown in Figure 33 and Figure 34. They are in very good agreement with the simulations results shown in Figure 31. The capacitor $C_1$ controls the lower side of the bandpass, while $C_2$ controls the upper side. The DC bias voltage applied for the measurements of the filter frequency responses correspond to the measured $C_j\,(V)$ curve given in Figure 24. Note that the curve $C_j\,(V)$ gives the capacitance of one varactor diode, and the simulations give the total capacitance of the back-to-back configuration.

The filter presented a 20 % of center frequency tuning range from 2.9 GHz to 3.5 GHz, considering an IL lower than 3 dB and a RL better than 10 dB. The $\mathrm{FBW}_{3dB}$ could be varied from 4% to 12% within the same bounds for the losses.

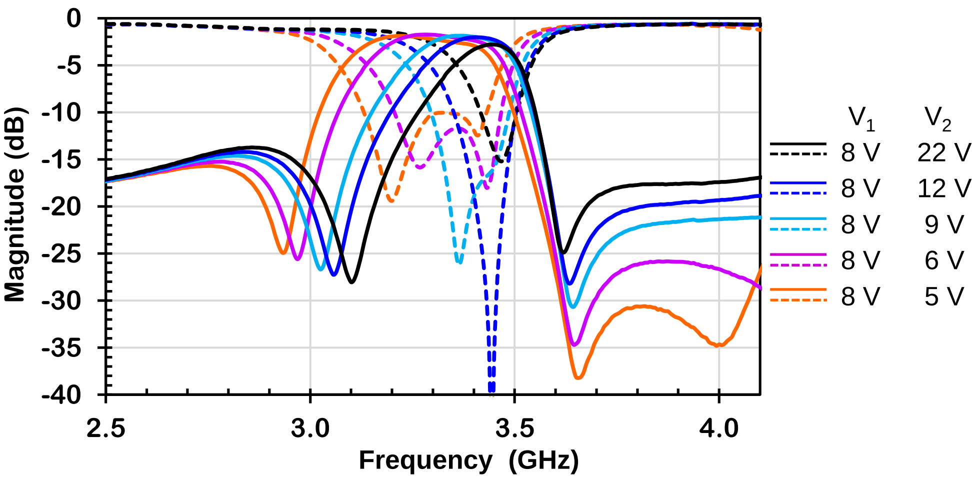

Figure 33 – Measured frequency response of the tunable triangular patch filter for different values of $V_2$, keeping $V_1$ constant.

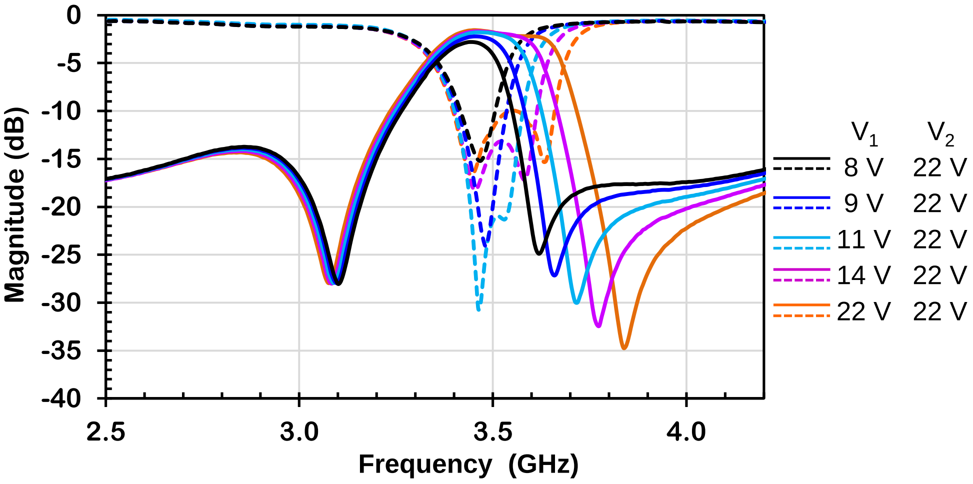

Figure 34 – Measured frequency response of the tunable triangular patch filter for different values of $V_1$, keeping $V_2$ constant.

As indicated by the theoretical analysis, it is possible to change the center frequency by keeping the 3-dB bandwidth constant as shown in the theoretical curves in Figure 35. These curves resulted from matrices (37) and (38), for both an infinite $Q$ and a finite $Q$ = 90 for the resonator.

$$M_{\Delta\, f_c=3.55\ \mathrm{GHz}}=\begin{bmatrix} 0 & -0.4926 & 0.6401 & -0.1097 \\ -0.4926 & -0.9470 & 0 & 0.4926 \\ 0.6401 & 0 & 1.0857 & 0.6401 \\ -0.1097 & 0.4926 & 0.6401 & 0 \end{bmatrix} \tag{37}$$

$$M_{\Delta\, f_c=3.05\ \mathrm{GHz}}=\begin{bmatrix} 0 & -0.4926 & 0.6401 & -0.1097 \\ -0.4926 & 2.5902 & 0 & 0.4926 \\ 0.6401 & 0 & 4.6136 & 0.6401 \\ -0.1097 & 0.4926 & 0.6401 & 0 \end{bmatrix} \tag{38}$$

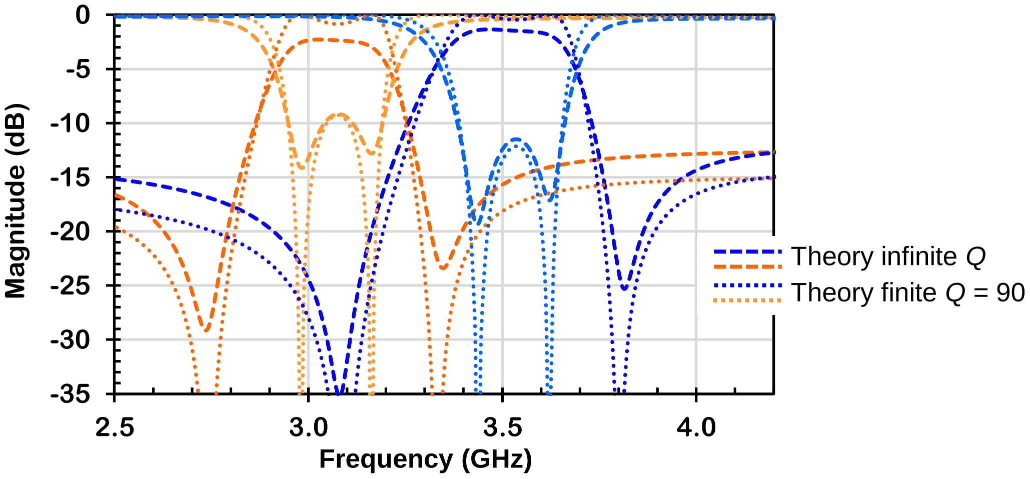

Figure 35 – Theoretical curves for the filter tuned to different center frequencies with a constant bandwidth of 318 MHz obtained from (37) and (38), considering a resonator with infinite $Q$ and finite $Q$ = 90.

Note that the term ($M_{22}$ - $M_{11}$) of each matrix is close to each other, but not the same, chosen in a way so that the bandwidth is kept constant. The center frequency of the filter was tuned to 3.55 GHz (in orange) and 3.05 GHz (in blue), both with a bandwidth of 318 MHz. The measurement results obtained by maintaining a constant $C_1/C_2$ ratio, are shown in Figure 36. They are in very good agreement with the theory. The IL is higher for the filter with lower center frequency because of the higher capacitance of the varactor diode.

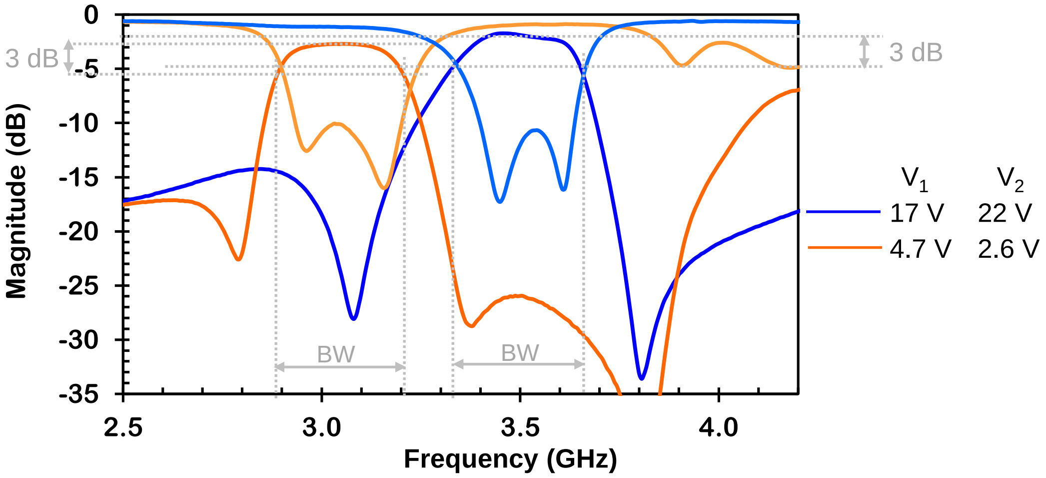

Figure 36 – Measurements of the filter tuned to different center frequencies (3.05 GHz in orange and 3.55 GHz in blue) with a constant bandwidth of 318 MHz.

The case of different bandwidths at a fixed center frequency was also possible by maintaining $\sqrt{C_1 \cdot C_2}$ constant, as analyzed in theory. Measurement results are shown in Figure 37 for a fixed center frequency of 3.36 GHz. Here again, measurement results confirm the theory.

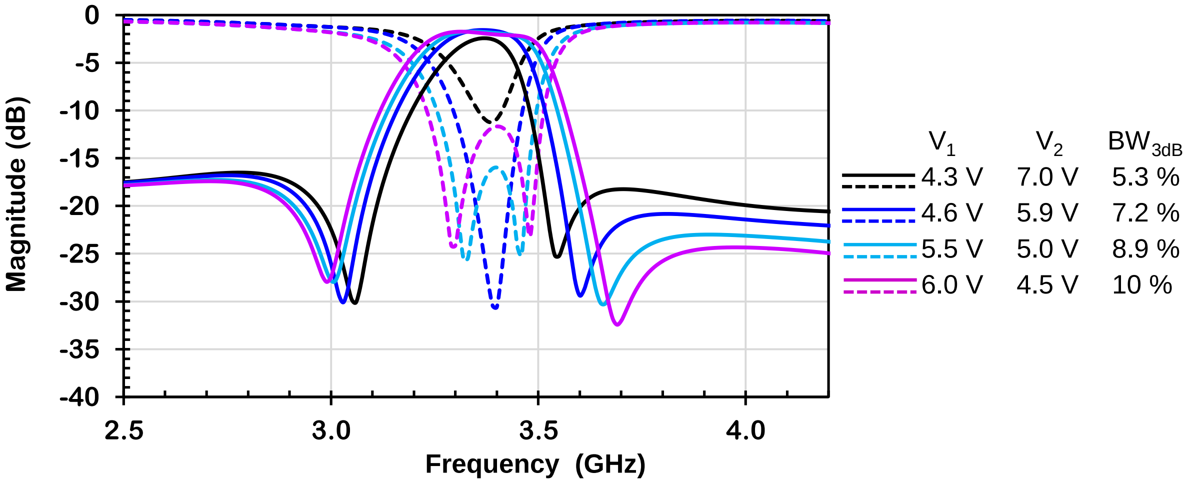

Figure 37 – Measurements for different bandwidths with a constant center frequency of 3.36 GHz.

Finally, the theory predicted that the *TZs* could be removed, and that the passband could be cancelled, as shown by the theoretical curves in Figure 19. Measurement results presented in Figure 38 confirm these theoretical results. When $f_{odd}$ becomes lower than $f_{even}$, there are no *TZs*, and when $f_{odd} = f_{even}$ there is the destructive superposition of both modes.

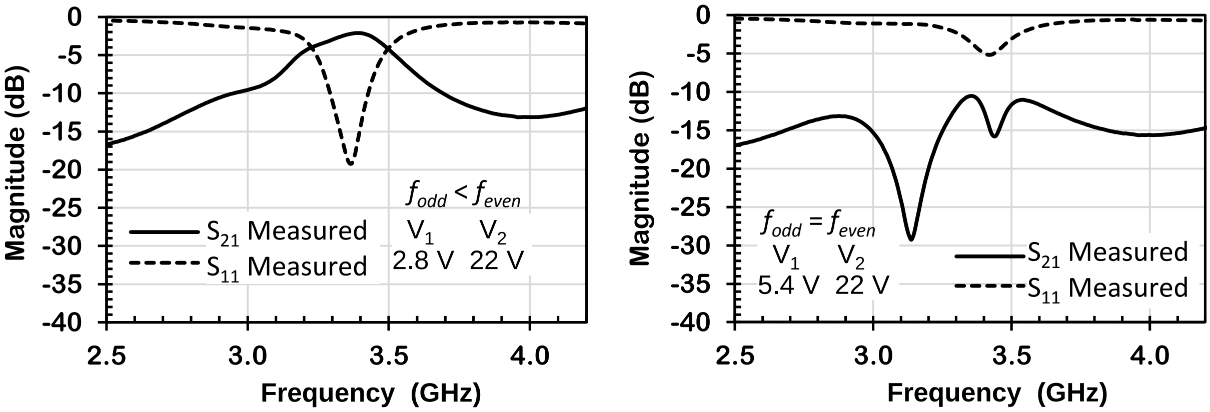

Figure 38 – Measured responses of the tunable triangular patch filter when (a) $f_{\text{odd}} < f_{\text{even}}$ and (b) $f_{\text{odd}} = f_{\text{even}}$

The small-signal measurements of the filter presented in this chapter were consistent with the theoretical approach and to the simulations, as it could be seen in the well-matched curves presented in this sub-section.

### 4.5.2 NONLINEAR MEASUREMENTS

#### *4.5.2.1 1-dB Compression Point ($P_{1dB}$)*

The 1-dB compression point ($P_{1dB}$) specified at the input of the filter is the value of the input power that results in compression of 1 dB in the output power. Measurements were performed at the filter's center frequency $f_c$ for different low biasing conditions, presented in Table 4.2.

Table 4.2 - $P_{1dB}$ of the tunable triangular filter for different biasing conditions.

| Center Frequency (GHz) | Bias Voltage (V) | $P_{1dB}$ (dBm) |
|---|---|---|
| 3.0 | 2.6 ($V_1$) and 2.8 ($V_2$) | +14.5 |
| 3.1 | 3.3 ($V_1$) and 3.2 ($V_2$) | +17.5 |
| 3.2 | 3.7 ($V_1$) and 4.9 ($V_2$) | +20.1 |
| > 3.2 | > 5 | > +21 |

As expected, by increasing the bias voltage, $P_{1dB}$ increased. For DC bias voltages higher than 5 V, the maximum input power allowed by the setup (+21.4 dBm) was reached, and the output had not yet been compressed thus, for bias voltages higher that 5 V the measurement could not be done.

The important fact is that the filter is certainly capable of handling +14 dBm of power, even at low bias voltage, which is suitable to most communication systems. Moreover, if a limited, but still wide, tuning range of 10 % between 3.2 GHz and 3.5 GHz is considered, then the $P_{1dB}$ is always greater than +21 dBm.

The effect of the compression on the entire filter's response at 3 GHz can be seen in Figure 39, for an input power below the 1-dB compression point at +7 dBm and above the $P_{1dB}$ at +16 dBm.

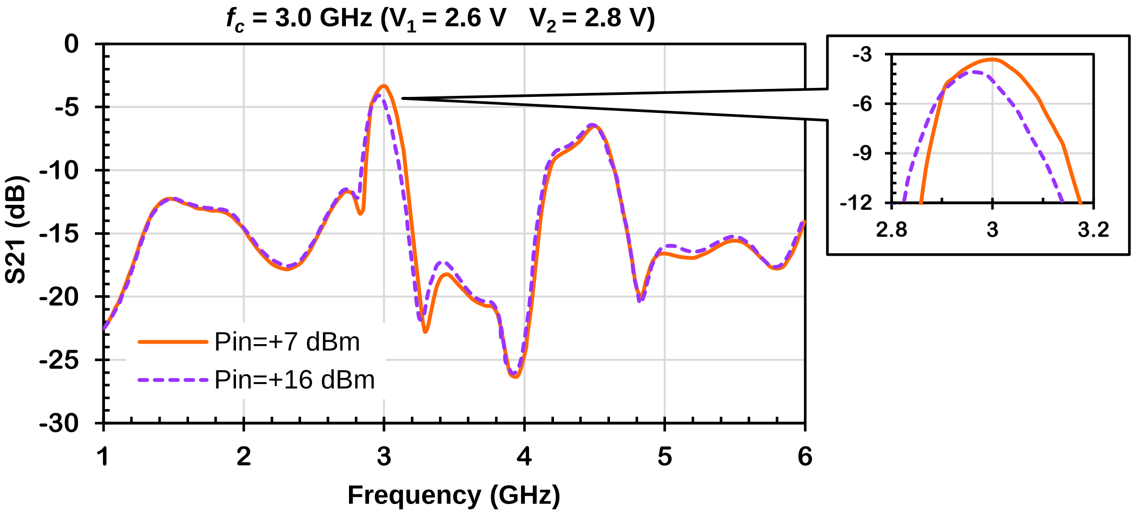

Figure 39 – Effect of the distortion on the filter response for input power below (+7 dBm) and above (+16 dBm) the $P_{1dB}$ at the lowest bias condition allowed by the filter.

The same power levels were delivered to the filter tuned to 3.1 GHz, which $P_{1dB}$ is slightly higher, shown in Figure 40. It is possible to see in this figure that the distortion effect is more accentuated for the compressed response of the filter centered at 3 GHz than for the filter centered at 3.1 GHz, which was in the beginning of compression.

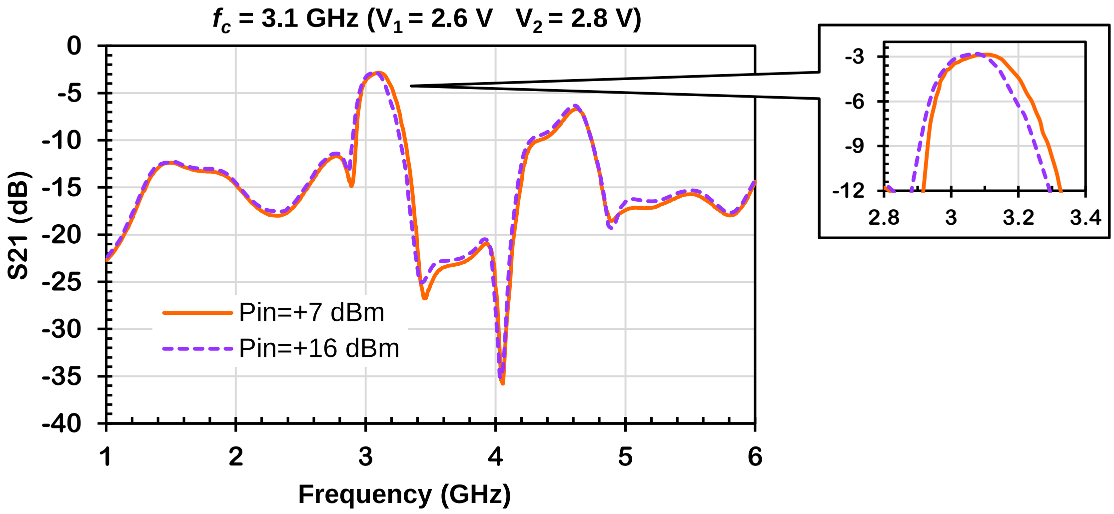

Figure 40 – Effect of the distortion on the filter response for input power below (+7 dBm) the $P_{1dB}$ and at the beginning of compression (+16 dBm) at a higher bias condition.

#### *4.5.2.2 Third-order Intercept Point*

Signal distortion was investigated using the measurement setup shown in Figure 11. Two tones separated by $\Delta f$ = 5 MHz were positioned within the filter's bandwidth. The filter was tuned to the lowest center frequency achieved by the filter, configuring the worst case for the varactor diodes distortion. The varactor diode produces higher levels of distortion for higher values of capacitance junction, or lower values of the applied reverse voltage. This situation characterizes when the filter is tuned at its minimum center frequency. The two tones were delivered to the filter with power level varying from -20 dBm to +2 dBm. The level of input tones and the intermodulation components were measured at the filter output and were used to calculate the third-order intercept point (IIP3) of the filter referred to the input port.

The minimum IIP3 was found to be equal to +29.9 dBm for the 200 MHz-bandwidth filter centered at 3 GHz as shown in Table 4.3. As expected, this value improves for higher bias voltages, and hence higher working frequency. It reaches the value of +39.9 dBm for the same bandwidth and an operating frequency $f_c$ = 3 GHz.

Table 4.3 – Measured IIP3 of the tunable filter with varactor diodes in back-to-back configuration.

| Center Frequency (GHz) | Bias Voltage (V) | IP3 (dBm) |
|---|---|---|
| 3.0 | 2.6 ($V_1$) and 2.8 ($V_2$) | +29.9 |
| 3.1 | 3.3 ($V_1$) and 3.2 ($V_2$) | +33.8 |
| 3.2 | 3.7 ($V_1$) and 4.4 ($V_2$) | +36.3 |
| 3.3 | 6.1 ($V_1$) and 5.6 ($V_2$) | +39.9 |

## 4.6 CHAPTER SUMMARY & DISCUSSION

In this chapter, a tunable dual-mode triangular patch filter with two slots was studied. The study of the couplings schemes was detailed and a very good agreement was shown between theory, simulations, and measurements. It was demonstrated that the central frequency and the bandwidth of the filter could be individually tuned by independently controlling each uncoupled degenerate fundamental mode. The topology allowed the control of each resonant mode frequency by voltage-variable capacitances realized by varactor diodes mounted across the slots of the patch resonator.

The coupling matrix analysis allowed the deduction of the conditions to correctly tune the filter and obtain the desired type of tuning. The filter presented a 20 % of center frequency tuning range from 2.9 GHz to 3.5 GHz. The $FBW_{3dB}$ could be varied from 4% to 12%. These results considered an IL lower than 3 dB and a RL better than 10 dB. Measurements clearly showed that the filter could be tuned to different operating frequencies and same bandwidth, or with different bandwidths at the same operating frequency. Moreover, it was shown that the filter could also actuate as an ON-OFF key, by changing only one bias voltage, when the modes became destructively superimposed, leading to a rejection of 15 dB at the filter operating frequency.

The tunable filter was fabricated and assembled with a simple and low cost process. The layout was designed with no critical dimensions, where the minimal dimension was 0.5 mm, facilitating the fabrication. The filter was mounted with a simple configuration of two DC bias voltages to control the varactor diode's junction capacitances. The varactor diodes were mounted in a back-to-back configuration to simplify the biasing and to reduce their distortion effects.

The unloaded quality factor $Q_u$ of the measured filter at different frequencies and bandwidths was calculated from eq. (39)[59], where $g_i$ are the elements of a low-pass prototype filter and $FW_{3dB}$ and IL are extracted from the filter measured response. This equation gives very good results if the input and output terminations of the filter are equal to each other or at least not very greatly different.

$$IL = \frac{4.343}{FBW_{3dB}} \sum_{i=1}^{N} \frac{g_i}{Q_{u_i}} \tag{39}$$

As verified by simulations, $Q_{ui}$ of each resonance and the $Q_u$ of the filter are assumed equal, leading to the equation in (40)[60].

$$Q_u = \frac{4.343}{FBW_{3dB}\, IL} \sum_{i=1}^{N} g_i \tag{40}$$

For a 2nd order filter ($N = 2$), considering a Butterworth filter, $g_1 = g_2 = 1.4142$. At the initial frequency without tuning element ($f_c$ = 3.7 GHz and $FBW_{3dB}$ = 10 %), the filter $Q_u$ calculated from (40) equals 110, which is not far from the assumed $Q_u$ of 90 considered by the coupling matrix software, presented in Figure 28. When the tunable filter is biased with the maximum DC voltage ($f_c$ = 3.55 GHz and $FBW_{3dB}$ = 11 %), the filter $Q_u$ equals 80, and with the minimum DC voltage ($f_c$ = 2.9 GHz and $FBW_{3dB}$ = 6.5 %), $Q_u$ equals 55. The $Q_u$ is expected to drop because the $Q_u$ of the varactor diode calculated by (33), decreases. However, considering all the possible combinations of center frequency and bandwidth changing the bias voltages, the $Q_u$ at can assume values as high as 130.

Simulation results showed that the filter insertion loss do not change with the variation of the series resistance $R_s$ of the varactor diode's equivalent electrical model. Therefore, the coupling capacitances $C_{in}$ between the feed lines and the resonator could also be replaced by varactors in order to tune the filter within different center frequency and bandwidth ranges, without increasing the filter insertion loss. Besides the GaAs varactor diodes used here, other variable capacitances could be used to implement this control, such as RF MEMS, which would improve even more the linearity of the filter[61].

The position and dimensions of the two slots were optimized to reduce the resonant frequencies of the fundamental modes and form a miniaturized dual-mode filter. This optimization is limited by physical constraints, as the slots reach a maximum length inside the geometry. Without tuning elements, the filter exhibited a 48 % of area reduction, considering a patch resonator without slots at the same frequency (3.7 GHz). The area reduction was calculated by (41) considering the area of the perturbed or tuned resonator $A_2$ at a frequency $f$ and the area of a resonator without perturbations or tuning elements $A_1$ at the same frequency $f$, which is calculated by the equations given in section 2.2.

$$Area\, reduction = \frac{A_2 - A_1}{A_1} \tag{41}$$

The filter could be tuned down to 3 GHz, which can also be considered as a further miniaturization, achieving an area reduction of 66 % comparing to a patch resonator without slots at 3 GHz.

The triangular patch filter could be tuned in different ways to achieve different tuning characteristics. Considering a "type A - $f_c$ tuning and constant bandwidth", the filter achieved a good center frequency tuning range of 15.4 % considering a constant absolute bandwidth. This value leaded to a reasonable figure of merit FoM of 0.71, defined in chapter 2, comparable to those in the literature, although the poor SF of 1.1. On the other hand, considering a “type B - Constant $f_c$ and bandwidth tuning”, at the same frequency, a high bandwidth tuning range of 67 % is achieved, leading to a much higher FoM of 2.2, as shown in Table 4.4. This table compares the designed tunable patch filters in this chapter and the tunable filters presented in the literature.

Table 4.4 - Comparison of tunable filters from the international literature and the tunable triangular patch filter presented in this chapter.

| Ref | Topology | Tuning type | Tuning Element | DC bias | $f_{min}$ (GHz) | IL$_{max}$ (dB) | Tuning range | Area (mm$^2$) | FoM |
|---|---|---|---|---|---|---|---|---|---|
| [23] | square Ring | D - discrete | varactor diode | 5.5 V | 2.45 | 1.6 | - | 900 | - |
| [24] | open Loop | C - discrete | VO$_2$ switch | - | 9.0 | - | 5.4 % | 84 | - |
| [25] | stub | B - discrete | PIN diode | - | 1.9 | 4.1 | 50 % | 1200 | 2.2 |
| [26] | ring & stub | C - discrete | PIN diode | - | 2.4 | 1.35 | 20 % | 900 | 1.01 |
| [27] | combline | A - continuous | varactor diode | 20 V | 0.75 | 5.0 | 18 % | 1250 | 1.86 |
| [28] | meander loop | C - continuous | varactor diode | 20 V | 1.68 | 7.6 | 41 % | 400 | 1.20 |
| [29] | folded | C - continuous | GaAs varactor diode | 20 V | 1.39 | 2.5 | 26 % | 200 | 15.6 |
| [30] | combline | C - continuous | BST varactor | 100 V | 11.7 | 10.0 | 20 % | 8.8 | 0.54 |
| [31] | folded | D - continuous | varactor diode | 20 V | 1.06 | 3.5 | 5.5 % | 1260 | 0.54 |
| [32] | CPW ring | B - continuous | BST varactor | 35 V | 1.8 | 2.5 | 10 % | 1015 | 0.56 |
| [35] | Triangular patch | B - discrete | PIN diode | 10 V | 10 | 3.3 | 60 % | 180 | 0.42 |
| [36] | Square patch | A - discrete | PIN diode | 10 V | 8.9 | 3.7 | 10 % | 225 | 0.06 |
| This filter | Triangular Patch | A - continuous | GaAs varactor diode | 22 V | 3.0 | 3 | 15 % | 375 | 0.71 |
| This filter | Triangular patch | B - continuous | GaAs varactor diode | 7 V | 3.36 | 3 | 67 % | 375 | 2.2 |

# 5 TUNABLE CIRCULAR PATCH FILTER WITH CENTER FREQUENCY AND BANDWIDTH CONTROL

This chapter describes the design, fabrication, and measurement of a tunable filter using a triple-mode circular patch resonator, initially centered at 2.45 GHz and with 27 % of $FBW_{3dB}$. The use of three modes allows the design of a bandpass patch filter with higher level of miniaturization, a wider bandwidth, and low insertion loss. This topology was first designed in my master's dissertation as a fixed filter. Here, it was modified to tune continuously its center frequency, bandwidth, and selectivity by varactor diodes. A detailed study of the continuously tunable circular patch filter, its modeling, and the corresponding analysis in terms of coupling scheme and coupling matrix are presented in this chapter.

## 5.1 INITIAL FILTER ANALYSIS

The basic triple-mode patch filter was designed with a circular resonator modified by four radial slots. The three different resonant modes that form this filter are the two fundamental degenerate modes ($TM^z_{1,1,0}$ - A and $TM^z_{1,1,0}$ - B) and the second mode ($TM^z_{2,1,0}$). The electric field patterns corresponding to these three modes are represented in Figure 41.

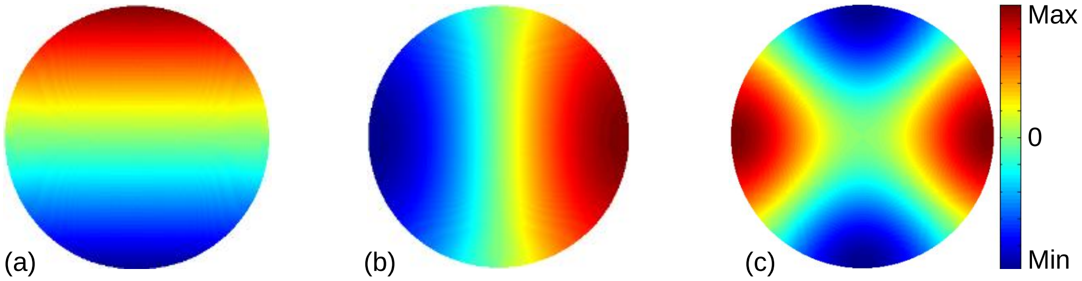

Figure 41 – Electric field patterns of the (a) fundamental degenerate mode $TM^z_{1,1,0}$ - A, (b) fundamental degenerate mode $TM^z_{1,1,0}$ – B, and (c) second mode $TM^z_{2,1,0}$ of a circular patch filter.

In a circular patch resonator, the patterns for the electric fields of the degenerate fundamental modes are orthogonal as seen in Figure 41. Their corresponding current distributions obtained from the EM simulations with the patch weakly coupled to the feed lines are shown in Figure 42. Considering the feed lines positioned as in this figure, both degenerate fundamental modes and the second mode are excited. This is because a resonant mode is excited when the excitation port is positioned where the electric field magnitude of this mode is not null. Therefore, considering the electric filed patterns in Figure 41, it is clear that each port excites only one of the degenerate fundamental modes and both ports excite the second mode. In the case where there is no perturbation in the patch resonator, the EM simulations confirmed that $TM^z_{1,1,0}$ - A is excited only by the output, resulting in the vertical current distribution presented in Figure 42(a). Analogously, the EM simulations showed that $TM^z_{1,1,0}$ - B is excited only by the input, resulting in the horizontal current distribution presented in Figure 42(b). $TM^z_{2,1,0}$, however, is excited by both ports, resulting in the current distribution presented in Figure 42(c).

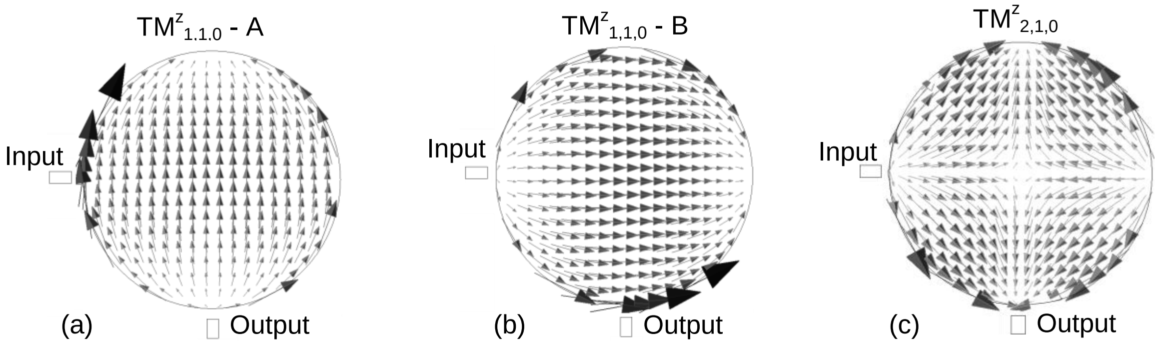

Figure 42 – Current distributions of the degenerate modes (a) $TM^z_{1,1,0}$ - A and (b) $TM^z_{1,1,0}$ - B, and (c) second mode $TM^z_{2,1,0}$ in an unperturbed circular patch resonator weakly coupled to the feed lines.

Nevertheless, the current distributions may rotate depending on the perturbation inserted in the resonator. This rotation happens when using any type of radial slot positioned at 45º away from the horizontal axis, as the ones illustrated in Figure 43.

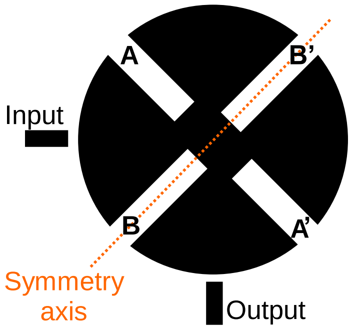

Figure 43 - Layout of a circular patch resonator with four radial slots positioned at ±45º from the horizontal axis.

As an example, a small perturbation was added to the patch at 45º away from the horizontal axis. This small perturbation in the form of a very thin rectangular slot rotates the fields in the same way as the four slots in Figure 43, hardly changing the current distributions of the modes. The rotated current distributions of the degenerate fundamental modes are shown in Figure 44. Note that the second mode does not rotate with the perturbation. Now that degenerate modes are rotated, the feed lines are no longer positioned at their null electric field, indicating that the degenerate modes are coupled to both ports. Considering the symmetry axis of the structure relative to the input and output ports shown in Figure 43, one can specify which modes have even or odd symmetry with respect to the symmetry axis of this structure.

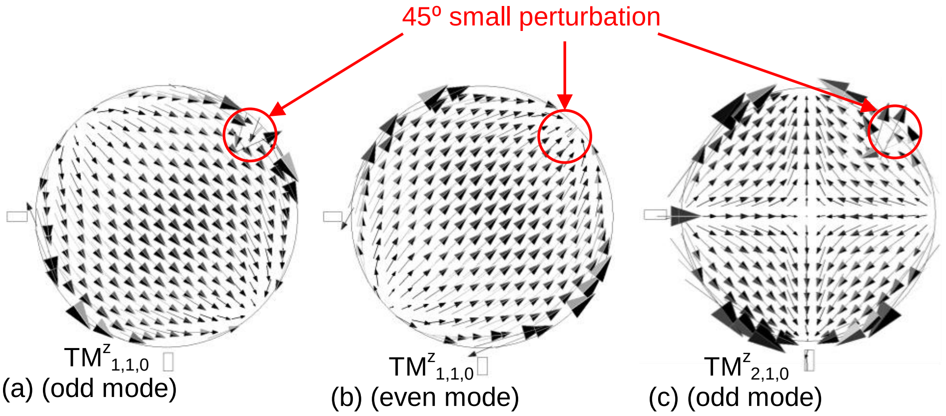

$TM^z_{1,1,0}$ (a) (odd mode)

$TM^z_{1,1,0}$ (b) (even mode)

$TM^z_{2,1,0}$ (c) (odd mode)

Figure 44 - Current distributions of the $TM^z_{1,1,0}$ degenerate (a) even and (b) odd modes and (c) $TM^z_{2,1,0}$ mode in a slightly perturbed circular patch resonator weakly coupled to the feed lines.

Then, it is simple to observe that the slots A-A’ will mainly perturb the fundamental even-mode, whereas the slots B-B’ will mainly perturb the fundamental odd-mode. The $TM^z_{2,1,0}$ mode, however, will be perturbed by all the four slots, and thus, its frequency will decrease more than the fundamental modes’ frequencies, leading to very close resonant frequencies when the correct set of slots’ lengths is chosen.

Figure 45 shows the results of the EM simulations performed in Momentum using a circular patch resonator with 8.1 mm of radius weakly coupled to the orthogonal feed lines as shown in Figure 43. The substrate considered is the Rogers 3010 ($\varepsilon_r$ = 10.2 and thickness = 25 mils) without losses. From this figure, the initial dimensions of the slots were chosen in order to split the degenerate modes, lower their resonant frequency, and lower the second mode frequency so that the three resonant frequencies are around 2.4 GHz. The feed lines were directly connected to the resonator to achieve the necessary couplings and form the passband. Their width is 0.58 mm in order to match the 50 Ω characteristic impedance microstrip line.

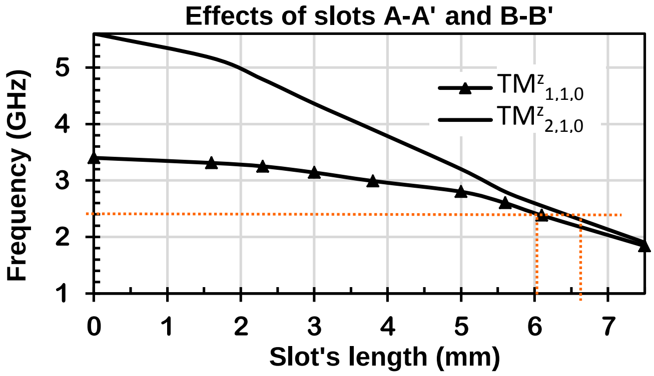

Figure 45 – Simulated resonant frequencies of the degenerate fundamental modes and the second resonant mode as a function of the length of slots A-A’ and B-B’ in a circular patch resonator with radius of 8.1 mm.

The initial layout of the circular patch filter with dimensions is given in Figure 46.

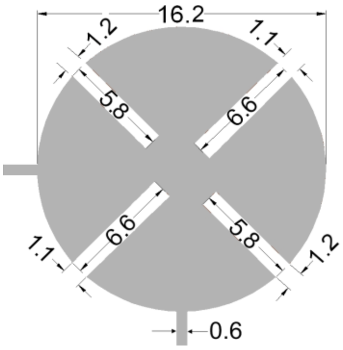

Figure 46 - Layout of the initial circular patch filter (dimensions in mm).

The simulated frequency response of the triple-mode patch filter is shown in Figure 47.

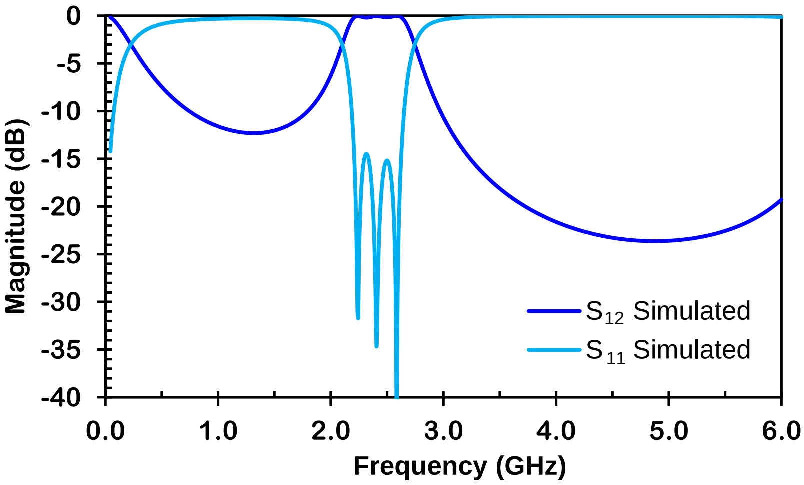

Figure 47 – Simulated frequency response of the unloaded triple-mode circular patch filter.

The filter exhibits a central frequency of 2.43 GHz and $FBW_{3dB}$ of 28 %. The EM simulations showed that the pole at the lowest frequency in Figure 47 corresponds to the $TM^z_{1,1,0}$ odd mode, the pole in the middle corresponds to the $TM^z_{1,1,0}$ even mode, and the pole at higher frequency corresponds to $TM^z_{2,1,0}$.

The conventional coupling scheme of a circular patch topology using only the degenerate modes is shown in Figure 48(a). Note that one degenerate mode is only coupled to the source and the other, to the load, as shown in the beginning of this chapter for a circular patch resonator without perturbation. Due to the symmetric geometry of the filter, the behavior of the degenerate fundamental modes in this structure can be interpreted with a 45º rotation that remodels the couplings between the nodes, as shown in Figure 48(b). In the second case, each mode is connected to both ports. These schemes are mathematically equivalent, however, as explained, the current distribution indicates that the second scheme better represents the model of this filter.

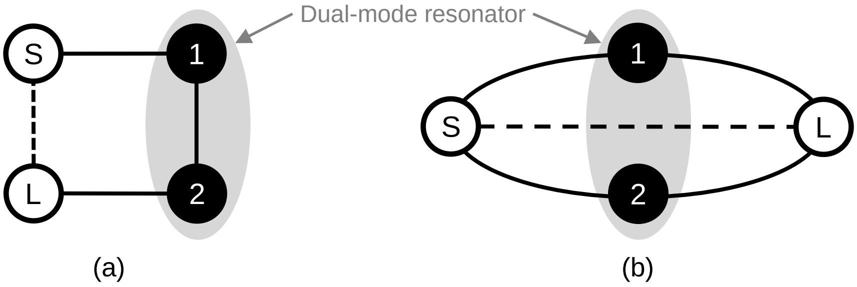

Figure 48 – (a) Conventional coupling scheme of the degenerate modes in a circular patch resonator. (b) Interpretation of the coupling scheme of the degenerate modes for the patch filter under analysis.

Figure 49 presents the complete coupling scheme for the triple-mode circular patch filter discussed in this chapter.

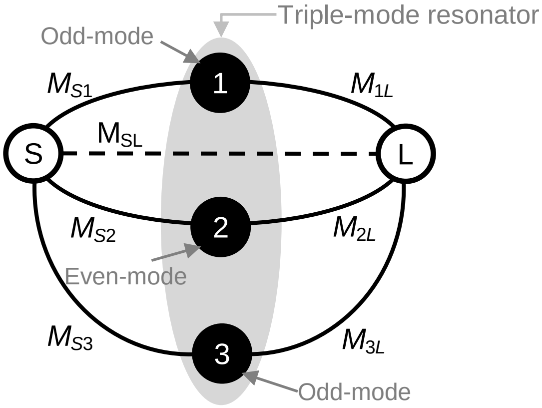

Figure 49 – Complete coupling scheme of the circular patch filter with one single (triple-mode) resonator supporting the two fundamental degenerate modes and the second mode.

In Figure 49, “1”, “2”, and “3” were chosen to represent the fundamental split odd mode, the fundamental split even mode, and the second mode, respectively. Thus, $M_{S1} = -M_{1L}$, $M_{S2} = M_{2L}$ and $M_{S3} = -M_{3L}$. The coupling matrix related to the coupling scheme presented in this figure is given by $M_O$ in (42), where the index “O” was used to refer to the circular resonator.

$$M_O = \begin{bmatrix} 0 & M_{S1} & M_{S2} & M_{S3} & M_{SL} \\ M_{1S} & M_{11} & 0 & 0 & M_{1L} \\ M_{2S} & 0 & M_{22} & 0 & M_{2L} \\ M_{3S} & 0 & 0 & M_{33} & M_{3L} \\ M_{LS} & M_{L1} & M_{L2} & M_{L3} & 0 \end{bmatrix} \tag{42}$$

Initially, there is no evidence concerning the coupling between source and load as they are directly connected to the resonator and there are no *TZ* in the frequency response of the filter. Because of that, the initial choice of $M_{SL}$ will be zero. Using such configuration, the coupling matrix can be analytically calculated[54] considering the equations given in section 3.1 and an in-band return loss of 15 dB, resulting in matrix (43).

$$M_O = \begin{bmatrix} 0 & 0.4890 & 0.4509 & 0.4500 & 0 \\ 0.4890 & 0.9020 & 0 & 0 & -0.4890 \\ 0.4509 & 0 & 0.0220 & 0 & 0.4509 \\ 0.4500 & 0 & 0 & -0.7488 & -0.4500 \\ 0 & -0.4890 & 0.4509 & -0.4500 & 0 \end{bmatrix} \tag{43}$$

It is important to notice that the position of each mode and its related couplings is merely a choice when building the matrix. For example, in matrix (43), “1” and “2” were chosen to represent the fundamental odd (in blue) and even (in red) modes, respectively. However, “1” and “2” could be chosen to represent the opposite, the even and odd modes. In the latter case, the matrix should be changed as shown in matrix (44) in order to keep the same couplings and to produce exactly the same response.

$$M_O = \begin{bmatrix} 0 & 0.4509 & 0.4890 & 0.4500 & 0 \\ 0.4509 & 0.0220 & 0 & 0 & 0.4509 \\ 0.4890 & 0 & 0.9020 & 0 & -0.4890 \\ 0.4500 & 0 & 0 & -0.7488 & -0.4500 \\ 0 & 0.4509 & -0.4890 & -0.4500 & 0 \end{bmatrix} \tag{44}$$

To facilitate the comprehension, the first choice was used in this analysis, where $M_{11}$, $M_{22}$ and $M_{33}$ represent each mode from the lower to the highest resonant frequency, indicated by the three poles in the frequency response of the filter, shown in Figure 47.

Figure 50 compares the theoretical frequency response produced by matrices (43) (or (44) considering the filter centered at 2.43 GHz and bandwidth of 650 MHz, and the EM simulation result of the filter without tuning elements. It can be seen at the inset of this figure that the insertion loss is almost zero, presenting a small ripple of 0.2 dB within the passband, indicating that the radiation loss is negligible due to the nature of the feed lines coupling to the resonator. All curves are in very good agreement except for the lower rejection band. The theoretical curve has better rejection than the simulated one because the input and output are directly connected to the resonator. When the feed lines are connected in such manner, the filter acts as a low-pass filter from DC to low frequencies, which is not accounted for in the matrix elements. The matrix models only the filter passband and a narrow frequency range around it. The matrix can model neither the filter response at very low frequencies nor the filter spurious harmonics.

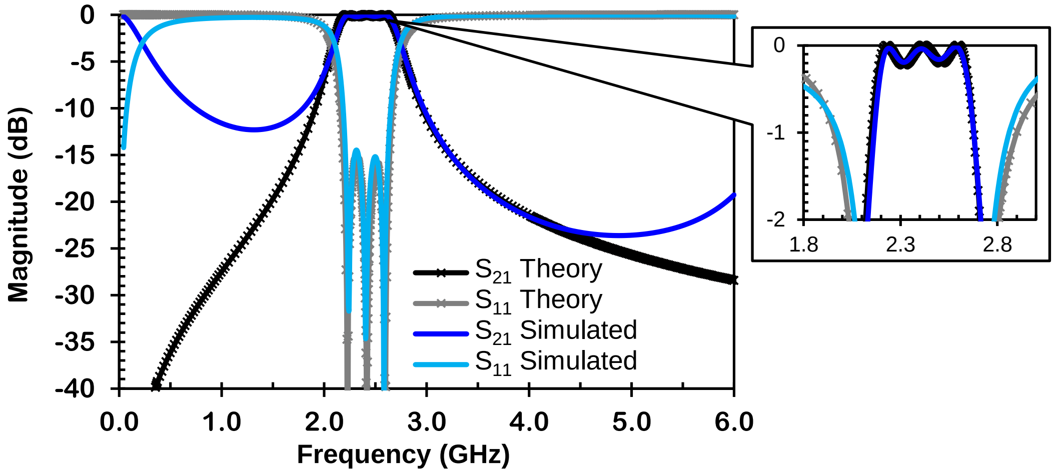

Figure 50 – Lossless simulated and theoretical (from matrix $M_O$ in (43)) responses of the unloaded triple-mode circular patch filter. An inset of the passband is shown on the upper right corner.

## 5.2 TUNING ANALYSIS

In order to verify how a patch filter behaves when capacitively loaded, the proposed patch filter was analyzed with capacitances across its slots at three possible positions: outside edge, middle or inside edge of the slots, as seen in Figure 51.

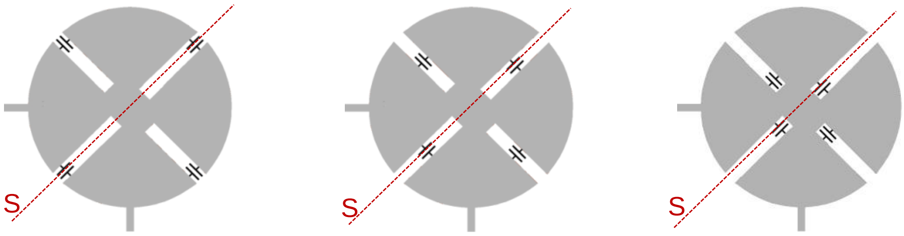

(a) (b) (c)

Figure 51 – Patch filter capacitively loaded at the (a) outside edge of the slots, (b) middle of the slots, and (c) inside edge of the slots.

The simulation results showed that each capacitance affects more than one resonant mode. This was expected as the simulations showed that one slot affects more than one mode, which is further detailed below.

Once more, the change in modal frequencies is affected not only by the capacitances, but also by their position across the slots. Table 5.1 shows the influence of the capacitances position on the tuning range, considering the filter frequency response with RL better than 10 dB within the passband. The IL remained practically constant and null along the whole tuning range. The four capacitances were kept equal in order to simplify the study. At a specific capacitance ($C_S$), the modes superimpose destructively at the resonant frequency ($f_S$) highly increasing the insertion loss. By further increasing the capacitances, the insertion loss decreases to its initial value up to a capacitance ($C_{max}$) in which the RL becomes worse than 10 dB due to the mismatch of the resonator impedance. In this table, the maximum tuning range is considered up to the capacitance $C_{max}$, which depends on its position at the slots. $C_{max}$ is equal to 5.5 pF when the capacitances are positioned at the inside edge of the slots, 4.4 pF in the middle, and 2.67 pF when positioned at the outside edge of the slots.

Table 5.1 – Simulated center frequency and capacitance ranges for different positions of capacitances along the four slots of the circular patch filter.

| Capacitance position | Capacitance range (pF) | Frequency range (GHz) | $C_S$ (pF) | $f_S$ (GHz) | Tuning range (%) |
|---|---|---|---|---|---|
| Inside edge of slots | 0 – 5.50 | 2.43 – 1.88 | 8.7 | 1.82 | 25 (max. range) |
| Middle of slots | 0 – 4.40 | 2.43 – 1.49 | 2.00 | 1.82 | 48 (max. range) |
| | 0 – 1.75 | 2.43 – 1.88 | - | - | 25 |
| Outside edge of slots | 0 – 2.67 | 2.43 – 1.54 | 1.33 | 1.82 | 45 (max. range) |
| | 0 – 1.16 | 2.43 – 1.88 | - | - | 25 |

The simulated results in this table show that a maximum center frequency tuning range of 48 % is obtained when the capacitances are positioned in the middle of the slots, which is the broadest tuning range of the three positions. In order to compare the influence of the capacitances in the center frequency response, the capacitances were also assessed within the same tuning range of 25 % from 2.43 GHz to 1.88 GHz at the three positions. Table 5.1 shows that for this range, a broader capacitance variation is needed when the capacitances are placed at the inside edge of the slots. This is understandable because at this position, the capacitances are short-circuited by the end of the slot, and hence their effect is weak. Therefore, for a given loading capacitance, the sensitivity of the resonance frequency increases when the capacitances are moved towards the border of the resonator.

Although the frequency range obtained with the capacitances positioned at the border of the resonator is close to the one with the capacitances in the middle of slots, its capacitance range is much narrower, making the filter excessively sensitive and, as explained before, more sensible to the parasitic resistance when considering a real tuning element. Therefore, the filter was designed with capacitors in the middle of the slots, providing the largest tuning range with a well-matched response within a reasonable range of capacitance.

For a proof-of-concept of this initial study, a circular filter was fabricated using fixed capacitors across the four slots, with the layout presented in Figure 52. The capacitors used were SMD 0505 capacitors, modeled as a series *RLC* with $R = 0.5\ \Omega$, and $L = 0.3$ nH. The filter was fabricated with traditional photolithographic process, which brought some inaccuracies in the whole filter dimensions, slightly changing its frequency response. Thus, after the fabrication, the filter was measured and its real dimensions were used in the filter simulations.

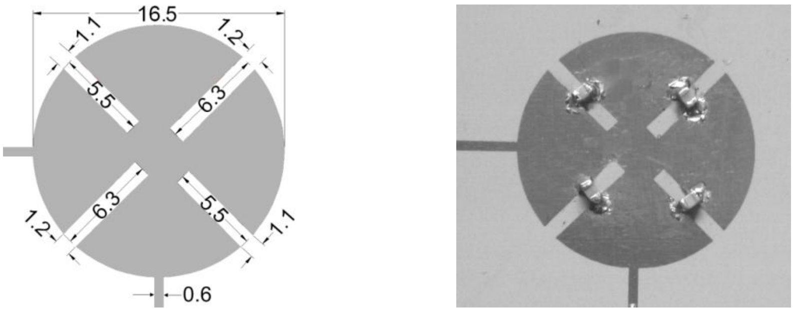

Figure 52 – Picture of the prototype circular patch filter with capacitors across the four slots.

The simulated and measured frequency responses of the unloaded filter, shown in Figure 53, are in very good agreement. The triple-mode patch filter is centered at 2.37 GHz, with $\mathrm{FBW}_{3\mathrm{dB}}$ of 28 %, insertion loss lower than 0.7 dB and return loss better than 12 dB.

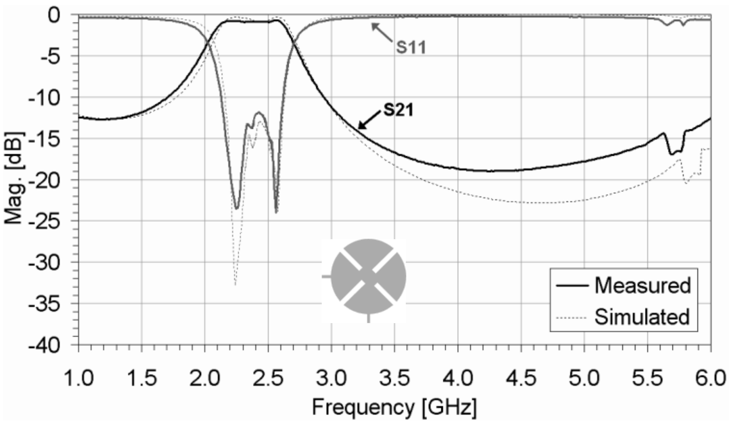

Figure 53 – Simulated and measured frequency responses of the unloaded triple-mode circular patch filter.

The patch filter could be tuned by manually changing the capacitors. The capacitance variation from zero to 1.8 pF resulted in 25 % of center frequency tuning range, varying from 2.37 GHz to 1.8 GHz. At the same time, the filter's passband decreased from 28 % to 8 % for the same range of capacitances. These results are summarized in Table 5.2 and presented in Figure 54.

Table 5.2 – Experimental results of the patch filter loaded with four equal capacitors mounted in the middle of the slots with different capacitances.

| Value of each capacitor (pF) | Center frequency (GHz) | $FBW_{3dB}$ (%) |
|---|---|---|
| No capacitors | 2.37 | 27.6 |
| 0.3 | 2.30 | 24.3 |
| 0.5 | 2.21 | 23.0 |
| 0.7 | 2.15 | 22.7 |
| 1.2 | 1.91 | 17.2 |
| 1.5 | 1.92 | 9.8 |
| 1.8 | 1.84 | 8.1 |

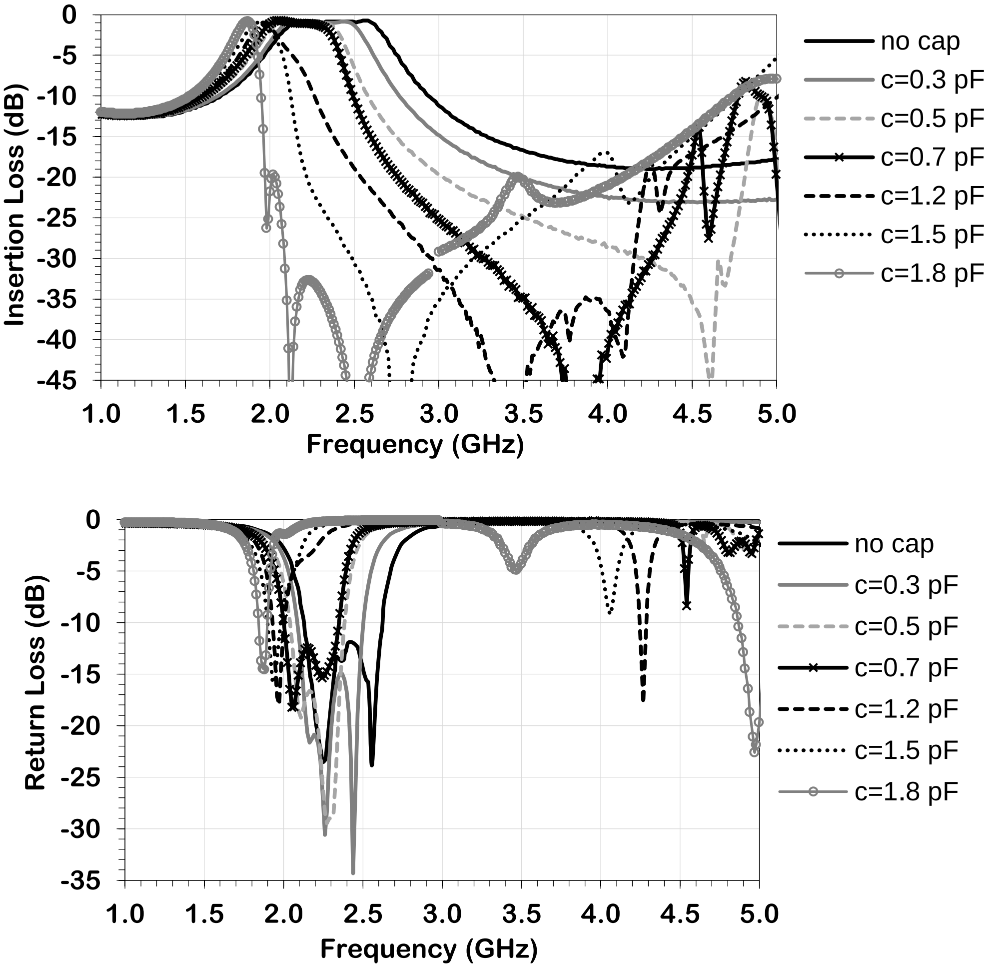

Figure 54 - Measured frequency responses of the circular patch filter loaded at the middle of the four slots with different capacitor values.

When the capacitances are greater than 1.8 pF, the passband characteristic is deformed and thus, the results were disregarded. The results presented consider an insertion loss better than 1.3 dB and a return loss better than 13 dB.

In order to obtain an electronically tuning, the filter was then analyzed considering the same varactor diode used in the design of the triangular patch resonator, the diode MA46H71, from M/A-COM. The varactor model has been detailed in section 4.3. The same back-to-back configuration was used because it facilitates the diodes biasing, halves the total capacitance, improves the nonlinearity performance, and better adjusts the capacitance of the tuning filter.

In the circular patch filter, as the input and output are directly connected to the resonator, the biasing configuration was inverted, and the patch resonator was connected to a positive DC bias source, instead of connected to the ground, as shown in Figure 55.

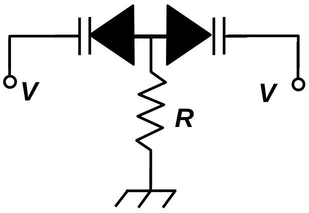

Figure 55 - Back-to-back configuration of the varactor diodes to halve the capacitance and improve nonlinearity.

## 5.3 THEORETICAL ANALYSIS & COMPLETE SIMULATIONS

As the couplings in this circular patch filter are not as simple as in the previous triangular filter, some investigations were carried out to further understand their behavior. The initial studies with fixed capacitors indicated that the simulations give a very good prediction of the filter response. The circular patch filter was then analyzed with a more complete model, using the varactor diode model positioned in the middle of the slots in the back-to-back configuration presented in Figure 55.

Four strips parallel to each slot were added to the layout, providing an easy access for the varactor diodes to the ground through the edges of the substrate board, and keeping the layout simple without any vias, resulting in the filter layout shown in Figure 56. Simulations of the filter with these strips showed that they have almost no effect on the filter response, slightly altering the scattering parameters in frequencies higher than 3 GHz.

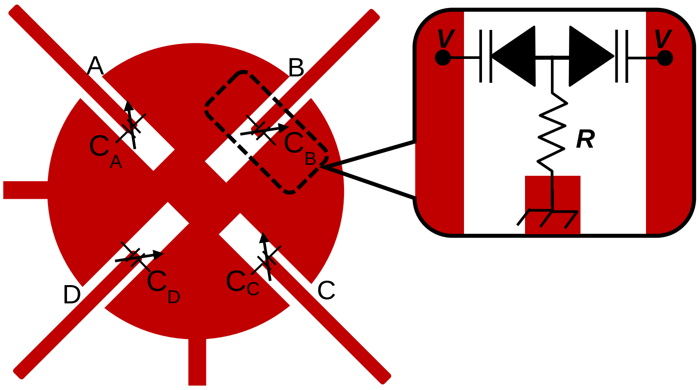

Figure 56 – Topology of the triple-mode circular bandpass patch filter with tuning elements in the middle of each slot.

The coupling matrix was recalculated with an in-band return loss of 10 dB within the passband, resulting in the coupling matrix presented by (45).

$$M_O = \begin{bmatrix} 0 & 0.4890 & 0.4609 & 0.4500 & 0 \\ 0.4890 & 0.8772 & 0 & 0 & -0.4890 \\ 0.4609 & 0 & 0.0520 & 0 & 0.4609 \\ 0.4500 & 0 & 0 & -0.8280 & -0.4500 \\ 0 & -0.4890 & 0.4609 & -0.4500 & 0 \end{bmatrix} \quad (45)$$

The substrate considered in the simulations and used to realize the filter is the Rogers 3010 ($\varepsilon_r = 10.2$, $\tan\,\delta = 0.0023$ and thickness = 25 mils). The simulations were carried out considering the substrate dielectric and conductor losses, which individual effects in the insertion loss of the filter passband is shown in Figure 57. The conductor and dielectric losses are in the same order of magnitude. For comparison, the filter was also simulated with a substrate with five times higher dielectric loss ($\tan\,\delta = 0.016$), like the low-cost FR4 substrate. This leads to an increase in the insertion loss from 0.4 dB to 2 dB.

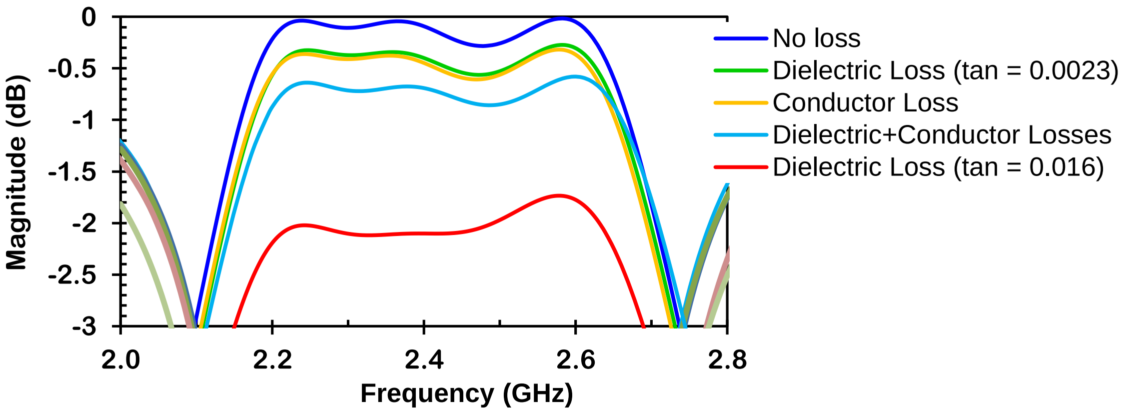

Figure 57 – Individual and total effects of the dielectric and conductor losses in the passband of the circular patch filter.

Figure 58 shows the theoretical frequency response considering the filter centered at 2.41 GHz and with 650 MHz of bandwidth, the simulated, and the measured frequency responses of the unloaded circular patch filter. The theoretical curves consider an ideal resonator with infinite unloaded quality factor $Q_u$, seen in the inset in Figure 58, which agreed well with the lossless simulations.

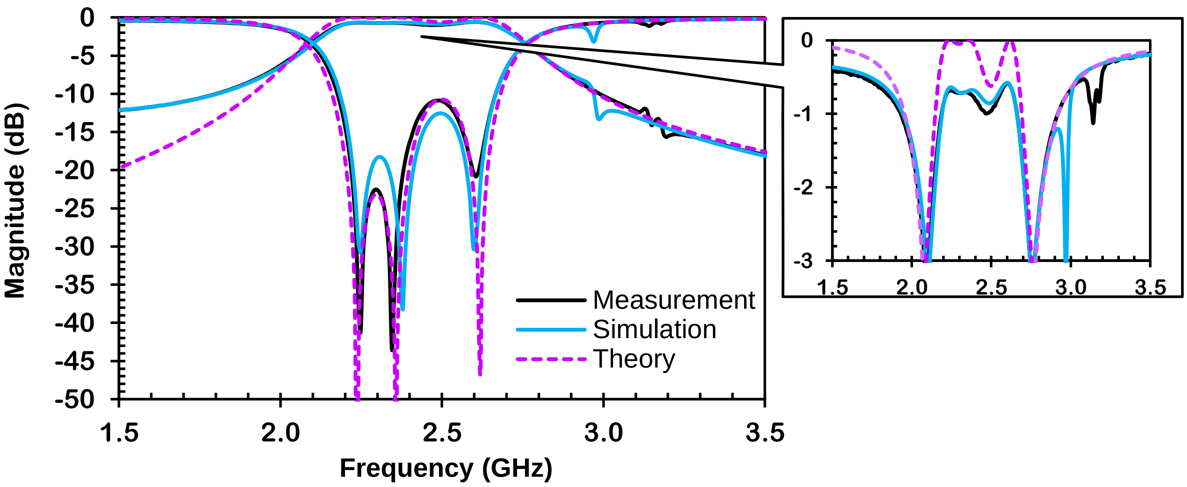

Figure 58 – Measured, simulated and theoretical (from matrix $M_O$ in (45)) frequency responses of the unloaded triple-mode circular patch filter. An inset of the passband is shown on the upper right corner.

This new study is concerned with how the capacitance connected to each slot affects the coupling coefficients of the matrix (45). A comparison between the simulated and theoretical frequency responses was carried out by varying the capacitance of only one slot at a time.

In order to clarify the study, the capacitance in each slot will be referenced as $C_A$, $C_B$, $C_C$ and $C_D$, respectively, as illustrated in Figure 56 and the frequency of the resonant modes $TM^z_{1,1,0}$ odd, $TM^z_{1,1,0}$ even, and $TM^z_{2,1,0}$ will be referred as $f_1$, $f_2$, and $f_3$, respectively. All theoretical curves ware plotted with the center frequency and bandwidth of the unloaded circular patch filter.

### 5.3.1 EFFECT OF $C_A$ AND $C_C$ ON THE COUPLING COEFFICIENTS

$C_A$ and $C_C$ have the same effect on the response of the filter, due to its symmetry. If these two capacitances are changed separately, the filter cannot be matched and the return loss is not acceptable. Therefore, the analysis was carried out with the influence of equal capacitances $C_A$ and $C_C$ varying together.

From the increase of these two capacitances, one can perceive two different effects in the mode frequencies: the decrease of $f_2$ approximating it to $f_1$, and the decrease of $f_3$. Each one of these effects can be individually modeled by increasing $M_{22}$ and $M_{33}$. It is interesting to note that both coefficients vary by the same amount of $w$, added to the coupling matrix in (46).

$$M_{\mathrm{AC}} = \begin{bmatrix} 0 & 0.4890 & 0.4609 & 0.4500 & 0 \\ 0.4890 & 0.8772 & 0 & 0 & -0.4890 \\ 0.4609 & 0 & 0.0520 + w & 0 & 0.4609 \\ 0.4500 & 0 & 0 & -0.8280 + w & -0.4500 \\ 0 & -0.4890 & 0.4609 & -0.4500 & 0 \end{bmatrix} \tag{46}$$

Figure 59 shows the simulated frequency responses when varying both $C_A$ and $C_C$ with the same values and the corresponding theoretical frequency responses for different values of $w$, modeled by matrix $M_{AC}$ in (46). Note that a very small capacitance already brings $f_2$ so close to $f_1$ that it is not possible to distinguish each other anymore.

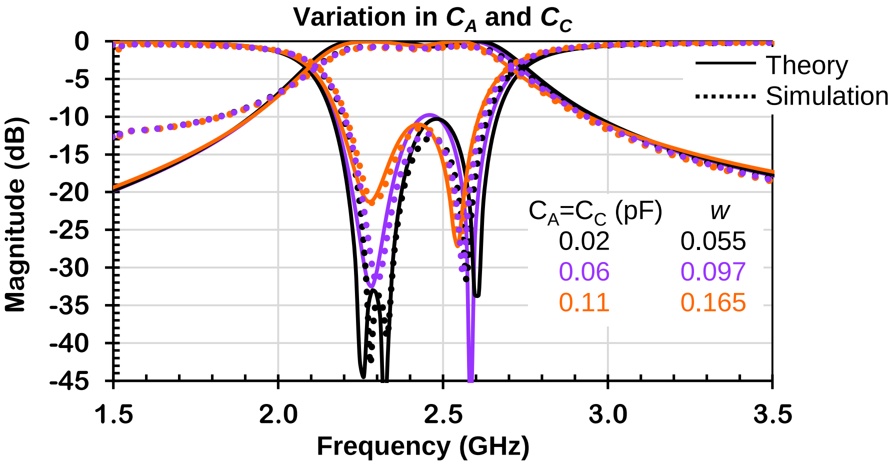

Figure 59 – Simulated frequency responses of the triple-mode circular patch filter capacitively loaded at slot A and slot C (dotted-line), and respective theoretical curves according to matrix $M_{AC}$ in (46) (full-line).

In conclusion, the main effect of increasing $C_A$ and $C_C$ is to increase both $M_{22}$ and $M_{33}$, which is equivalent to reduce both $f_2$ and $f_3$.

### 5.3.2 EFFECT OF $C_B$ ON THE COUPLING COEFFICIENTS

A different behavior can be seen when changing $C_B$. The increase of this capacitance lowers both $f_1$ and $f_3$ at the same time, while slightly increasing $f_2$. Simulations showed that $C_B$ has a stronger effect on $f_3$ than on $f_1$, reducing $f_3$ more than $f_1$. Thus, to accurately model this influence, $M_{33}$ should increase more than $M_{11}$. From the analysis of the coupling matrix, it was possible to determine the correct amount: $M_{33}$ should be increased 2.4 times more than $M_{11}$, resulting in the coupling matrix $M_B$ in (47). Using these values, the theoretical responses were correctly fitted to the simulations shown in Figure 60. Even though there is a small change in $f_2$, $M_{22}$ was not changed because the change in $M_{11}$ and $M_{33}$ resulted in the expected variation of $f_2$.

$$M_B = \begin{bmatrix} 0 & 0.4890 & 0.4609 & 0.4500 & 0 \\ 0.4890 & 0.8772 + z & 0 & 0 & -0.4890 \\ 0.4609 & 0 & 0.0520 & 0 & 0.4609 \\ 0.4500 & 0 & 0 & -0.8280 + 2.4 * z & -0.4500 \\ 0 & -0.4890 & 0.4609 & -0.4500 & 0 \end{bmatrix} \tag{47}$$

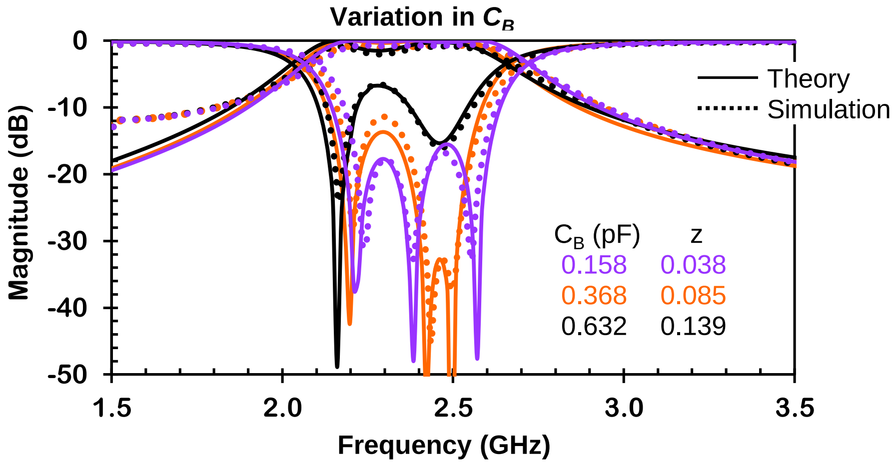

Figure 60 – Simulated frequency responses of the triple-mode circular patch filter capacitively loaded only at slot B (dotted-line), and respective theoretical curves according to matrix $M_B$ in (47) (full-line).

In conclusion, the main effect of increasing $C_B$ is to increase both $M_{11}$ and $M_{33}$, which is equivalent to reduce both $f_1$ and $f_3$, and slightly increase $f_2$.

### 5.3.3 EFFECT OF $C_D$ ON THE COUPLING COEFFICIENTS

$C_D$ affects the filter response in yet another way. The analysis of the effect of $C_D$ is much more complex because this capacitance affects several couplings at the same time.

Initially, by increasing $C_D$, $f_1$ and $f_3$ decrease, and $f_2$ remains unchanged. As seen in the previous section concerning the effect of $C_B$, when $M_{11}$ and $M_{33}$ increase, $f_1$ and $f_3$, are reduced, but $f_2$ is slightly increased, even if $M_{22}$ remains unchanged. Therefore, in the case of $C_D$, if $M_{11}$ and $M_{33}$ increase, $M_{22}$ has to slightly increase, in order to lower $f_2$ and keep it at the same frequency. This situation can be simply modeled by increasing the three susceptances by the same amount.

The EM simulations, however, also exhibited a transmission zero (TZ) at the upper side of the passband. Increasing $C_D$ lowers the frequency at which the TZ is located. This was expected because $C_D$ makes a quasi-direct path between input and output ports. A transmission zero can be modeled by any coupling that provides a shorter path for the signal from the input to the output. A TZ cannot be modeled by susceptances, because they only model changes in the resonant modes frequency. Thus, it is necessary to find which coupling or couplings provide the expected TZ. An inspection of the coupling coefficients $M_{S1}$ (= -$M_{1L}$), $M_{S2}$ (= $M_{2L}$), $M_{S3}$ (= -$M_{3L}$), and $M_{SL}$ (= $M_{LS}$) showed the following:

- (1) by increasing the coupling between the feed lines and the fundamental even mode $M_{S2}$, two TZ are brought to finite frequencies, one at each side of the filter bandpass. If these couplings are decreased, the overall rejection of the out-of-band frequency response worsens;
- (2) by decreasing the coupling between the feed lines and the fundamental odd mode $M_{S1}$, one TZ is brought to finite frequencies below the filter bandpass. If these couplings are increased, the overall rejection of the out-of-band frequency response worsens;
- (3) by decreasing the coupling between the feed lines and the $TM^z_{2,1,0}$ mode $M_{S3}$, one TZ is brought to finite frequencies at the upper side of the filter bandpass. If these couplings are increased, the overall rejection of the out-of-band frequency response worsens;
- (4) by increasing the coupling between source and load $M_{SL}$, a TZ is brought to finite frequencies below the filter bandpass. If this coupling is decreased, the TZ is moved to the upper side of the filter bandpass.

Thus, the TZ at the upper side of the filter bandpass can be modeled by decreasing either $M_{S3}$ (= -$M_{3L}$), or $M_{SL}$ (= $M_{LS}$), or both. Nevertheless, those couplings also change the frequency of all resonant modes. Therefore, the initial scenario where all susceptances could be increased of the same amount to model an increase in $C_D$ is no longer valid. The susceptances will increase, but with different amounts *a*, *b* and *c*. The corresponding matrix for modeling the effect of $C_D$ is finally given by $M_D$, in (48).

$$M_D = \begin{bmatrix} 0 & 0.4890 & 0.4609 & 0.4500 * u & g \\ 0.4890 & 0.8772 + a & 0 & 0 & -0.4890 \\ 0.4609 & 0 & 0.0520 + \mathrm{b} & 0 & 0.4609 \\ 0.4500 * u & 0 & 0 & -0.8280 + c & -0.4500 * u \\ g & -0.4890 & 0.4609 & -0.4500 * u & 0 \end{bmatrix} \tag{48}$$

The frequency response resulted from this matrix for different values of *a*, *b*, *c*, *g* and *u* is presented in Figure 61 with the respective simulated curves obtained by varying $C_D$. As can be seen in Figure 61, the filter response was very well modeled by changing the three susceptances and both couplings $M_{S3}$ (= $-M_{3L}$), and $M_{SL}$ (= $M_{LS}$).

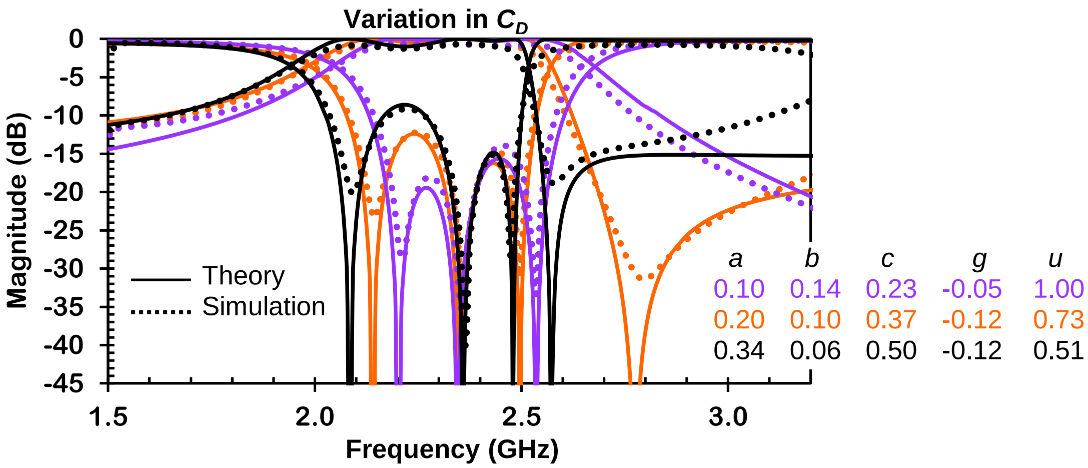

Figure 61 – Simulated frequency responses of the triple-mode circular patch filter capacitively loaded only at slot D (dotted-line), and respective theoretical curves according to matrix $M_D$ in (48) (full-line).

In conclusion, the effect of increasing $C_D$ is to increase the three susceptances and the magnitude of $M_{S3}$ and $M_{SL}$, which is equivalent to reduce both $f_1$ and $f_3$, while keeping $f_2$ unchanged, and to bring a transmission zero closer to the upper side of the passband, improving the selectivity at the upper side of the filter passband.

### 5.3.4 COMBINED EFFECT OF THE 4 CAPACITANCES ON THE COUPLING COEFFICIENTS

The study carried out in the above sub-sections has shown that when using the capacitances across the four slots, the coupling coefficients varied in different ways, allowing this patch filter to be reconfigured by varactor diodes in terms of its center frequency, bandwidth, and rejection. The rejection is changed by bringing a transmission zero close to the upper side of the passband. Particularly for the susceptances, they all increased with the increase of each individual capacitance, and thus, the result of increasing all capacitances together is obviously a simultaneous decrease in the frequency of the three resonant modes. Furthermore, important observations can be done from the theoretical analysis of different filter responses, analogously to the triangular filter:

- $M_{11}$ changes the fundamental odd-mode, $M_{22}$ changes the fundamental even-mode, and $M_{33}$ changes the second odd-mode. If individual capacitances can also change individually these modes, a tunable filter with independent tuning of frequency and bandwidth is feasible.

- The center frequency is a linear function of the average susceptance ($(M_{11} + M_{22} + M_{33})/3$), as seen in Figure 62(a). Figure 62 was plotted with the coupling coefficient values adjusted to the simulations (and later to measurements with the varactor diodes) of equal capacitances at the four slots of the filter.
- $FBW_{3dB}$ is a linear function of ($M_{33}$ - $M_{11}$), corresponding to the difference between the maximum and minimum susceptances, as seen in Figure 62(b).

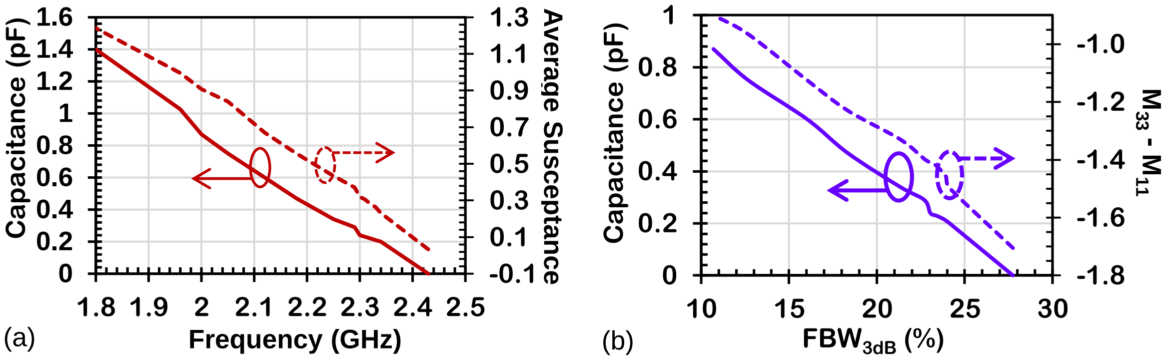

Figure 62 – Simulated and theoretical curves of the filter loaded with equal capacitances at the four slots (a) center frequency x capacitance (full-line), center frequency x average susceptance (dashed-line); (b) bandwidth x capacitance (full-line), bandwidth x ($M_{33}$-$M_{11}$) (dashed-line).

The analysis of the capacitance effect in each slot showed that individual changes in each mode frequency are not possible, so the degree of freedom of this filter is reduced compared to the tunable triangular patch filter.

On the other hand, simulations with equal capacitances at the four slots showed that both frequency and bandwidth decrease at the same time when increasing all the capacitances. In terms of the coupling matrix analysis, the coupling coefficients that generate the theoretical curves corresponding to those simulations are presented in Figure 63.

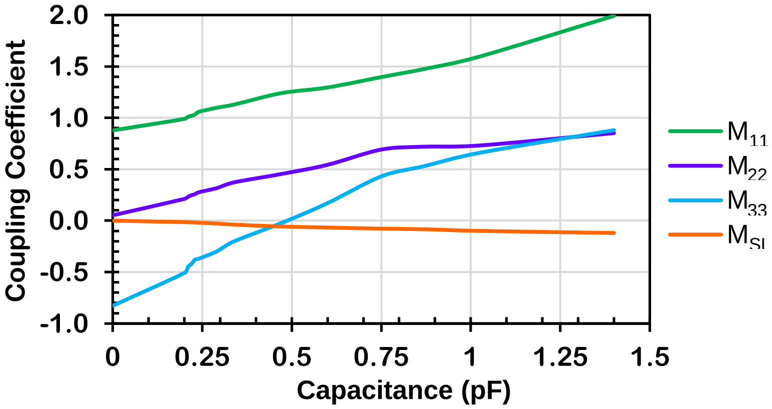

Figure 63 – Couplings coefficients ($M_{11}$, $M_{22}$, $M_{33}$ and $M_{SL}$) variation corresponding to the simulated results of the filter loaded with equal capacitances at the four slots.

The coupling matrix analysis showed that the susceptance $M_{33}$ increases more than $M_{11}$ or $M_{22}$ because of the combined effect of the capacitances. This means that $f_3$ decreases faster than the two other frequencies, explaining the reduction of the filter center frequency and bandwidth.

Furthermore, the simulations with equal capacitances at the four slots, in Figure 64 showed that a transmission zero is brought to the upper side of the passband. The capacitance given in the legend of these curves is the total capacitance of the back-to-back varactor diodes configuration connected to each slot.

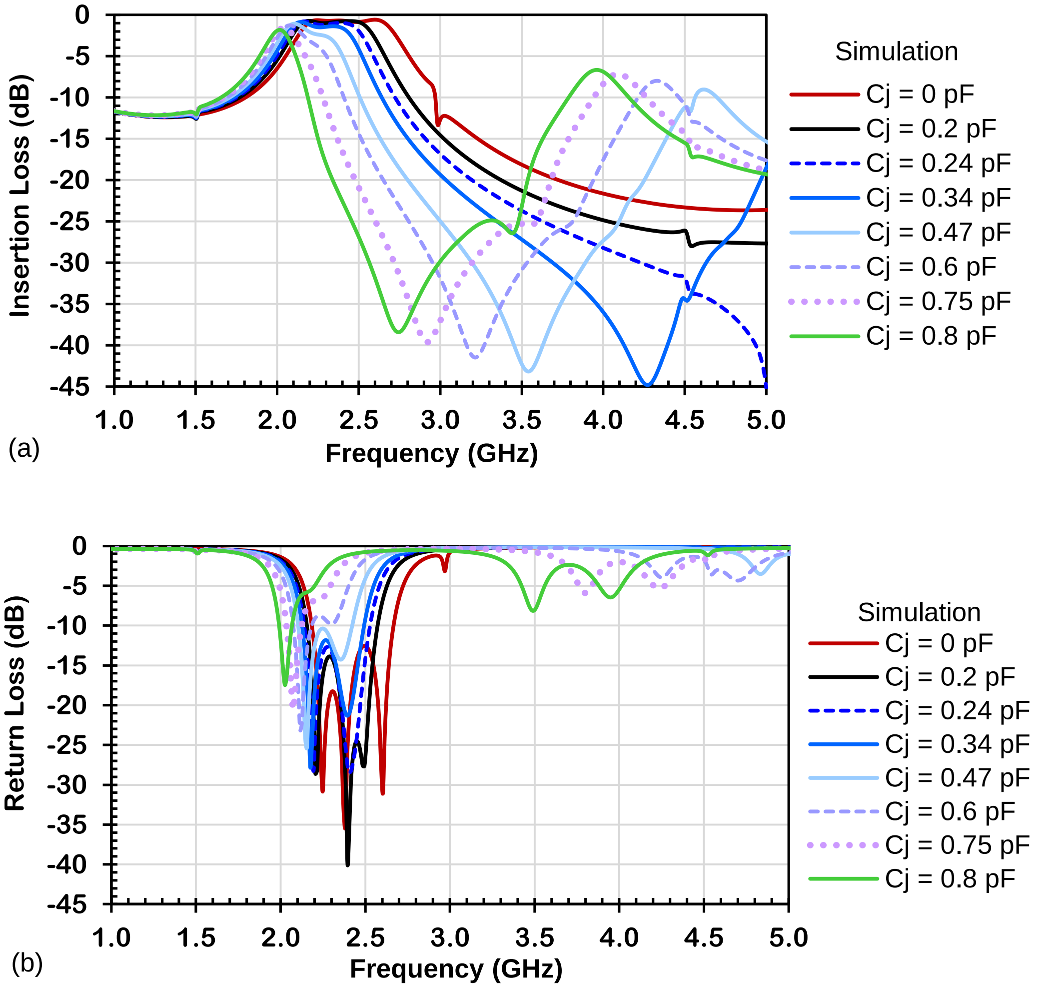

Figure 64 – Simulated frequency responses of the circular patch filter loaded equally at the four slots as illustrated in Figure 56. The value is the total capacitance of the two varactor diodes in each slot. (a) Insertion loss. (b) Return loss.

As explained in section 5.3.3 concerning the effect of $C_D$, the transmission zero was accounted for by the negative coupling between the input and output $M_{SL} = M_{LS}$, and a small modification of the coupling between source/load and resonant mode “3” $M_{S3} = -M_{3L}$. The theoretical curves are presented in Figure 65, which considered the combined effects of the coupling coefficients corresponding to the effect of the four equal capacitances used in the simulations. The values of the coupling coefficients of these curves can be extracted from Figure 63.

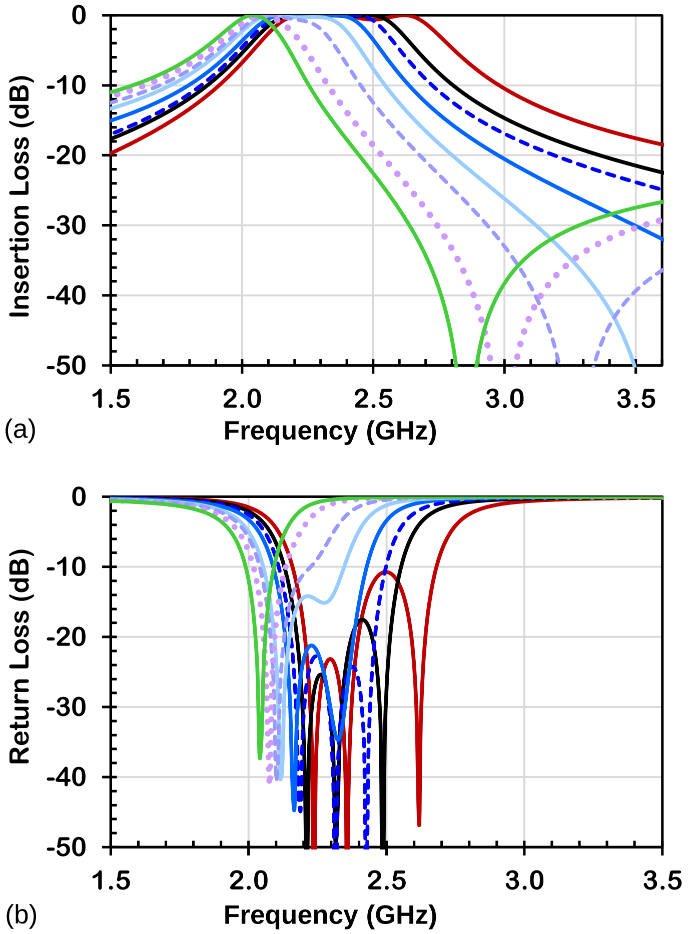

Figure 65 – Theoretical response of the circular patch filter loaded equally at the four slots, with the coefficients presented in Figure 63. (a) Insertion loss. (b) Return loss.

## 5.4 TUNABLE FILTER FABRICATION AND MEASUREMENTS

### 5.4.1 SMALL-SIGNAL MEASUREMENT

The fabricated and assembled tunable bandpass circular patch filter is presented in Figure 66. The configuration of the patch filter with the input and output directly connected to the resonator provides a DC path, which deteriorates the filter rejection at very low frequencies, as explained above. In order to enhance the filter rejection at low frequencies, a decoupling capacitor was used at the input and output feed lines. The filter was assembled with all the varactor diodes biased by a single DC voltage connected to the patch through a 47 KΩ resistor to block the RF signal.

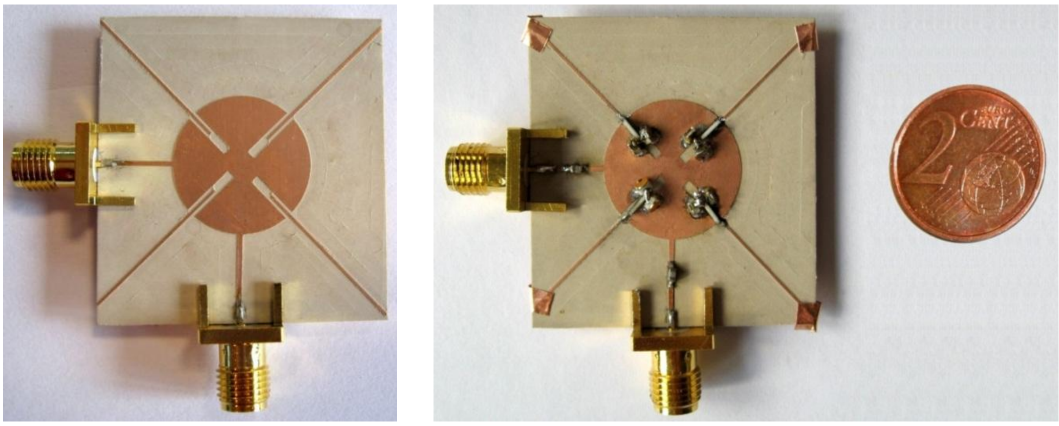

Figure 66 – (a) Fabricated circular patch filter without tuning elements. (b) Assembled tunable bandpass circular patch filter beside of a 2 € cents piece.

The center frequency of the patch filter could be continuously tuned from 1.8 GHz to 2.35 GHz, which represents a tuning range of 27 % with a DC bias voltage ranging from 0.5 V to 20 V. This is equivalent to the total capacitance of the back-to-back configuration varying from 0.2 pF to 0.8 pF. Within this range, the results showed good performance with the insertion loss lower than 2.8 dB and return loss better than 11 dB.

Nonetheless, a more rigorous limit could be set to a maximum IL of 2 dB and RL of 13 dB, reducing the tuning range from 2 GHz to 2.35 GHz (16 % of tuning range). These measured results are shown in Figure 68. It can be seen that the measurements are in very good agreement with the simulated results and the theoretical curves in Figure 64 and Figure 65, respectively. As expected, at the same time, the filter $FBW_{3dB}$ could be changed from 9 % to 26 %

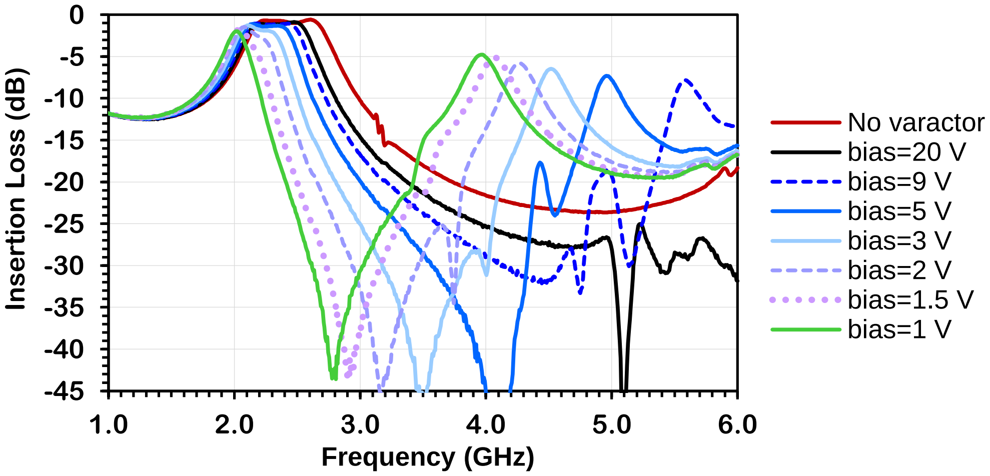

Figure 67 – Measured frequency response (insertion loss) of the tunable circular patch filter with a single DC bias applied to all varactors from 1 V to 20 V.

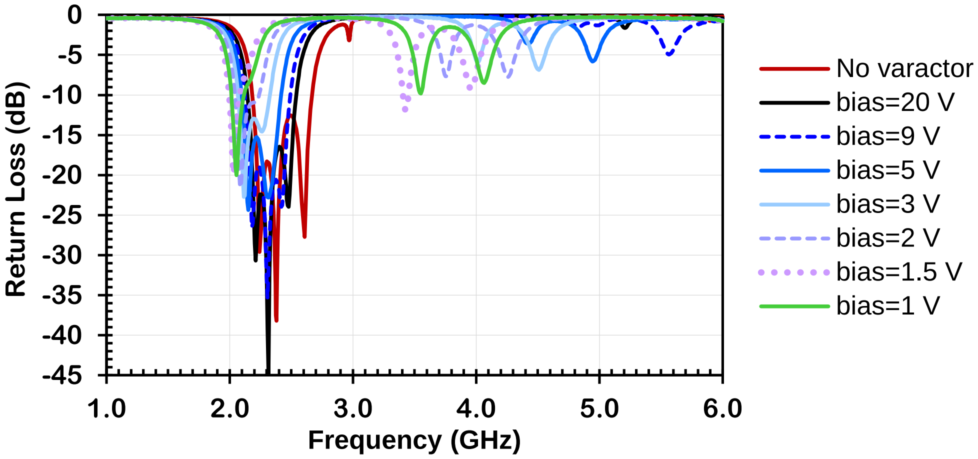

Figure 68 – Measured frequency response (return loss) of the tunable circular patch filter with a single DC bias applied to all varactors from 1 V to 20 V.

## 5.4.2 NONLINEAR MEASUREMENTS

### *5.4.2.1 1-dB Compression Point ($P_{1dB}$)*

The 1-dB compression point ($P_{1dB}$) specified at the input of the filter was measured at the center frequency for different low biasing conditions, presented in Table 4.2. For DC bias voltages higher than 2 V, the maximum input power allowed by the setup (+21.4 dBm) was reached, and the output had not yet been compressed thus, the measurement could not be done. The important fact is that the filter is easily capable of handle +10 dBm of power, even at low bias voltage, suitable to most communication systems. If a tunable working frequency comprised between 2 GHz and 2.35 GHz is considered, then the $P_{1dB}$ is better than +18.8 dBm, the insertion is lower than 2 dB, and the return loss is better than 13 dB, making this kind of tunable filter very efficient.

Table 5.3 - $P_{1dB}$ of the tunable circular filter for different biasing conditions.

| Center Frequency (GHz) | Bias Voltage (V) | $P_{1dB}$ (dBm) |
|---|---|---|
| 1.95 | 1.0 | +12.9 |
| 1.98 | 1.5 | +15.7 |
| 2.0 | 2.0 | +18.8 |
| >2.0 | >2.0 | > +18.8 |

#### *5.4.2.2 Third-order Intercept Point*

Two tones separated by $\Delta f$ = 5 MHz were positioned within the bandwidth of the filter, tuned to very low bias voltage with the measurement setup shown in Figure 11. The tones were delivered to the filter with power level from -20 dBm to -1.6 dBm. The level of input tones and the $3^{rd}$ order intermodulation components were measured at the filter output and were used to calculate the $3^{rd}$ order intercept point (IIP3) of the filter referred to the input port.

The minimum IIP3 was found to be of +25.8 dBm for the 175 MHz-bandwidth filter centered at 1.95 GHz as shown in Table 4.3. As expected, this value improves for higher bias voltages and center frequencies. The IIP3 is greater than +31 dBm when the center frequency is higher than 2 GHz.

Table 5.4 – Measured IIP3 of the tunable filter with varactor diodes in back-to-back configuration.

| Center Frequency (GHz) | Bias Voltage (V) | IP3 (dBm) |
|---|---|---|
| 1.95 | 1.0 | +25.8 |
| 1.98 | 1.5 | +29.5 |
| 2.0 | 2.0 | +31.3 |

## 5.5 EXTENDED ANALYSIS OF THE COUPLING MATRIX

The bias configuration using only one voltage is very simple, although it limits the degree of freedom related to the control of the resonant modes. Independent bias voltages for each varactor diode (except for $C_A$ and $C_C$, which should always act as matched pair, being changed together) leads to a higher degree of freedom because more configurations of center frequency and bandwidths can be chosen. A further analysis of the coupling matrix of this filter leads to some considerations about using this circular patch filter to obtain a tunable filter with constant bandwidth or a tunable filter with constant frequency.

As the bandwidth of this filter is determined by ($M_{33}$ – $M_{11}$), if this difference is kept constant, filters with the same fractional bandwidth at different frequencies can be designed. It is important to remind, that even if $M_{22}$ does not affect directly the width of the passband, it should be also changed in a manner that its frequency remains between the two other frequencies otherwise the passband characteristic will change. Thus, for keeping the bandwidth constant, $M_{11}$ and $M_{33}$ should change in the same direction and by the same amount $z$. $M_{22}$ should also change in the same direction and by an amount, ideally the same as the others, as shown in Figure 69, as a response for the matrix (49), but it is not obligatory. The study of the effects of each capacitance in the filter response presented in section 5.3 showed that $C_B$ changes both $M_{11}$ and $M_{33}$. On the other hand, $C_A$ and $C_C$ change both $M_{22}$ and $M_{33}$. With the combination of these capacitances, $M_{33}$ always changes more than $M_{11}$, and therefore, a constant fractional bandwidth is not possible for this filter, even with the use of multiple bias voltages. Therefore, the filter response presented in Figure 69 cannot be obtained experimentally.

$$M_{FBW\ cte} = \begin{bmatrix} 0 & 0.4890 & 0.4609 & 0.4500 & 0 \\ 0.4890 & 0.8772 + z & 0 & 0 & -0.4890 \\ 0.4609 & 0 & 0.0520 + \mathrm{z} & 0 & 0.4609 \\ 0.4500 & 0 & 0 & -0.8280 + z & -0.4500 \\ 0 & -0.4890 & 0.4609 & -0.4500 & 0 \end{bmatrix} \quad (49)$$

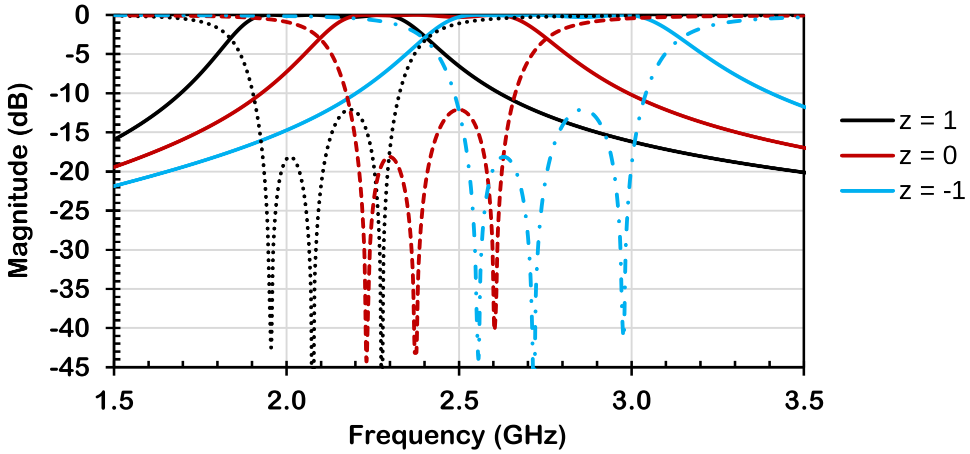

Figure 69 – Theoretical responses for different center frequencies with the same fractional bandwidth.

On the other hand, keeping a constant center frequency and varying the bandwidth can be achieved by changing both $M_{11}$ and $M_{33}$ in the opposite direction, keeping the condition ($M_{11}$ + $M_{33}$ + $M_{22}$)/3 constant. A basic example is given by matrix (50), with the theoretical curves presented in Figure 70. Again, from the study presented in section 5.3, it was shown that $C_B$ changes both $M_{11}$ and $M_{33}$, and $C_A$ and $C_C$ change both $M_{22}$ and $M_{33}$. Therefore, a tunable bandwidth filter with constant center frequency is feasible with the use of two bias voltages, one to control $C_B$ and another one to control $C_A$ and $C_C$ in opposite ways. For that, the $C_B$ bias voltage should increase while decreasing $C_A$ and $C_C$ bias voltage (or vice-versa), without any capacitance at slot D.

$$M_{f_0\ cte} = \begin{bmatrix} 0 & 0.4890 & 0.4609 & 0.4500 & 0 \\ 0.4890 & 0.8772 + k & 0 & 0 & -0.4890 \\ 0.4609 & 0 & 0.0520 & 0 & 0.4609 \\ 0.4500 & 0 & 0 & -0.8280 - k & -0.4500 \\ 0 & -0.4890 & 0.4609 & -0.4500 & 0 \end{bmatrix} \quad (50)$$

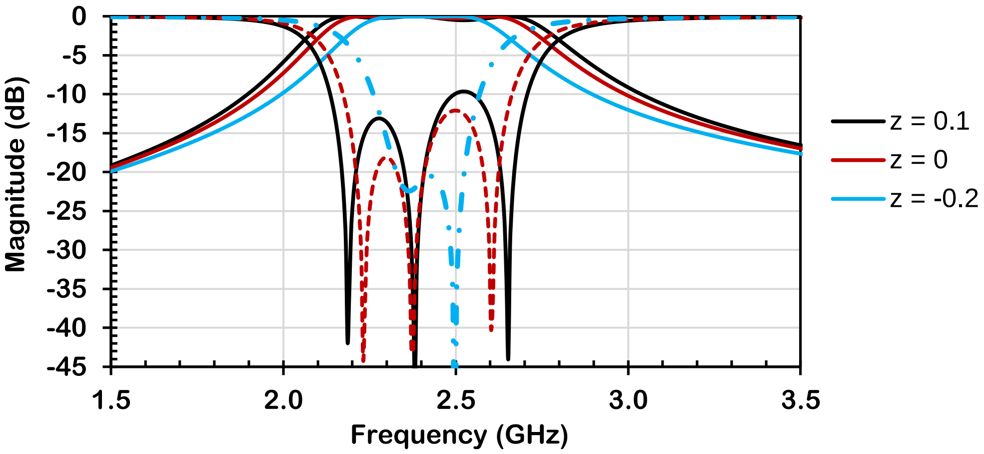

Figure 70 – Theoretical responses for different bandwidths with the same center frequency.

Moreover, in order to improve the selectivity of the filter without tuning elements, it is possible to physically realize a higher coupling between the input and output by changing the layout, and bring the transmission zero closer to the filter passband. For example, if the layout is folded at the symmetry axis, as illustrated in Figure 71, and a small rectangular cut is opened in the ground plane right between the input and output, the necessary coupling for changing the position of the transmission zero can be created.

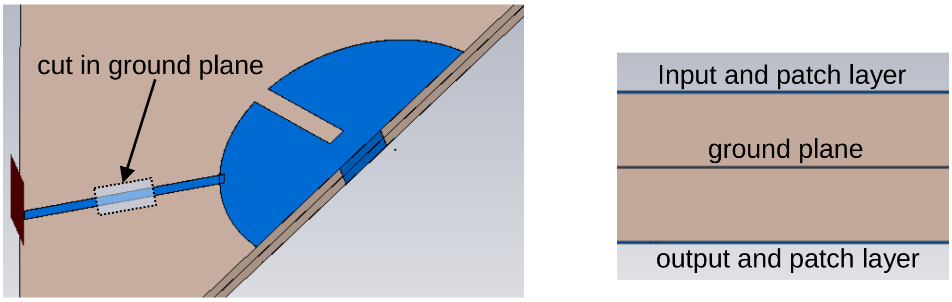

(a)

(b)

Figure 71 – Illustration of a layout of the filter folded at its symmetry axis in order to increase the coupling between the feed lines and achieve a better selectivity for the filter.

Simulations with different dimensions of the cut in the ground plane confirmed the improvement of selectivity, presented in Figure 72. As expected, the frequency at which the transmission zero occurs was reduced when the coupling between feed lines was increased, with a longer cut in the ground plane. This filter can be easily fabricated in a multilayer process without major problems and by using plated through holes for the connections of the two layers of the patch at the symmetry axis. This simulation was carried out in HFSS, which is a very good 3D EM simulator, and very easy to draw the 3D layout into.

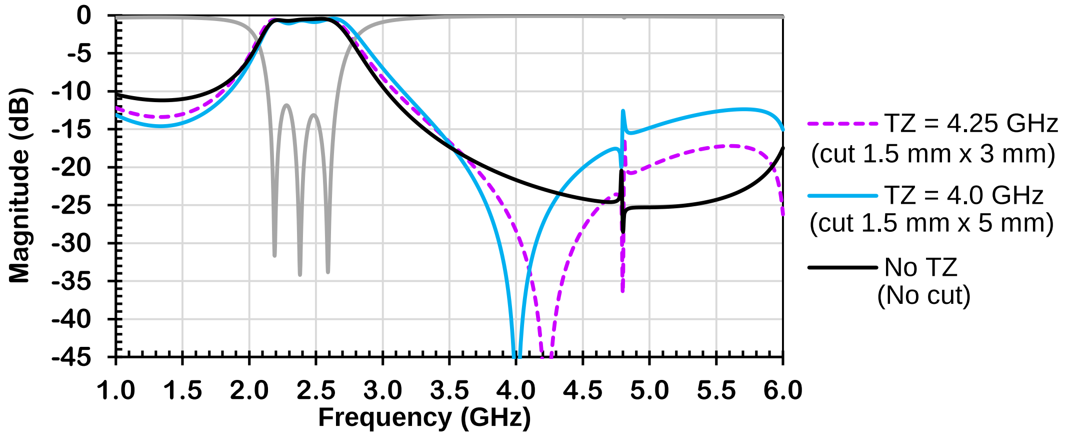

Figure 72 – Simulation of the layout of the filter folded at its symmetry axis in order to increase the coupling between input and output. Frequency response of the filter without the cut (in black) and with different dimensions of the cut made at the ground plane, indicated in Figure 71.

## 5.6 CHAPTER SUMMARY & DISCUSSION

A detailed study of a tunable triple-mode circular patch filter was presented with the proposed methodology using a new theoretical analysis of the filter coupling scheme. The tunable filter is formed by a triple mode circular patch resonator with two pairs of slots, in which two varactors are connected in series. Measurements show that it is possible to continuously tune the center frequency of the patch filter from 1.8 GHz to 2.35 GHz using a DC bias voltage ranging from 0.5 V to 20 V. Within this range, the bandwidth of this filter varies simultaneously from 8.5 % to 26 %. All results show insertion loss lower than 2.8 dB and return loss better than 11 dB. The unloaded patch filter reaches a miniaturization of 48 % (calculated by (41)) compared to a patch resonator at the same frequency (2.41 GHz) without the slots. The center frequency of the tunable patch filter with varactor diodes could be tuned up to 1.8 GHz. Considering this frequency, the area reduction is even higher, of 72 %, comparing to a patch resonator at 1.8 GHz.

The direct analysis of the coupling matrix explained well the filter behavior for different tuning bias conditions. The filter was fabricated using a single DC bias voltage for all the varactor diodes for simplicity purposes, which makes the center frequency and the bandwidth to decrease simultaneously. The bias configuration using only one voltage is very simple, although it limits the degree of freedom related to the control of the resonant modes. However, what is important to point out is that the behavior of the filter is very well modeled by the proposed coupling scheme.

It was shown in the extended theoretical analysis in section 5.5 that an independent bias voltage for each varactor diode (except for $C_A$ and $C_C$, which should always be changed together) leads to a higher degree of freedom because more configurations of center frequency and bandwidths can be chosen, or other type of tuning, as different bandwidths at the same center frequency.

The unloaded quality factor $Q_u$ of this filter was calculated from eq. (39). Here, $N = 3$ thus, the 3rd order Butterworth elements of a low-pass prototype filter were considered: $g_1 = g_3 = 1$ and $g_2 = 2$. At the initial frequency without tuning element ($f_c$ = 2.41 GHz and bandwidth = 27 %), the filter $Q_u$ equals 81. When the filter was tuned to the maximum frequency of the tuning range ($f_c$ = 2.35 GHz and bandwidth = 26 %), $Q_u$ equals 84. When the filter was tuned to the minimum frequency of the tuning range ($f_c$ = 1.8 GHz and bandwidth = 8.5 %), $Q_u$ equals 73.

The tunable circular patch filter designed in this chapter used a single bias voltage. Because of that, its tuning characteristic was a “type C - simultaneously $f_c$ and bandwidth tuning, without independent control”. Although the center frequency and bandwidth of the filter changed together, the figure of merit FoM was calculated considering one at a time. Considering the bandwidth tuning range, the filter achieved a high range of 104 %. Considering the center frequency, the filter achieved a very good tuning range of 27 %.

These values lead to high FoMs, defined in chapter 2, as shown in Table 5.5. This table compares the designed tunable patch filters in this chapter, in chapter 4, and the tunable filters presented in the literature. The filter also presented a good SF of 3.9.

Table 5.5 - Comparison of tunable filters from the international literature and the tunable circular patch filter presented in this chapter.

| Ref | Topology | Tuning type | Tuning Element | DC bias | $f_{min}$ (GHz) | $IL_{max}$ (dB) | Tuning range | Area ($mm^2$) | FoM |
|---|---|---|---|---|---|---|---|---|---|
| [23] | square Ring | D - discrete | varactor diode | 5.5 V | 2.45 | 1.6 | - | 900 | - |
| [24] | open Loop | C - discrete | $VO_2$ switch | - | 9.0 | - | 5.4 % | 84 | - |
| [25] | stub | B - discrete | PIN diode | - | 1.9 | 4.1 | 50 % | 1200 | 2.2 |
| [26] | ring & stub | C - discrete | PIN diode | - | 2.4 | 1.35 | 20 % | 900 | 1.01 |
| [27] | combline | A - continuous | varactor diode | 20 V | 0.75 | 5.0 | 18 % | 1250 | 1.86 |
| [28] | meander loop | C - continuous | varactor diode | 20 V | 1.68 | 7.6 | 41 % | 400 | 1.20 |
| [29] | folded | C - continuous | GaAs varactor diode | 20 V | 1.39 | 2.5 | 26 % | 200 | 15.6 |
| [30] | combline | C - continuous | BST varactor | 100 V | 11.7 | 10.0 | 20 % | 8.8 | 0.54 |
| [31] | folded | D - continuous | varactor diode | 20 V | 1.06 | 3.5 | 5.5 % | 1260 | 0.54 |
| [32] | CPW ring | B - continuous | BST varactor | 35 V | 1.8 | 2.5 | 10 % | 1015 | 0.56 |
| [35] | Triangular | B - discrete | PIN diode | 10 V | 10 | 3.3 | 60 % | 180 | 0.42 |

| Ref | Topology | Tuning type | Tuning Element | DC bias | $f_{min}$ (GHz) | $IL_{max}$ (dB) | Tuning range | Area (mm$^2$) | FoM |
|---|---|---|---|---|---|---|---|---|---|
| [36] | Patch Square Patch | A - discrete | PIN diode | 10 V | 8.9 | 3.7 | 10 % | 225 | 0.06 |
| Filter chapter 4 | Triangular Patch | A - continuous | GaAs varactor diode | 22 V | 3.0 | 3 | 15 % | 375 | 0.71 |
| Filter chapter 4 | Triangular patch | B - continuous | GaAs varactor diode | 7 V | 3.36 | 3 | 67 % | 375 | 2.2 |
| This filter | Circular Patch | C - continuous | GaAs varactor diode | 22 V | 1.8 | 2.8 | 27 % | 289 | 4.0 |
| This filter | Circular patch | C - continuous | GaAs varactor diode | 22 V | 1.8 | 2.8 | 104 % | 289 | 15.7 |

Finally, these good results suggest that the investigation of patch filters using other configurations with MEMS capacitors or switches can be very promising.

# 6 CONCLUSIONS & FUTURE WORK

This chapter presents the main conclusions of this thesis and proposes some future research directions in the area of microwave tunable patch filters that could be developed based on the design and synthesis methodology presented in this thesis.

## 6.1 CONCLUSIONS

The aim of this thesis was the design and the synthesis of tunable bandpass filters at microwave frequencies using planar patch resonators. The initially proposed goals were achieved, with original contributions presented in conferences, magazines, and patent deposits in the field of microwave tunable filters using planar patch resonators. These works are listed in the section “Publications Derived from this Work” after the “References” of this thesis.

The knowledge resulting from the analysis of the resonant modes of patch resonators was applied on the establishment of a design procedure for microwave tunable multimode filters. The methodology provided the techniques to extract the coupling scheme that models the filter behavior and the necessary equations for calculating the corresponding coupling matrix. The synthesis technique using coupling matrix was valuable to the tunability analysis, as well as the complete 3D EM simulations of the filter. The complete simulations were carried out through the combination of the 3D electromagnetic simulation of the filter layout with the electrical simulations of the tuning devices, represented by their lumped elements model. Lossless simulations were compared to simulations considering the substrate dielectric and conductor losses and the equivalent electrical circuit model of the tuning element in order to assess their effects. The final approach was to compare the theoretical filter response resulting from the analysis of the coupling matrix coefficients to the simulation results considering the tuning element model. This allowed the correct model of the tuning effect and the definition of the tuning possibilities and limits, corroborating the theory.

The methodology was applied to the design of two tunable patch filters using varactor diodes electronically controlled by a DC bias voltage. The filters were fabricated using Microwave Integrated Circuit (MIC) technology on flexible substrates. The most critical layouts dimensions were compatible with the fabrication processes, resulting in low-cost easy-fabrication filters. The tunable elements were mounted on the filter with regular soldering, and realized by varactor diodes in a back-to-back configuration. A 0 V to 22 V DC bias voltage was used to control the varactor diodes capacitance.

The first filter designed was a dual-mode bandpass filter that used a triangular patch resonator with two perpendicular slots, allowing the independent control of the center frequency and bandwidth. The filter was designed at 3.8 GHz and could be tuned to different frequencies while keeping a constant bandwidth, achieving a center frequency tuning range of 14.5 %. On the other hand, the same filter could be tuned with different bandwidths while maintaining a constant center frequency, which resulted in a maximum bandwidth tuning range of 67 %. Lastly, considering the variation of the center frequency regardless of the bandwidth and vice-versa, the filter presented 20 % of center frequency tuning range from 2.9 GHz to 3.5 GHz and a $\mathrm{FBW}_{3dB}$ tuning range from 4 % to 12 %.

The second filter designed was a triple-mode bandpass filter and used a circular patch resonator with four slots. The filter was designed at 2.4 GHz, using a single voltage for biasing all the varactor diodes of the filter. The center frequency of the filter was tuned simultaneously with the bandwidth, reaching high tuning ranges of 27 % and 104 %, respectively. Using two bias voltages, the filter could be tuned with different bandwidths at the same center frequency.

Nonlinear measurements showed that both filters are capable of handling high levels of power. The tunable circular patch filter presented a 1-dB compression point ($P_{1dB}$) better than +12.9 dBm and a 3rd-order intercept point (IIP3) better than +25.8 dBm. The tunable triangular patch filter presented a $P_{1dB}$ better than +14.5 dBm and a IIP3 better than +29.9 dBm.

Finally, the developed methodology for design and synthesis of microwave tunable patch filters was validated by the measured electrical performances of both filters, which were in very good agreement with the theoretical and simulation results. This is a very flexible methodology, which can be applied to the analysis and comprehension of microwave filters of any order, with any coupling scheme, or with distinct tuning mechanisms.

## 6.2 FUTURE WORKS

The methodology presented in this thesis could be applied to the design of higher order filters by coupling more than one resonator, in order to achieve smaller bandwidths, higher levels of out-of-band rejection and sharper cut-off slopes.

The theoretical analysis proposed in this thesis and simulated results indicate that not only bandpass patch filters, but also stopband patch filters can be tuned with good performance. In terms of reconfigurable filters, some initial analyses showed that patch filters can be easily switched to change from a bandpass to a stopband filter configuration.

Although the tuning of the designed patch filters was realized by varactor diodes, other types of tuning elements could be considered. Tuning elements such as MEMS or ferroelectric capacitors have been proven to be of great interest for tuning filters because of characteristics such as low loss, excellent linearity and low bias voltages. In this sense, initial studies on the design of MEMS varactors integrated in tunable patch filters have already began with promising results, showing higher tuning ranges, more flexible capacitance ranges and lower actuation voltage (less than 10 V) when compared to the available commercial varactor diodes.

# REFERENCES

[1] W. Sichak and H. Augenblick, “Tunable Waveguide Filters,” *Proceedings of the IRE,* vol. 39, no. 9, pp. 1055-1059, Sep. 1951.

[2] M.H.N. Potok, “Capacitive-iris-type mechanically tunable waveguide filters for the X-band,” *Proceedings of the IEE Part B: Electronic and Communication Engineering,* vol. 109, no. 48, p. 505, Nov. 1962.

[3] C. Nelson, “Ferrite-Tunable Microwave Cavities and the Introduction of a New Reflectionless, Tunable Microwave Filter,” *Proceedings of the IRE*, vol. 44, no. 10, pp. 1449-1455, Oct. 1956.

[4] P.S. Carter, “Magnetically-Tunable Microwave Filters Using Single-Crystal Yttrium-Iron-Garnet Resonators,” *IEEE Transactions on Microwave Theory and Techniques,* vol. 9, no. 3, pp. 252-260, May. 1961.

[5] M.H. Norwood and E. Shatz, “Voltage variable capacitor tuning: A review,” *Proceedings of the IEEE*, vol. 56, no. 5, pp. 788-798, May. 1968.

[6] L. Kaufman and W.H. Steier, “A Plasma-Column Band-Pass Microwave Filter,” *IEEE Transactions on Microwave Theory and Techniques,* vol. 10, no. 6, pp. 431-439, Nov. 1962.

[7] C.K. Greene, “A Microstrip Nonreciprocal Tunable YIG Filter,” *IEEE Journal of Solid-State Circuits,* vol. 3, no. 2, pp. 146-148, Jun. 1968.

[8] K. Chang et al., “On the Study of Microstrip Ring and Varactor-Tuned Ring Circuits,” *IEEE Transactions on Microwave Theory and Techniques,* vol. 35, no. 12, pp. 1288-1295, Dec. 1987.

[9] M. Igarashi and Y. Naito, “Properties of a Four-Port Nonreciprocal Circuit Utilizing YIG on Stripline--Filter and Circulator,” *IEEE Transactions on Microwave Theory and Techniques*, vol. 20, no. 12, pp. 828-833, Dec. 1972.

[10] I.C. Hunter and J.D. Rhodes, “Electronically Tunable Microwave Bandpass Filters,” *IEEE Transactions on Microwave Theory and Techniques,* vol. 30, no. 9, pp. 1354-1360, Sep. 1982.

[11] Y.-H. Shu et al., “Electronically switchable and tunable coplanar waveguide-slotline band-pass filters,” *IEEE Transactions on Microwave Theory and Techniques*, vol. 39, no. 3, pp. 548-554, Mar. 1991.

[12] S. Kumar, “Electronically tunable ring resonator microstrip and suspended-substrate filters,” *Electronics Letters*, vol. 27, no. 6, p. 521, Mar. 1991.

[13] W.-guan Lin, “Microwave Filters Employing a Single Cavity Excited in More than One Mode,” *Journal of Applied Physics*, vol. 22, no. 8, p. 989, Aug. 1951.

[14] I. Wolff, “Microstrip bandpass filter using degenerate modes of a microstrip ring resonator,” *Electronics Letters*, vol. 8, no. 12, p. 302, Jun. 1972.

[15] R.D. Wanselow, “Prototype Characteristics for a Class of Dual-Mode Filters (Short Papers),” *IEEE Transactions on Microwave Theory and Techniques*, vol. 23, no. 8, pp. 708-711, Aug. 1975.

[16] S. Kallianteris et al., “A New Class of Dual-Mode Microwave Filters for Space Application,” *7th European Microwave Conference, 1977*, pp. 51-58, Oct. 1977.

[17] P. Guillon et al., “Dielectric resonator dual modes filter,” *Electronics Letters*, vol. 16, no. 17, p. 646, Aug. 1980.

[18] M. Guglielmi and G. Gatti, “Experimental Investigation of Dual-Mode Microstrip Ring Resonators,” *20th European Microwave Conference, 1990*, pp. 901-906, Oct. 1990.

[19] J.A. Curtis and S. Fiedziuszko, “Miniature dual mode microstrip filters,” *1991 IEEE MTT-S International Microwave Symposium Digest*, pp. 443-446, 1991.

[20] C.T.-C. Nguyen, “Microelectromechanical devices for wireless communications,” *Proceedings MEMS 98. IEEE. Eleventh Annual International Workshop on Micro Electro Mechanical Systems. An Investigation of Micro Structures, Sensors, Actuators, Machines and Systems (Cat. No.98CH36176)*, pp. 1-7, 1998.

[21] A. Abbaspour-Tamijani et al., “Miniature and tunable filters using mems capacitors,” *IEEE Transactions on Microwave Theory and Techniques*, vol. 51, no. 7, pp. 1878-1885, Jul. 2003.

[22] E. Pistono et al., “Novel factor of merit for center-frequency tunable bandpass filters comparison,” *Microwave and Optical Technology Letters*, vol. 51, no. 4, pp. 985-988, Apr. 2009.

[23] Y.-M. Chen et al., “A reconfigurable bandpass-bandstop filter based on varactor-loaded closed-ring resonators [Technical Committee],” *IEEE Microwave Magazine*, vol. 10, no. 1, pp. 138-140, Feb. 2009.

[24] D. Bouyge et al., “Applications of vanadium dioxide (VO2)-loaded electrically small resonators in the design of tunable filters,” *Proceedings of the 40th European Microwave Conference*, vol. 22, no. 3, pp. 822-825, Sep. 2010.

[25] A. Miller and J.-sheng Hong, “Wideband Bandpass Filter With Reconfigurable Bandwidth,” *IEEE Microwave and Wireless Components Letters*, vol. 20, no. 1, pp. 28-30, Jan. 2010.

[26] C.H. Kim and K. Chang, “Ring Resonator Bandpass Filter With Switchable Bandwidth Using Stepped-Impedance Stubs,” *IEEE Transactions on Microwave Theory and Techniques*, vol. 58, no. 12, pp. 3936-3944, Dec. 2010.

[27] M. Sanchez-Renedo, “High-Selectivity Tunable Planar Combline Filter With Source/Load-Multiresonator Coupling,” *IEEE Microwave and Wireless Components Letters*, vol. 17, no. 7, pp. 513-515, Jul. 2007.

[28] M.R. Al Mutairi et al., “A Novel Reconfigurable Dual-Mode Microstrip Meander Loop Filter,” *2008 38th European Microwave Conference*, no. October, pp. 51-54, Oct. 2008.

[29] M.A. El-Tanani and G.M. Rebeiz, “A Two-Pole Two-Zero Tunable Filter With Improved Linearity,” *IEEE Transactions on Microwave Theory and Techniques*, vol. 57, no. 4, pp. 830-839, Apr. 2009.

[30] J. Sigman et al., “Voltage-Controlled Ku-Band and X-Band Tunable Combline Filters Using Barium-Strontium-Titanate,” *IEEE Microwave and Wireless Components Letters*, vol. 18, no. 9, pp. 593-595, Sep. 2008.

[31] C.-K. Liao et al., “A Reconfigurable Filter Based on Doublet Configuration,” *2007 IEEE/MTT-S International Microwave Symposium*, pp. 1607-1610, Jun. 2007.

[32] Y.-H. Chun et al., “BST-Varactor Tunable Dual-Mode Filter Using Variable Zc Transmission Line,” *IEEE Microwave and Wireless Components Letters*, vol. 18, no. 3, pp. 167-169, Mar. 2008.

[33] J.-S. Hong and S. Li, “Dual-mode microstrip triangular patch resonators and filters,” *IEEE MTT-S International Microwave Symposium Digest, 2003*, no. 1, pp. 1901-1904, 2003.

[34] A.L.C. Serrano, “Projeto de filtros de micro-ondas passa-faixa planares utilizando ressoadores patch dual-mode” M.S. thesis, Dissertação (Mestrado) - Escola Politécnica, Universidade de São Paulo, São Paulo, 2007, [Online]. Available: http://www.teses.usp.br/teses/disponiveis/3/3140/tde-28032008-172509/en.php.

[35] C. Lugo and J. Papapolymerou, “Single switch reconfigurable bandpass filter with variable bandwidth using a dual-mode triangular patch resonator,” *IEEE MTT-S International Microwave Symposium Digest, 2005.*, vol. 00, no. C, pp. 779-782, 2005.

[36] C. Lugo and J. Papapolymerou, “Dual-mode reconfigurable filter with asymmetrical transmission zeros and center frequency control,” *IEEE Microw. Wireless Compon. Lett*, vol. 16, no. 9, pp. 499-501, Sep. 2006.

[37] A.L.C. Serrano and F.S. Correra, “A miniaturized bandpass filter with two transmission zeros using a novel square patch resonator,” *2007 SBMO/IEEE MTT-S International Microwave and Optoelectronics Conference*, pp. 941-945, 2007.

[38] I. Wolff and N. Knoppik, “Rectangular and circular microstrip disk capacitors and resonators,” *IEEE Transactions on Microwave Theory*, vol. 22, no. 10, pp. 857-864, Oct. 1974.

[39] Z. Du et al., “Analysis of microstrip fractal patch antenna for multi-band communication,” *Electronics Letters*, vol. 37, no. 13, p. 805, Jun. 2001.

[40] J. Watkins, “Circular resonant structures in microstrip,” *Electronics Letters*, vol. 5, no. 21, pp. 524-525, Oct. 1969.

[41] C.H.O. Chew, “Effects of Fringing Fields on the Capacitance of Circular Microstrip Disk,” *IEEE Transactions on Microwave Theory and Techniques*, vol. 28, no. 2, pp. 98-104, Feb. 1980.

[42] J. Helszajn and D.S. James, “Planar Triangular Resonators with Magnetic Walls,” *IEEE Transactions on Microwave Theory and Techniques*, vol. 26, no. 2, pp. 95-100, Feb. 1978.

[43] J. Helszajn et al., “Circulators Using Planar Triangular Resonators,” *IEEE Transactions on Microwave Theory and Techniques*, vol. 27, no. 2, pp. 188-193, Feb. 1979.

[44] M. Saito, “Synthesis for general-coupled resonator transmission networks,” *Electronic Communications in Japan*, vol. 53-A, no. 5, p. 2633, 1969.

[45] J. Rhodes, “The Theory of Generalized Interdigital Networks,” *IEEE Transactions on Circuit Theory*, vol. 16, no. 3, pp. 280-288, Mar. 1969.

[46] A.E. Atia and A.E. Williams, “Narrow-Bandpass Waveguide Filters,” *IEEE Transactions on Microwave Theory and Techniques*, vol. 20, no. 4, pp. 258-265, Apr. 1972.

[47] R. Cameron, “General coupling matrix synthesis methods for Chebyshev filtering functions,” *IEEE Transactions on microwave theory and*, vol. 47, no. 4, pp. 433-442, Apr. 1999.

[48] S. Amari, “On the maximum number of finite transmission zeros of coupled resonator filters with a given topology,” *IEEE Microwave and Guided Wave Letters*, vol. 9, no. 9, pp. 354-356, Sep. 1999.

[49] J. Montejo-Garai, “Synthesis of N-even order symmetric filters with N transmission zeros by means of source-load cross coupling,” *Electronics Letters*, vol. 36, no. 3, p. 232, Mar. 2000.

[50] S. Amari, “Direct synthesis of folded symmetric resonator filters with source-load coupling,” *IEEE Microwave and Wireless Components Letters*, vol. 11, no. 6, pp. 264-266, Jun. 2001.

[51] S. Amari et al., “Adaptive synthesis and design of resonator filters with source/load-multiresonator coupling,” *IEEE Transactions on Microwave Theory and Techniques*, vol. 50, no. 8, pp. 1969-1978, Aug. 2002.

[52] J.-S. Hong and M.J. Lancaster, *Microstrip Filters for RF/Microwave Applications*, New York, USA, John Wiley & Sons, Inc., 2001.

[53] R.S. Kwok and J.-F. Liang, “Characterization of High- Resonators for Microwave-Filter Applications,” *IEEE Transactions on Microwave Theory and Techniques*, vol. 47, no. 1, pp. 111-114, 1999.

[54] “CoupleFil,” *http://www.couplefil.com/couplefil.html*, 2010.

[55] J.-S. Hong and S. Li, “Theory and Experiment of Dual-Mode Microstrip Triangular Patch Resonators and Filters,” *IEEE Transactions on Microwave Theory and Techniques*, vol. 52, no. 4, pp. 1237-1243, Apr. 2004.

[56] W. Hu et al., “Dual-Mode Bandpass Filters Using Microstrip Slotted Equilateral Triangular Patch Resonators,” no. 4, pp. 503-508, 2006.

[57] A.L.C. Serrano and F.S. Correra, “Dual-mode bandpass filter using triangular patch resonator with inverted T-shaped slot,” *Microwave and Optical Technology Letters*, vol. 49, no. 12, pp. 2897-2902, Dec. 2007.

[58] K. Buisman et al., “Distortion-Free Varactor Diode Topologies for RF Adaptivity,” *IEEE MTT-S International Microwave Symposium Digest, 2005.*, vol. 0, no. 4, p. 157, 2005.

[59] S. Cohn, “Dissipation Loss in Multiple-Coupled-Resonator Filters,” *Proceedings of the IRE*, vol. 47, no. 8, pp. 1342-1348, Aug. 1959.

[60] G.L. Matthaei et al., *Microwave filters, impedance-matching networks, and coupling structures*, Artech House Norwood, MA, 1980.

[61] L. Dussopt and G.M. Rebeiz, “Intermodulation distortion and power handling in RF MEMS switches, varactors, and tunable filters,” *IEEE Transactions on Microwave Theory and Techniques*, vol. 51, no. 4, pp. 1247-1256, Apr. 2003.

# PUBLICATIONS DERIVED FROM THIS WORK

## ARTICLES/POSTERS

The developed work during this doctorate generated presentations in international workshops, conferences, symposia. It also generated publications of articles in magazines and patent deposit. The following papers were presented and/or published:

A.L.C. Serrano and F.S. Correra, “A triple-mode bandpass filter using a modified circular patch resonator,” *Microwave and Optical Technology Letters*, vol. 51, no. 1, pp. 178-182, Jan. 2009.

A.L.C. Serrano et al., “Tunable Microwave Bandpass Patch Filter,” *GDR-Ondes Paris - CNAM, 2-4 November,* 2009, Paris, France.

A.L.C. Serrano et al., “A Tunable Bandpass Patch Filter,” *IEEE Proc. International Workshop on Microwave Filters*, vol. 1, pp. 72-76, 2009, Toulouse, France.

A.L.C. Serrano et al., “A tunable bandpass patch filter with varactors,” *2010 IEEE MTT-S International Microwave Symposium*, vol. 2, pp. 1752-1755, May. 2010, Anaheim, US.

A.L.C. Serrano et al., “Analysis of a Reconfigurable Bandpass Circular Patch Filter,” *IEEE Transactions on Microwave Theory and Techniques*, vol. 58, no. 12, pp. 1-7, Dec. 2010.

A.L.C. Serrano et al., “Filtre patch triangulaire avec contrôle indépendant de la fréquence centrale et de la bande passante,” *17èmes Journées Nationales Microondes, 18-19-20 Mai*, 2011, Brest, France.

This article is under review:

A.L.C. Serrano et al., “Tunable Triangular *Patch* Filter with Independent Central Frequency and Bandwidth Control,” *IEEE Transactions on Microwave Theory and Techniques*.

## PATENTS

Two patents were deposited, one in France and the other in Brazil:

**Title: “Filtre à résonateur patch accordable”**

Deposit N°: 10/54507

Date: 8 June 2010

**Title: “Filtro de micro-ondas passa-faixa com ressoador bidimensional circular reconfigurável”**

Deposit N°: 018100043240

Date: 17 November 2010

# APPENDIX

```
%---------------------------------------------------------------------------------------------%
% Theoretical curves of S11 e S21 calculated from a coupling matrix %
%---------------------------------------------------------------------------------------------%

clear

%-----------------------------------------------------------%
% To be completed with the filter specifications:

n=;      % n is the order of the filter
fc=;     % Central frequency fc in Hz
BW=;   % Absolute Bandwidth in Hz
%------------------------------------------------------------%

%-----------------------------------------------------------------------------------------------%
%Matrices

R=zeros(n+2);
R(1,1)=1;
R(n+2,n+2)=1;

W=eye(n+2);
W(1,1)=0;
W(n+2,n+2)=0;

M=zeros(n+2);

% To be complete with the necessary couplings of the coupling scheme
% where 1 is related to the source;
% 2 to N-1 are related to the modes;
% N+2 is related to the load.
M(1,2)=;
M(1,3)=;
M(2,2)=;
M(2,3)=;
M(3,3)=;

% For a symmetrical matrix M:
for b=1:n+2
   for a=1:n+2
      M(a,b)=M(b,a);
   end
end

disp(M)
%-----------------------------------------------------------------------------------------------%

%---------------------------------------------------------%
% To be completed with the graphic definition:

points=;          % Definition of the curves
fi=;                 % Initial frequency of the graphic
ffinal=;            % Final frequency of the graphic
f=fi:(ffinal-fi)/(points-1):ffinal;
%---------------------------------------------------------%
```

```
%----------------------------------------------------------%
% S-parameters calculus
for a=1:points

    f1=fc*(f(a)/fc-fc/f(a))/BW;
    A=M-1j*R+f1*W;
    B=inv(A);

    S21(a)=20*log10(abs(-2*1j*B(n+2,1)));
    S11(a)=20*log10(abs(1+2*1j*B(1,1)));

end

%----------------------------------------------------------%

plot(f,S21,'b',f,S11,'k','LineWidth',2)
```